Dissertation zur Erlangung des Doktorgrades

der Fakultät für Chemie und Pharmazie

der Ludwig-Maximilans-Universität München

High Throughput assisted Investigation on

Lanthanide (III)

Tetrakisphosphonates

von

Monika Plabst

aus

München

2009

Erklärung

Diese Promotion wurde im Sinne von § 13 Abs. 3 der Promotionsordnung vom
29. Januar 1998 von Herrn Professor Dr. Thomas Bein betreut.

Ehrenwörtliche Versicherung

Diese Dissertation wurde selbstständig, ohne unerlaubte Hilfsmittel erarbeitet.

München, am 19. 10. 2009

_____

(Unterschrift der Autorin)

Dissertation eingereicht am 12. 10. 2009

1. Gutachter: Prof. Dr. Thomas Bein

2. Gutachter: Prof. Dr. Peter Klüfers

Mündliche Prüfung am 26. 11. 2009

Danksagung

Diese Arbeit ist im Arbeitskreis von Herrn Professor Thomas Bein am Institut für physikalische Chemie der Ludwig- Maximilians-Universität München entstanden und wäre ohne die Unterstützung vieler Menschen nicht möglich gewesen. Vor allen Dingen möchte ich meinem Doktorvater Herrn Professor Thomas Bein ganz herzlich für die Aufnahme in seinen Arbeitskreis danken, indem ich unter besten Bedingungen arbeiten konnte. Ohne die geistige Freiheit, die er mir zugestanden hat, sein Vertrauen in meine Arbeit und die Unterstützung bei den Publikationen wäre das nicht möglich gewesen.

Bei Herrn Professor Peter Klüfers vom Institut für anorganische Chemie möchte ich mich herzlich für die Übernahme des Zweitgutachtens bedanken. Der Prüfungskommission gilt mein großer Dank für die Zeit, die Sie sich fürs Lesen der vorliegenden Arbeit genommen haben.

Besonderer Dank geht an Frau Dr. Lynne Mc Cusker von der ETH Zürich für die Rietfeldverfeinerung einer meiner Strukturen. Danke für das Interesse an meiner Arbeit, die guten Diskussionen und die ausgesprochen wertvollen und hilfreichen Ratschläge.

Bei Herrn Dr. Peter Maier vom Institut für anorganische Chemie möchte ich mich für die Datensammlungen für die Röntgenstrukturanalysen bedanken. Bei Herrn Peter Maier und Herrn Helmut Hartl vom Institut für anorganische Chemie bedanke ich mich für die Aufnahme zahlreicher NMR Spektren und ICP-OES Analysen.

Bei Jürgen Sauer von der Firma Nanoscape möchte ich mich dafür bedanken, dass er mir die ersten Seltenerden geschenkt hat. Sie waren inspirierend!

Ganz besonders möchte ich mich bei meinen Kollegen bedanken, die mir die Jahre im Arbeitskreis unvergesslich gemacht haben. Danke an Camilla für viele

gute Diskussionen und gemeinsame Kaffeepausen, an Johann für seine ganz besondere Weltanschauung und all die Dymo Labels, an Keili z.B. für die Teeblumen, an Valentina, Huihong, Anderl und Andreas für die angenehme Zeit im Büro, an Mirjam für unsere gemeinsame Erkenntnis was das Wort FAN wirklich bedeutet, an Johann II für die Unterstützung am D8, an Gabriela und Olivier für die Einführung in die Welt der Zeolite und gemeinsame Wanderungen, an Johannes, Hendrik, Lea, Barbara, Alex und Enrica dafür, dass sie den alten Kern gebildet haben, an Ralf z. B. fürs Organisieren vieler Stammtische, an Markus und Steffen (danke für die REMs), Jörg, Axel, Benni, Norma, Dina, Karin, Bastian, Christian, Doro, Flo, Hans, an Yan, Yujing, ShaoFeng, Hongji und Kun Hou (dafür, dass ich jetzt weiß, was Restaurant auf Chinesisch bedeutet), Vesna, Mihaela und alle die ich jetzt vergessen haben, da der Arbeitskreis so schnell wächst, dass ich den Überblick verliere…

Bei unserer Sekretärinnen Regina und Dagmar möchte ich mich dafür bedanken, dass Sie diesen Überblick immer behalten haben und für die stete Unterstützung in allen organisatorischen Belangen.

Ein Besonderer Dank geht auch an Tina für Ihr stetes Bemühen um alles, was anfällt und ganz besonders für Ihre Unterstützung beim Aufbau und Testen des Syntheseroboters. Deine Tortenrezepte sind übrigens nach wie vor ungeschlagen!

Der größte Dank gilt meiner Familie und meinen Freunden die mich die ganze Zeit ermutigt und unterstützt haben. Al final muchas gracias a ti, Xavier, por pasar estos años conmigo. Con el deseo de empezar una nueva etapa!

Abstract

Phosphonic acids and lanthanides are both promising building blocks for the synthesis of new metal organic frameworks (MOFs). However, their chemical and structural flexibility challenges the tailoring of well defined crystalline structures. This work is focused on overcoming this lack of control with the introduction of 1,4-phenylenbis(methylidyne)-tetrakis(phosphonic acid), H_8L, a molecule that combines a rigid spacer and two ligands suitable for the chelation of large ions.

Using a synthetic high-throughput approach, H_8L was investigated as new molecular building block for the formation of coordination frameworks with lanthanides (Ln = La, Nd, Gd, Dy) under hydrothermal conditions. Thereby, 14 new lanthanide phosphonates were discovered, categorized into three structure types and their crystallization fields described. Structure type I comprises six compounds with the general formula **Ln(H_5L)**. The examples of $Ln[(PO_3H)_2CH$-C_6H_4-$CH(PO_3H)(PO_3H_2)]\cdot4H_2O$, where Ln = La, Nd, reveal two-dimensional coordination networks having a layered structure, but differ in the layer stacking. Structure type II comprises 4 compounds of the general formula **Ln_2(H_2L)** and is represented by $La_2[(HO_3P)(O_3P)$-CH-C_6H_4-CH-$(PO_3)(PO_3H)]$ $\cdot8H_2O$, a layered structure with dimeric lanthanum coordination polyhedra. Four compounds of the type **NaLn(H_4L)** are in stucture type III, which was solved from $NaLa[(PO_3H)_2CH$-C_6H_4-$CH(PO_3H)_2]\cdot4H_2O$. This structure consists of a three-dimensional open framework with La^{3+} coordinated by bisphosphonate units in an exclusively bidentate fashion. It provides one-dimensional rhombic channels which are occupied by sodium ions and water molecules acting as guests.

Abstract

The anionic, open-framework of the new MOF **NaLa(H$_4$L)** exhibits an exceptional selectivity for monovalent metal cations. The presented work elucidates the relationship between the ion-exchange behavior and the framework flexibility: The exchange of the Na$^+$ ions in **NaLa(H$_4$L)** with alkaline-earth, alkaline and selected transition metal ions was studied. EDX and ICP-OES elemental analysis revealed that ion exchange was successful with monovalent ions, while higher-valent ions were rejected. An explanation for this charge selectivity could be found in the site-specific role of the guest cation. X-ray diffraction and thermogravimetric studies on the reversible hydration and dehydration behavior demonstrate that **NaLa(H$_4$L)** has a flexible framework. Contraction of the channels upon dehydration leads to a decrease in the cell volume by 15%. Rietveld refinement of the structure of the dehydrated form **NaLa(H$_4$L)$_{dehyd}$** revealed the key role played by the guest cation in the channel-shrinking mechanism. In the hydrated, expanded form, each Na$^+$ ion guest shares three phosphonate oxygens with a La^{3+} ion in a lanthanum phosphonate chain that defines part of the wall of a rhombic channel. The Na$^+$ ion completes its octahedral coordination sphere with two water molecules and a weaker bond to a fourth phosphonate oxygen. In the dehydrated, contracted form, the Na$^+$ ion loses the two water molecules and moves towards a second La^{3+} ion, which is located in an adjacent lanthanum phosphonate chain, to share two more phosphonate oxygens, and becomes 5-coordinate. This results in the formation of an -La-O-Na-O-La- chain and a concomitant shrinking of the channels. A comparison of the monovalent metal (M(I)) ion-exchanged compounds, **M(I)La(H$_4$L)**, reveals that both the ionic radius and the enthalpy of hydration of the guest cation affect the equilibrium between the expanded and the contracted forms, and that the framework adapts specifically to the size of the guest cation.

Furthermore the influence of the guest ion on the synthesis of **NaLa(H$_4$L)** was investigated. In a screening of the synthesis parameters, Na$^+$ was identified as a strong structure-directing agent for this framework. In addition, a series of compounds **MLa(H$_4$L)** with M = Li$^+$, Na$^+$, K$^+$, NH$_4$$^+$ and Rb$^+$ were prepared by synthesis or ion exchange and characterized using X-ray powder diffraction, elemental analysis and scanning electron microscopy. Sorption of N$_2$, Kr and H$_2$O in these compounds revealed a preference of the network for water molecules. Furthermore a strong influence of the guest ions on the shape of the water sorption isotherms could be observed. The isotherms of **LiLa(H$_4$L)**, **NaLa(H$_4$L)** and **KLa(H$_4$L)** show one distinctive step of adsorption that can be correlated with the expansion of the flexible framework upon hydration. The required partial pressure for the pore expansion depends on the incorporated guest ion and increases with the decreasing hydration enthalpy form Li$^+$ to K$^+$.

Table of Contents

1 Introduction

1.1 Metalphosphonates Amongst Other Crystalline Porous Materials

The thermodynamically favored state of atoms or molecules in a solid most often is the close packing in the form of dense matter. If porosity is desired, synthesis strategies must be applied that prevent molecules and atoms from reaching the thermodynamic minimum. One common approach to reach this goal focuses on the trapping of kinetically formed metastable phases, which result from the condensation of small building blocks forming a host structure around an assembly of guest molecules. The second important approach relies on the self-assembling of covalently bonded rigid organic building blocks by metal centres, whose coordination geometries restrict the possibilities for assembly of the building blocks and, thus, prevent them from dense packing. The following chapter will introduce zeolites and metal organic frameworks as representative examples for both approaches and finally discuss metalphosphonates, the target compounds of this work, and their positioning in between the aforementioned classes of materials.

1.1.1 Zeolites and Zeotypes

Definition

Zeolites are crystalline aluminosilicates with open framework type structures and defined pores and cavities in the range of 3-15 Å.[1] They are composed of $[SiO_4]$ tetrahedrons as building blocks which can be partially replaced by $[AlO_4]^-$ tetrahedrons. The resulting negative framework charge is compensated by counter ions located in the pores. According to Loewenstein's Rule the Si/Al

ratio may go as low as unity in which case each [SiO$_4$] tetrahedron is connected to one [AlO$_4$]$^-$ tetrahedron. Lower values would cause unfavourable electrostatic interactions between neighbouring aluminium tetrahedrons bearing a negative charge. Low Si/Al ratios create highly hydrophilic networks with strong affinities to ionic guests. Rising Si/Al ratios lead to a decrease of the framework charge and thus less charge balancing ions. Pure silica zeolites, which are obtained at a Si/Al ratio of infinity, show hydrophobic properties and prefer the absorption of non-polar molecules.

History of Zeolites

The history of zeolites began in 1756 with the discovery of the natural mineral stilbite by the Swedish mineralogist Axel Frederic von Cronstedt.[2] Upon rapidly heating, the crystals released large amount of steam from water that had been absorbed by the material. Based on this, Cronstedt termed the material *zeolite*, from the greek words ζέω (*zeō*), meaning "boil" and λίθος (*lithos*), meaning "stone". Following the discovery of a number of new minerals, zeolites were soon classified as a new new type of hydrated aluminophosphates with several key properties, e.g. reversible dehydration without morphology change (Damour in 1840),[3] reversible ion exchange (Eichhorn in 1858)[4] and molecular sieve effects (Weigl and Steinhoff in 1925).[5] Taylor and Pauling achieved the first determination of a zeolite structure in 1930,[6] which was followed by the preparation of the first synthetic zeolite analogues through the pioneering work of Barrer.[7] Between 1949 and 1954 the synthesis of several zeolite analogues was described by Milton and Breck, e.g zeolites A, X and Y, which are today of commercial importance.[8] Synthetic zeolites of the first decade were prepared from solely inorganic precursors and exhibited low Si/Al ratios. In the 1960s a growing understanding of the synthesis process led to the introduction of quaternary ammonium ions into zeolite synthesis.[9] Due to the decreased charge

density and increased steric requirements in comparison to alkali cations, the zeolites incorporating such organic cations in general display much higher Si/Al ratios and hydrophobicity.[10,11] The key step in this development followed rapidly in 1967 with the disclosure of the first high-silica zeolite, zeolite β (5 < Si/Al < 100), made using the tetraethylammonium cation.[12] In 1978 the first all silica zeolite was obtained with Silicalite-1.[13] Up to the present day the zeolite science flourishes. As of Mai 2009, 192 unique zeolite frameworks have been identified, and over 40 naturally occurring zeolite frameworks are known.[14]

Zeotypes

In a narrower sense the term zeolite is restricted to aluminosilicates. However, the scientific community soon discovered that open frameworks with partial or fully substitution of the SiO_4 / $[AlO_4]^-$ units by heteroelements can be accessed, and extended this family of materials to the so-called zeotypes. A significant number of metal silicates has been discovered, e.g. borosilicates,[15,16] gallosilicates,[17,18] titanosilicates[19] and ferrisilicates.[18] A prominent example for open frameworks without silicon are microporous crystalline aluminophosphates, so called AlPOs, that were first desribed in 1982 by Wilson working at Union Carbide.[20] Constructed from $[PO_4]^+$ and $[AlO_4]^-$ building units, AlPO materials provide neutral frameworks thus complementing the scope of anionic zeolites. However, charge can be induced into AlPO frameworks either by an Al/P-ratio > 1 or by a partial substitution of aluminum or phosphorus by silicon[21] or other elements.[8] Moreover, several metal phosphate open frameworks are reported including phosphates of gallium,[22] indium,[23] tin,[24] antimony,[25] molybdenum,[26] vanadium,[27] iron,[28] cobalt,[28] manganese,[29] copper,[30] nickel,[31] zirconium[32] and titanium.[33] Compared with classical aluminosilicates, bond lengths, bond angles and coordination numbers can vary in zeotypes due

to the type and the amount of the incorporated hetero-atoms. This flexibility allows the formation of new framework structures that have no zeolite analogues. Famous examples are the aluminophosphate VPI-5[34] exhibiting large 18-membered rings or a gallophosphate with a 20 membered ring and a pore opening with the shape of a four leafed clover.[35]

Zeolite Synthesis

The basic chemical reaction in all processes during zeolite formation is the reversible T-O-T bond making and bond breaking reaction in solution, which is catalyzed by a mineralizer (Scheme 1.2.1 - 1) such as hydroxide or fluoride.

$$T\!-\!OH + {}^{\ominus}O\!-\!T \rightleftharpoons T\!-\!O\!-\!T + {}^{\ominus}OH$$

$$T\!-\!OH + HO\!-\!T \rightleftharpoons T\!-\!O\!-\!T + H_2O$$

$$\text{T-atom} = \text{Si, Al}$$
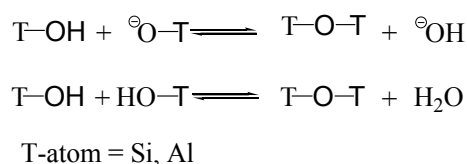
Scheme 1.1.1 - 1

When first prepared, the reaction mixture for a zeolite synthesis consists of a non-equilibrium combination of precondensed oxidic silicon and aluminum precursors. Over a period of time and especially on heating, condensation and hydrolysis reactions occur, leading to a redistribution of the species and a repartition of reaction components between the solid and liquid phase. The enthalpy of the involved reactions is small due to similar bonds in reactants and products. Thus, the equilibration process is kinetically controlled and can lead to the successive formation of increasingly stable phases as a function of time according to the Ostwald step rule.[36]

To achieve the crystallization of the open frameworks of zeolites or zeotypes, usually a hydrothermal pathway has to be chosen.[37] In a typical hydrothermal zeolite synthesis the reactants, containing a silicon source and an aluminum source, are mixed together with a cation source, a mineralizer, e.g. hydroxide or

fluoride, and water. This initial mixture, the so-called gel, contains amorphous components and species in solution. The aqueous reaction mixture is heated in a sealed autoclave, usually at temperatures between 50 °C and 200 °C. Crystallization typically starts after an induction period. Gradually all amorphous material is replaced by an approximately equal mass of zeolite crystals, which can be recovered by filtration, washing and drying.

The chemical processes underlying the experimental procedures of zeolite synthesis were intensively studied and many researchers claimed different mechanistic theories such as solid phase transformations from the amorphous precursors into crystals[1] or processes that involve crystal growth from solution species.[38-40] The actual perspective on zeolite synthesis mechanism does not distinguish between solution mediated processes and rearrangement in the solid phase and emphasizes a high mobility of small reacting species catalyzed by the mineralizer (Figure 1.1.1 - 1). In the proposed mechanism T-O-T bond breaking allows the transport of small species from a domain of amorphous material into the liquid phase. At the same time condensation reactions on the solid phase take place. During the induction period, equilibration leads to elements of local order in the amorphous solid. If the order reaches a certain periodicity, a nucleus for a crystal is generated in the gel. Further growth of the periodic structures and dissolution of the remaining amorphous regions finally lead to the zeolite crystal. The formation of a specific open framework structure in this self-assembly process is mediated by the participating cations (Figure 1.1.1 - 1 center). They are involved in the assembling of the building units at the growth site by acting as coordination centers for water molecules, silicate ions and other polar units and thus provide much of a blue print for the spatial architecture. Using cations of special size or morphologies (e.g. large

organoammonium ions) as so-called structure directing agents (SDAs), in some cases the crystallisation of a certain zeolite framework can be induced.[41-43]
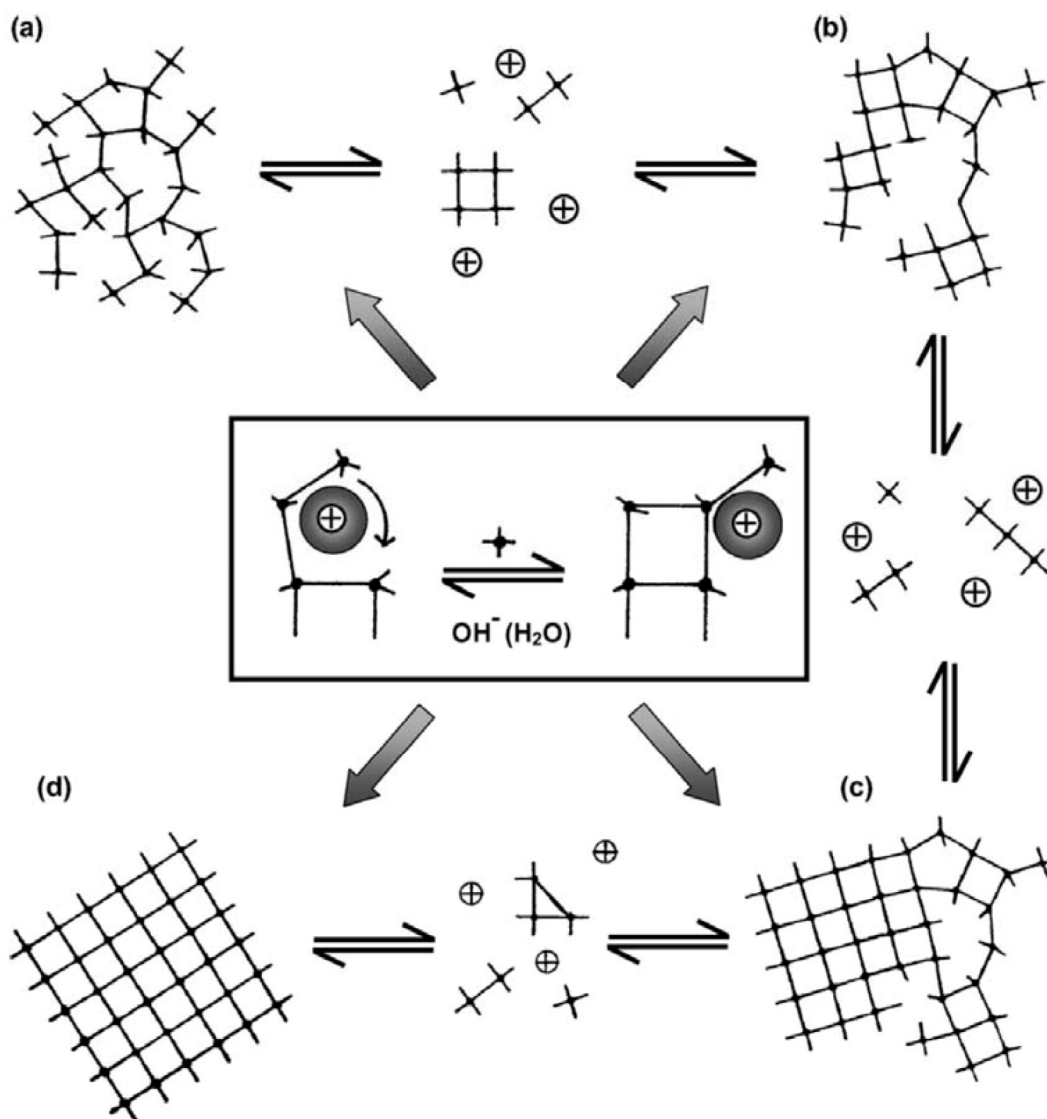
Figure 1.1.1-1: A generalized mechanism for zeolite synthesis relying on T-O-T bond breaking and bond making reactions in an initial domain of amorphous material (a). Equilibration leads to elements of local order (b) which can nucleate localized periodic structures (c). During further equilibration the crystal grows and amorphous regions dissolve (d). The formation of a specific open framework structure in this self-assembly process is mediated by the participating cations which act as templates for the construction of the framework (center).[37]

Applications

Zeolites combine microporosity with a high thermal stability, which explains their successful implementation in many industrial processes. Their main application fields are ion exchange, catalysis and gas separation. Due to their negative framework charge, which is compensated by loosely bound guest ions, many zeolites are strong ion exchangers. They are industrially used as water softener in detergents or for the capturing of particular ions from radioactive waste. Some show molecular sieving effects and are therefore employed in gas separation processes, as for example the separation of n-paraffin from i-paraffin (Union Carbide 1959). However, the most significant application of zeolites nowadays is catalysis. The hydrogen-exchanged forms facilitate many industrial catalytic processes (such as cracking (Mobil Oil 1962), hydrocracking and selectoforming, alkylation, NOx reduction etc.) in their function as powerful solid-state acids.[8] For more recent applications various morphologies of zeolites such as films and membranes, fibers, micropatterns, and nanoparticles have been elaborated, which are expected to have high potential as separation membranes, chemical sensors and hosts for guest species in optical applications. For example, porous zeolite films are considered as a good alternative to dense films for low-k materials in semiconductor devices.

1.1.2 Metal Organic Frameworks

Definition

Metal Organic Frameworks are three-dimensional coordination polymers with open framework architectures. They are composed of organic molecular building blocks that connect inorganic nodes such as transition-metal ions or metal clusters. The molecular building blocks must provide a rigid body that determines the size of the pore and at least two ligand functionalities. The

coordination geometry of the metal in combination with a specific ligand defines the geometry of the structure. For example, the assembly of a tetrahedral metal center and the linear organic linker such as 4,4'-bipyridine results in structures with expanded diamond topology (Figure 1.1.2-1).

History of MOFs

The research field of inorganic-organic hybrid compounds that comprises coordination polymers and metal-organic frameworks was developed during the last 30 years. Early examples are one-dimensional porphyrin coordination polymers with magnetic properties discovered by Basolo in 1970.[44,45] Three-dimensional coordination polymers followed in the late 1970s, when Hardy and coworkers synthesised zeolitic materials with ion exchange properties by linking hexacyanoferrate units with tetrahedrally coordinated Zn^{2+} ions.[46] The first deliberate network design dates back to the work of Robson and Hopkins, who reported in 1989 the substitution of the acetonitrile ligands in $Cu(I)(CH_3CN)_4$ by the tetrafunctional linker 4,4',4'',4'''-tetracyano phenylmethane, which extended the nodes of tetrahedral copper complexes into a three-dimensional network.[47] Yaghi and coworkers performed pioneering work on metal carboxylates,[48,49] and introduced the term metal organic framework (MOF) for coordination polymers with a permanent porosity. They contributed a large number of reviews to the discussion about overall design concepts of this new class of materials. In 2001 the "modular approach" was presented, a concept for the understanding and prediction of the framework topologies of MOFs. This approach is based on secondary building units (SBUs) as synthetic modules for the construction of robust frameworks with permanent porosity.[50] SBUs are frequently recurring structural motifs such as molecular complexes and cluster entities that are defined by the coordination geometry of the participating metals in combination

a) Building Blocks

self
assembly

b) Molecular Complex

c) Extended Framework
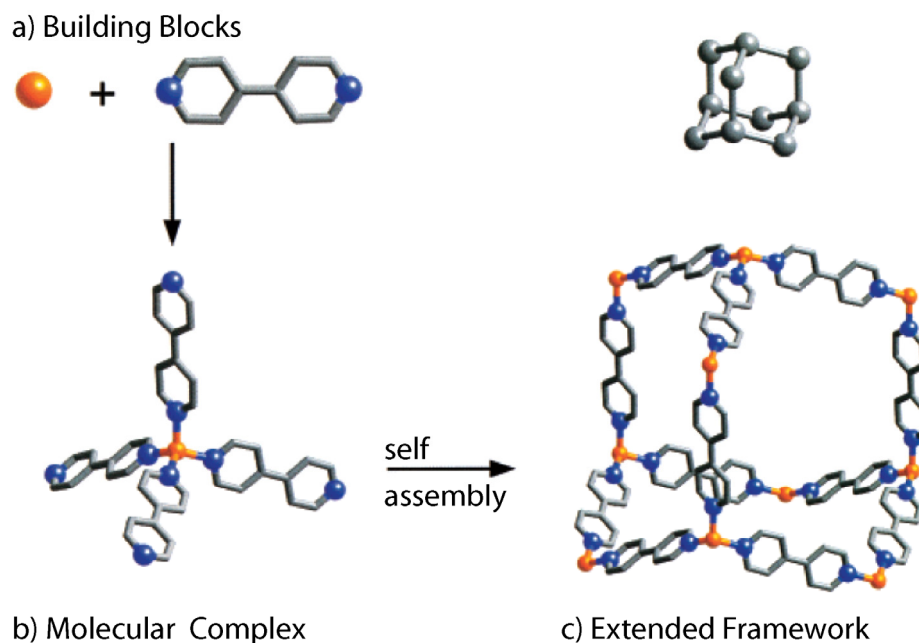
Figure 1.1.2-1: The modular assembly of predefined organic linkers (here 4,4' bipyridine) and metal ions (here Cu(I)) can be used to achieve expanded network architectures.[50]

with the bonding mode of the involved ligands. They represent the nodes of a framework and define its geometry. Varying the rigid linker of the organic building block, one SBU can be transformed into diffrent extended porous networks. The success of this modular design concept could be shown by synthesizing MOF 1-16, a series of isoreticular cubic structures, by combining the tetranuclear zinc carboxylate cluster as SBU with various isotopic ligands.[51,52] A tremendous flood of new MOF structures followed. Most work to date has focused on O and N-based ligands, as many of them are commercially available (Figure 1.1.2.-2 I). Typical linear linkers are dicarboxylates and bipyridines. Triangular topology is provided by trimesic acid and its derivatives. Recent efforts to induce a certain framework not only via a given metal coordination geometry but also via predefined angles in the organic building block led to a series of angular ditopic ligands, as for example 4,5 imidazole dicarboxylic acid.[53]

The most frequently used metal ions today are divalent and trivalent first-row transition metals (e.g. Zn^{2+}, Mn^{2+}, Fe^{2+}, Co^{2+}, Ni^{2+}, Cu^{2+}, Mn^{3+}, Fe^{3+}, Cr^{3+}). They have well-known coordination environments that often depend upon the identity of the ligands. Examples for cluster entities that frequently recur as SUBs include the characteristic paddle wheel dimer, a square Cu^{2+} carboxylate cluster, which can be found in the highly porous 3-D copper trimesate (Cu-BTC)[54]. Similarly, the Zn_4O cluster that is found in basic zinc actetate, $Zn_4O(OCOCH_3)$,[49,52,61] and the trimeric Cr^{3+} cluster, Cr_3O[55] are common building units of MOFs (Figure 1.1.2-2 II).

Recent important developments include the so-called breathing MOFs with dynamic structures, reported as the MIL family (MIL-53, MIL-88 and MIL-101) by Ferey and coworkers.[56-58] These porous metal carboxylate frameworks can reversibly change their cell volumes (some of them by up to 40 %), while the connections between the framework metals (M = Cr^{3+}, Al^{3+}, Fe^{3+}) and the organic linkers remain intact. A similar dynamic behavior was found in the CPL family, which was first described by Kitagawa and coworkers in 1999.[59,60] These stable and porous pillared layer structures usually contain two different types of ligands. For example in CPL-1, Cu^{2+}-ions and pyrazine-2,3-dicarboxylate ligands form two-dimensional sheets that are pillared by pyrazine ligands bridging Cu^{2+} ions of different sheets. They show a shape-responsive fitting for various guest molecules, which improves the efficiency of the adsorption by aiding the host structural transformation suited for incorporating the guest molecules. Another new MOF family is the so called Z-MOF (or ZIF) family, a class of materials with zeolite-like frameworks derived from the coordination of single metal ions by angular ditopic linkers.[53,61] These expanded zeolite structures provide properties that are rather untypical for MOFs such as a negative framework charge and thus rather strong guest-framework interactions. A related class of porous hybrid materials was introduced by Yaghi et al. in 2005.
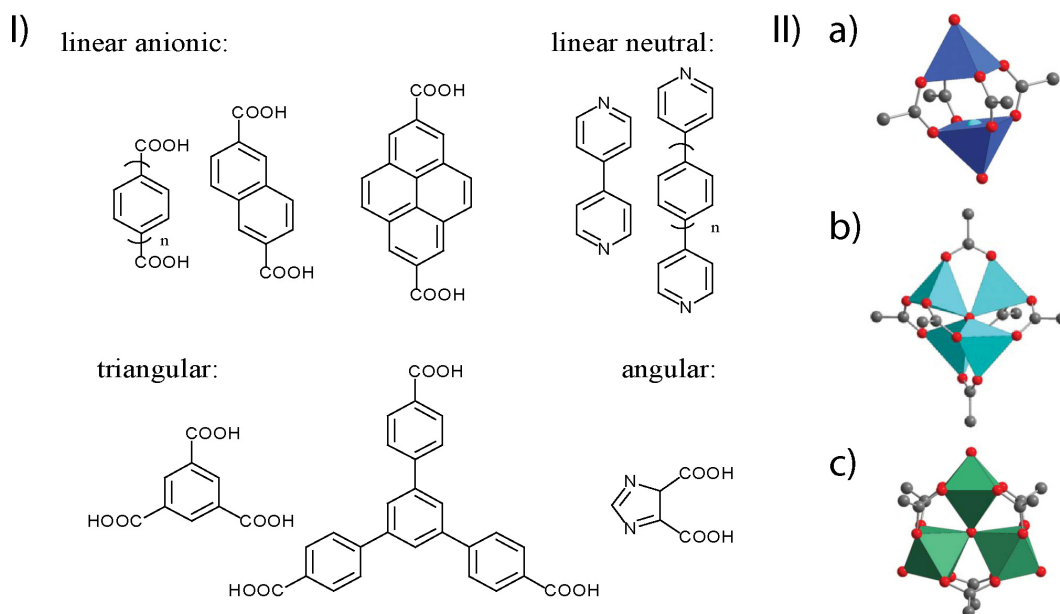
Figure 1.1.2-2: I) Common organic building blocks of MOFs; II) Commonly recurring secondary building units SBUs: a) the "paddle wheel" dimer of CuO_5 square pyramids, b) the tetrahedron of ZnO_4 tetrahedra sharing a central oxygen, c) the trigonal planar trimer of CrO_6 octahedra sharing a central oxygen.

Covalent organic frameworks (COFs)[62,63] were obtained by condensation of organoboronic acids with polyols, which present a more covalent bonding in comparison to the ionic nature of metal-ligand interactions in MOFs.

Lanthanide based MOFs

Lanthanide coordination frameworks have been far less studied than their d-block metal counterparts.[64,65] One reason for this might be the coordination chemistry of the lanthanide elements themselves. In contrast to the d-metals where predictable coordination geometries may be anticipated, the coordination sphere of lanthanides is difficult to control. Ln elements tend to have larger coordination numbers (typically 8-12), are primarily ionic in their bonding and display no crystal field effects, thus resulting in spherical coordination geometries (Figure 1.1.2-3). The absence of design strategies for lanthanide

MOFs makes it far more difficult to target materials with specific properties. On the other hand their higher connectivity and greater flexibility led to unanticipated structures with unusual eight,[66,67] seven[67] and five[68] connected framework systems, which are rarely or not accessible with d-metals.

An illustrative example was recently reported by Li and coworkers, who described a series of new microporous lanthanide MOFs, [Ln(BTC)(DMF)$_2$·H$_2$O), Ln = Tb, Dy, Ho, Er, Tm, Yb], with zeolite topology.[69] They exhibit all the same three-dimensional architecture assembled by organic and inorganic four connected nodes (Figure 1.1.2-4 I). The inorganic node consists of Ln^{3+} ions and four carboxylate ligands of benzene tricarboxylic acid (BTC). However, the coordination number of the lanthanide ions in these structures is eight. Besides six oxygens of two mono- and two bidentate chelating carboxylate ligands, two oxygens from terminal dimethyl formamide molecules form part of the metal complex (Figure 1.1.2-4 II). Though the overall network is very attractive, its formation has not been anticipated as the coordination of the lanthanide ion is not controlled by a specific metal ligand coordination geometry, but rather random.
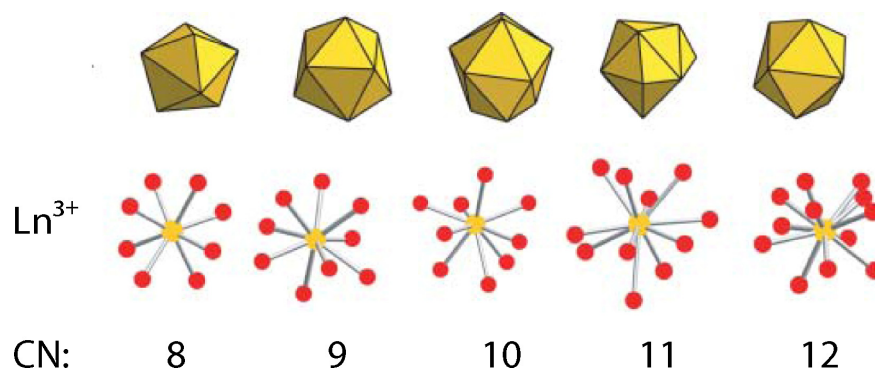
Figure 1.1.2-3: Coordination geometries for the lanthanide elements.
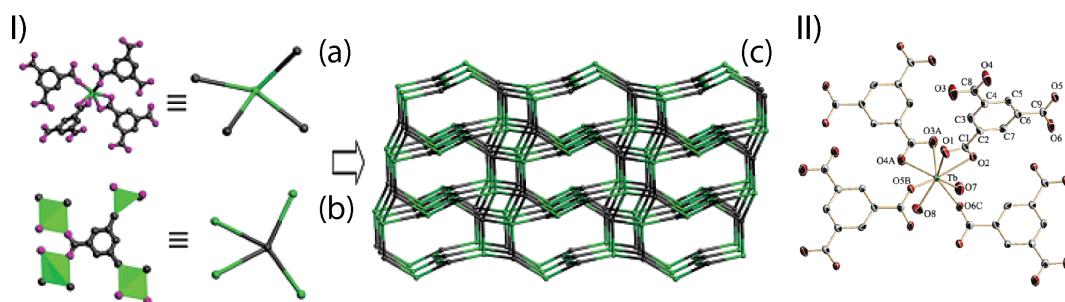
Figure 1.1.2-4: I) Framework of Tb(BTC)(DMF)$_2\cdot$H$_2$O: Tb^{3+} coordinated by four BTC ligands (a) and the phenyl group of BTC coordinated through two chelating bidentate and two monodentate carboxylate groups (b) can both be regarded as four-connected nodes which build a zeolitic framework (c). II) Full coordination sphere of Tb^{3+}.

Another interesting aspect regarding the synthesis of lanthanide based MOFs was observed by Cahill and coworkers.[65] They prepared a series of three-dimensional lanthanide adipate frameworks. During synthesis they offered two types of ligands, the harder carboxylate function of the adipate molecule and softer nitrogen ligands of pyridine derivatives. They observed that only carboxylate and solvent water coordinated to the metal while the pyridine-derived molecules were found as guests in the pores. Different guest molecules templated various structures forming hydrogen bonds to the framework and could be further used as sensitizing species for the excitation of light emission of the lanthanides. The same preference of lanthanide ions for hard ligands was used by Champness and coworkers for the formation of five, seven and eight connected networks.[64] Using organic linkers with hard N-O functional groups as ligating group, they achieved exclusive coordination of the framework lanthanide by the provided organic building block and avoided solvent coordination.

MOF Synthesis

Due to the geometrical restrictions of the predefined building blocks, the self-assembly of MOFs is much more predictable than the formation of zeolites, where [SiO$_4$] tetrahedra can assemble in numerous ways. Therefore, during the search for new structures emphasis has been placed rather on choosing adequate ligand/metal combinations than on the systematic exploration of crystallization conditions. Furthermore, the numerous possibilities of metal/ligand/solvent combinations make a generalization difficult. Nevertheless, some trends have been observed and described up to now: Often the first and most time-consuming step in MOF synthesis is the preparation of the organic building block, if the latter is not commercially available. The second step is the crystallization of the metal organic framework from the chosen building blocks, while preventing uncontrolled precipitation of amorphous material. This succeeds sometimes at room temperature using solvent diffusion methods or, more typically, using solvothermal methods at higher temperatures (75-200 °C) under autogeneous pressure. A crucial prerequisite for the successful crystallization of the desired framework is finding the adequate reaction medium. Depending on the solubility of the organic ligand and the metal salt, besides water other polar solvents or solvent mixtures are used, most commonly alcohols, dialkyl formamides and pyridine. Thereby crystallization often proceeds from clear solutions of the precursors, or from heterogenous mixtures of ligand solutions and a partially dissolved metal salt. The conversion of amorphous precursor gels into crystals, as it is described for zeolites, has not been reported for MOFs. Time-dependent effects are rarely reported in MOF synthesis. An exemplarily systematic high-thorughput study on cobalt succinates reveals very little effects as a function of time.[70] This points to the likelihood that kinetic control is of less importance in MOF synthesis than it was

found to be in the case of zeolites. This conclusion is straightforward, as in the case of aluminosilicate zeolites, crystallizations and transformations involve the making and breaking of strong Si-O or Al-O bonds, whereas the metal-ligand bonds (e.g. M-O, M-N) in MOFs are relatively weak. However, transformations from one framework into another could play a role if various inorganic SBUs are available in one metal/ligand system, as it is the case in the MIL family. Further investigations will be necessary to reveal possible transformations between those frameworks. Consequently, the pertinent chemical parameters of MOF synthesis in a defined reaction medium are the pH, which provides the respective ligand in an adequate degree of deprotonation, the concentration, which influences the formation of crystal nuclei and growth, and the temperature. The influence of reaction temperature on hybrid framework formation was studied in a series of experiments where cobalt(II) hydroxide was reacted with succinic acid in a 1:1 molar ratio at five temperatures between 60 °C and 250 °C.[70] Remarkably, this yielded a series of five different phases that became more dense and less hydrated with increasing temperature, transitioning from a hydrated 1-D coordination polymer at the lowest temperature to an anhydrous 2-D hybrid metal-oxide at the highest. This showed for the first time that hybrid framework formation is strongly influenced by classical thermodynamic factors, such as condensation due to entropy-driven dehydration reactions at higher temperatures. A good example for the influence of the pH on the formation of a specific network is the work of Stock and Bein on manganese with the phosphonocarboxylic acid, p-$H_2O_3PCH_2$-C_6H_4-CO_2H.[71] At low pH values only one oxygen of the phosphonate group is deprotonated and the system is limited to forming a one-dimensional coordination polymer. As the pH is raised, the second proton of the phosphonate group is released and the dimensionality increases to form a two-dimensional coordination polymer,

while at the highest pH, the carboxylate becomes deprotonated and the dimensionality can increase to 3D.

Applications

MOFs have a lower thermal and chemical stability than most zeolites and are probably more expensive in production. Therefore they often cannot surpass the latter in their traditional fields of application. However, this new generation of materials excels in particular specialized applications in the field of gas storage, gas separation, catalysis and sensing.[72] Their often neutral frameworks provide large non- or weakly polar pores that allow the uptake of considerable amounts of small molecules. For example, the amount of methane that can be stored in the cubic framework of IRMOF-6 at 36 atm is (based on volume) 70 % of the amount stored in gas cylinders, where much higher pressures (256 atm) have to be applied.[51] Recently, the hydrogen storage capacities of MOFs have been intensively studied,[73] as well as the selectivity of several dynamic structures for particular guests.[74,75] Free coordination sites at the framework metal or targeted functionalized groups connected to the organic spacer are potential reactive centers for catalytic applications.[76] Recent studies of thin MOF films grown on self assembled monolayers (SAMs) demonstrate how these materials can be tailored for potential sensing applications.[77] Another way of inducing function in MOF materials is via the framework metal. Lanthanide ions, for example, show magnetic and luminescent properties related to their f-electrons. As the f-elctrons show a core-like behaviour and do not participate significantly in bonding, the electronic spectra and magnetic properties of the ions are largely independent of environment and can therefore be potentially transferred to many structure types.[65,78,79]

1.1.3 Metalphosphonates

Classification

Metal phosphonates can be conceptually positioned between zeotype materials (e.g. aluminophosphates) and metal organic frameworks. Similar to the phosphate ion $[PO_4]^{3-}$, the phosphonate ion $[R-PO_3]^{2-}$ forms extended inorganic networks with numerous metal ions. Certainly it must be considered that the connectivity is reduced from four to three and that the structures are strongly influenced by the size and shape of the organic units that have to be accommodated. On the other hand numerous coordination complexes with phosphonate or phosphate ligands are described, and well established synthesis routes are known to allow a tailored design of organic molecules with phosphonate functionalities.[80] The latter features both point to phosphonic acids as potential candidates for building blocks of metal organic frameworks.

Most closely related with zeolites are probably metalphosphonates that are based on phosphonic acids with very small organic groups.[81] In these materials the phosphonate functionality connects the metal ions into an extended inorganic network, while the organic moieties point into the pores. The first 3D open framework metalphosphonate, β-Cu(O$_3$PCH$_3$), which provides a 1 D channel system with methyl groups lining the pores was reported by Le Bideau in 1994 (Figure 1.1.3-1a).[82] In the same year two other members of this familiy with the framework composition Al$_2$(OPCH$_3$)$_3$ were reported by Maeda.[84,85] The polymorphs Al-MePO-α and Al-MePO-β both are composed of one AlO$_6$ octahedron, three AlO$_4$ tetrahedra and six methylphosphonates with different manners of connectivity. The corner sharing aluminates and phosphonate units form three-dimensional open frameworks with one-dimensional channels of about 7 Å lined by the methyl groups.
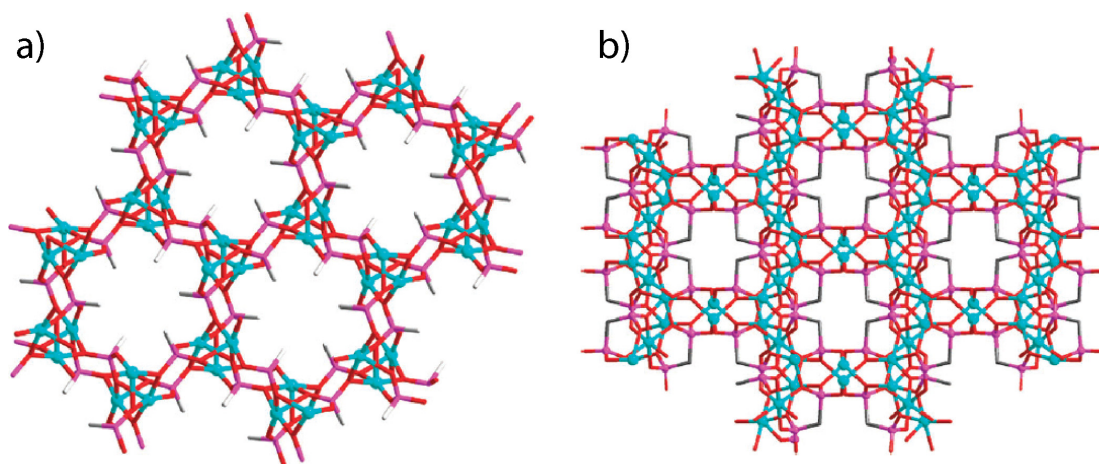
Figure 1.1.3-1: a) Three-dimensional open framework structure of copper methyl phosphonate showing the methyl-decorated 1-D channels running along the framework. b) 3-D open framework structure of the nickel phosphonate $Ni_4(O_3PCH_2PO_3)_2\cdot2H_2O$ (VSB-3) showing the methylene groups of the phosphonate ions decorating the channels of the inorganic framework constructed of NiO_6 and NiO_4 polyhedra. Color scheme: Cu-cyan; P-purple; O-red; C-grey.[83]

The microporous nature of both materials was proven by nitrogen adsorption. This approach could be extended to methylenediphosphonic acid. The three-dimensional open framework structure of $Co_2(O_3PCH_2PO_3)\cdot H_2O$ showed one dimensional channels lined with methylene bridges.[86] Another representative example is VSB-3, a nickel phosphonate $[Ni_4(O_3PCH_2PO_3)_2\cdot2H_2O]$ with thermal stability up to 575°C and ferromagnetic interactions between the Ni centers.[87] The skeleton of VSB-3 can be visualized as sheets of NiO_6 trimers cross-linked in the third dimension by corner sharing NiO_4 tetrahedra. (Figure 1.1.3-1b) This framework is then extensively decorated by the bridging P-CH$_2$-P units, which point into narrow pores. However, these three-dimensional inorganic frameworks are quite an exception in metalphosphonate chemistry as this approach is limited to the smallest phosphonic acid building blocks. Efforts to prepare networks using ligands with longer alkyl chains from the type H_2O_3P-

$(CH_2)_n$-PO_3H_2 with $n \geq 2$ showed that in most cases the formation of layered structures becomes predominant.

The structural layer motif is, without doubt, the most prevalent in metal phosphonate chemistry. Layered metal phosphonates have been intensively studied and reviewed by Alberti and Clearfield since the 1970's.[88] Initially metalphosphates were studied as inorganic layered solids, which evolved into the field of inorganic-organic hybrids by appending organic groups off the rigid inorganic layers. A representative example is zirconium phosphate (Figure 1.1.3-2a). In the structure of α-$Zr(HPO_4)_2$ the zirconium ions lay slightly above and below the mean plane of a layer and are bridged by phosphate groups above and below. Three oxygen atoms of a phosphate group are bonded to three different zirconium ions. The fourth oxygen bonds to a proton and points into the interlayer space. When substituting the phosphate ion by phosphonate ions, e.g. phenylphosphonate, the inorganic layer structure stays intact and the -OH group is exchanged by the organic group modifying the interlayer distance. This exchange makes the interlayer, where guest molecules can be introduced, tunable as it can range from hydrophilic to hydrophobic depending on the organic part of the phosphonic acid employed. By using difunctional phosphonic acids, the inorganic layers can be connected into the third dimension, thus generating so-called pillared materials (Figure 1.1.3-2b). Pillared layers are usually dense solids. Porosity can be introduced into these materials by replacing some phosphonates with a monofunctional group (e.g. phosphate or small monophosphonates) in order to create some interlayer space.[90] The problem with this approach is that the substitution is random, thus although a porous phosphonate can be formed, structural characterization and defined pore sizes remain a challenge.
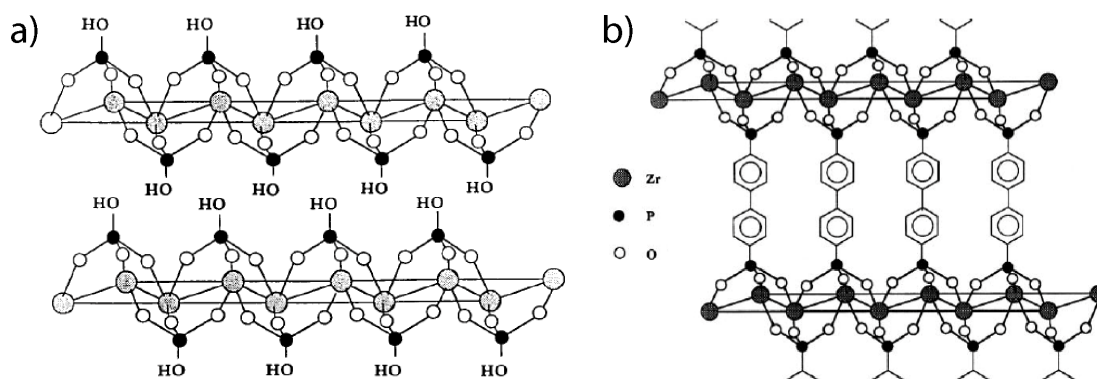
Figure 1.1.3-2: a) layered structure of zirconium phosphate (α-Zr(HPO$_4$)$_2$);[88] b) schematic representation of Zr(O$_3$PC$_{12}$H$_8$PO$_3$)$_2$ showing the expected pillared structure.[89]

Clearly there exists a parallel to MOF chemistry. Therefore, with the MOF boom starting in the 90's, many efforts have been made to prepare phosphonic acids with two or more phosphonic acid groups separated by a rigid organic spacer. Representative examples are shown in figure 1.1.3-3. These ligands, which are tolopogically related with MOF building blocks based on carboxylates, were tested in metal organic framework synthesis. However, the rigid organic spacer in most of the obtained new structures with the building blocks **I-IV** showed the default structure for metal phosphonates: a layered assembly.[88,91-98] This behaviour can be attributed to the versatile bonding modes of the phosphonate group, which can coordinate via each of its three oxygen atoms and thus, act as mono or bidentate ligand, or as a combination of both to one, two or even three metal ions. Depending on the synthesis conditions, and on the needs of the structure to be formed, the phosphonic acid can be converted into its mono-deprotonated or its fully deprotonated form, which further increases the number of possible assemblies. In most cases this flexibility allows the metal phosphonate groups to pack efficiently in inorganic layers.
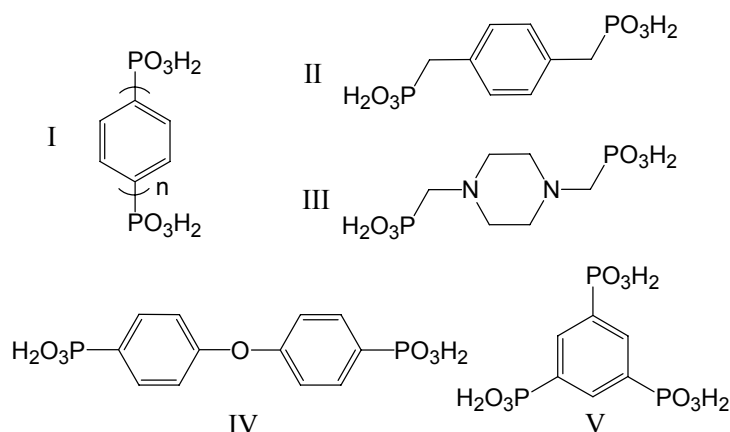
Figure 1.1.3-3: Phosphonic acids prepared for the synthesis of coordination polymers.

Frequently recurring SBUs with a defined metal-phosphonate ligation have not been observed yet. In contrast to metal carboxylates or metal amines, this makes organometalphosphonate chemistry less predictable, and control over the formation of geometrically well-defined structures has not been obtained yet. Only few crystalline three-dimensional coordination polymers with open frameworks have been described up to now.[99,100]

One approach for forming pores in metalphosphonates is to employ a large multidirectional ligand that would completely disfavour the formation of a layered inorganic motif. 1,3,5,7-tetrakis(4-phenylphosphonic acid) adamantane is such a molecule as it possesses four phosphonic acid moieties spaced by rigid phenyl groups from an adamantane core. Taylor reported the crystal structure of the Cu^{2+} network of this ligand, $[Cu_3(H_3L)(OH)(H_2O)_3] \cdot H_2O \cdot MeOH$, that consits of trigonal trinuclear copper clusters linked by the organic spacer into a diamondoid net (Figure 1.1.3-4a).[101] The cluster was composed of three copper centers coordinated by three separated phosphonate groups and capped by a fourth one to create a pseudo tetrahedral arrangement of phosphonates. The other side of the cluster contains a μ_3-hydroxyl group to charge balance. The

network is doubly interpenetrated but the bulky copper clusters resulted in voids filled with water and methanol and CO_2 sorption revealed a BET surface of 200 m^2g^{-1}. The main outcome of this work was to show that in metal phosphonate chemistry the organic linker can in fact determine the inorganic aggregation, as new metal clusters were formed as required by the diamondoid topology. A similar accessible core unit was observed by Clearfield and coworkers using 1,3,5-benzentriphosphonate,*V*, which is an analogue to trimesic acid.[102] The trigonal substitution of the benzene ring in this compound should again disfavour the simple layered motif. Combining this ligand with copper ions, the compound $Cu_6[C_6H_3(PO_3)_3](H_2O)_8$ was formed, a highly hydrated network with six negative charges on the ligand and tetracopper clusters as building units. Porosity was not examined for this material.

Sterical hindrance imparted by the ligand can also lead to an open framework. While 1,4 benzenediphosphonic acid **I** readily forms layered structures with most metals, 1,4-dihydroxy-2,5-benzenediphosphonic acid (DHBP) with Zn^{2+} ions in DMF yielded a three-dimensional open framework $Zn(H_2L)(DMF)_2$ with homoleptic PO_3 coordination and permanent porosity.[100] The organic groups of the linker protrude in four directions from one-dimensional columns of phosphonate-bridged zinc centers to form a square grid (Figure 1.1.3-4b). XRD and TGA measurements showed that the network is stable up to a loss of about 80% of the included DMF molecules. CO_2 and N_2 sorption analysis gave BET surface areas of 216 and 209 m^2g^{-1} respectively. The free hydroxyl group in this compound represents a potentially reactive site for post-synthetic modification. Nowadays the phosphonate functionality is often used in combination with other functional groups including imino, hydroxyl, carboxylic acid, sulfonic acid and pyridine.[95,103-110] The new functional group on the organophosphonate ligand is thereby expected to perturb the layered structure in metaldiphosphonates, with the result hopefully being a new three-dimensional open framework.
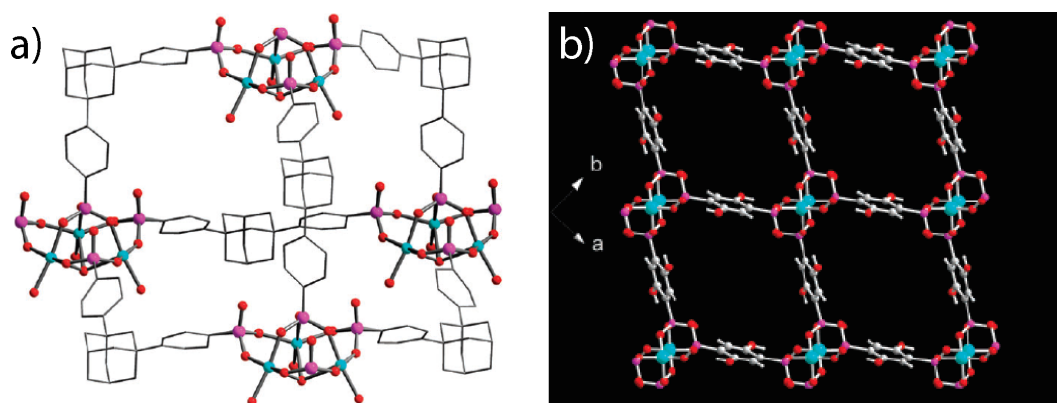
Figure 1.1.3-4: a) Crystallographic representation of a diamondoid cage formed from the 1,3,5,7-tetrakis(4-phenylphosphonic acid)adamantane tetrahedron and pseudo-tetrahedral tricopper clusters. The network is twofold interpenetrated. [83] b) Cross section of the crystal structure of [Zn(DHBP)](DMF)$_2$ showing the pores. Guest molecules are not represented. [100] Cu-cyan; P-purple; O-red; C-grey.

A successful example for this strategy is NiSTA-12, a Ni-N,N'-piperazine-bis(methylenephosphonate). The structure can be broadly described as helical chains of edge-sharing NiO$_5$N octahedra linked into a honeycomb arrangement by the ligand. The specific pore volume of the dehydrated form of NiSTA-12 is comparable to those in zeolite beta and the network showed a tenfold higher uptake for CO$_2$ over CH$_4$.

An indication for the potential of lanthanide phosphonates was given using the polyfunctional linker, N,N'-piperaziniumbismethylenephosphonate **(IV)**. Two polar three-dimensional open frameworks were obtained by combining this linker with lanthanum chloride. [111] Both frameworks were made up from one-dimensional lanthanide phosphonate chains connected in three dimensions by the piperazinium backbone, which imparted a macro cationic nature on the framework. The three-dimensional network contained channels lined by the piperazinium and phosphonate units and occupied by Cl- ions. No data is available on the porosity of this compound. This promising structure indicates

that the phosphonate functionality might be a good ligand choice for the construction of MOFs from metals with high coordination numbers.

Synthesis of Phosphonate based MOFs

As metalphosphonates are positioned between zeolites and classical MOFs, synthetic aspects from both types of materials have to be considered. Phosphonic acids precipitate immediately with many metal ions forming amorphous solids. Therefore classical diffusion methods are often not suitable if a good crystalline product is targeted and hydrothermal procedures are the method of choice. The formation of a homogeneous gel of the precursors can sometimes have an influence on the purity of the desired phase. Reaction media have to be more polar than in the case of carboxylate or amino ligands and a low pH is intrinsic and suitable. Templating is much more common than in classical MOF syntheses. All this leads to an increase of the number of variable synthesis parameters, which can be addressed best by a systematic high-throughput approach.

Potential Applications of Phosphonate based MOFs

In contrast to other MOF materials phosphonates would offer a much greater likelihood of forming polar pores. This would translate into different selectivities for the sorption of guest molecules than observed for non-polar pores that are much more typically observed in MOFs. Other applications of materials with polar pores would be ion exchange or ion conductors, both aspects that have not been extensively studied in MOFs. Given that the variable deprotonation degree of phosphonates might enhance certain ion mobilities in the solid state, a material such as a phosphonate MOF would be an intriguing candidate. A high chemical and thermal stability and the ability to complex high-valent ions is another feature of interest. However, regarding the potential applications of

phosphonates, of course new materials with regular micropores would be required. Clearfield and coworkers already demonstrated that porosity in pillared layers can be achieved (up to now 400 m^2g^{-1} in Sn(IV) phosponates).[89,112] But the low crystalline character and the undefined pores of these materials complicate the investigation of their host-guest chemistry. Well-defined crystalline phosphonate based MOFs could overcome this problem.

1.2 High Throughput Methods in Material Synthesis

New and optimized functional materials provide a basis for technological progress. Due to the fast-growing competition in a global market they are subjected to constantly faster development cycles. To satisfy the short development periods in a global environment, new technologies for efficient material design have to be investigated and implemented. For this purpose high-throughput (HT) methods are a successful example.[113] They comprise the fast and automated discovery, investigation and optimization of unknown and known substances by combining design of experiment, fast synthesis, high-throughput screening and the handling of large amounts of data with the aim to generate, analyze and characterize a large number of materials with varying compositions. This is expected to result in shorter times of development, higher rates of success and better reproducibility. The generation of a large variety of new materials by defined variation of chemical compositions and process parameters led to the exploitation of numerous parameter spaces and thus, more knowledge. HT methods were rapidly developed during the past 30 years initially from universities and a few pioneering companies, followed soon by industry with increased emphasis. In retrospect, the first publications reporting a systematic approach that would today be associated with high-throughput

experimentation, were contributed by Edison (1878), Ciamician (1912) and Mittasch (BASF, 1909); the latter described the development of a catalyst for the ammonia synthesis.[114] In 1970 Hanak introduced the first gradient libraries for the R&D department of RCA laboratories[115] and in 1980 Moulijin published the first article about a parallel reactor system for heterogeneous catalysis.[116] First studies that focus on high throughput as research topic were realized at universities in the USA, e.g., at UC Berkeley at the beginning of the 90's in the field of superconductors.[117] These activities led to the foundation of the company Symyx, which has become a market leader in HT applications today. At the same time HT projects were reported from the chemical industry (GE, Dupont, Avery-Dennison, Exxon, DOW, UOP).[118] In Japan and Korea HT methods were implemented with broad public investment in the investigation of materials for electronic devices or communication technology. In Europe the initial engagement came from industry (Hoechst, Bayer, Siemens, BASF, Shell), initially in combination with service providers such as Symyx, later in internal HT projects. At the same time the first European start-up companies were founded, such as hte (Germany), avantium (Netherlands) or Accelab (Germany). This was accompanied by public programs that initiated cooperations between industry and universities. In 2003 the world market for high throughput technologies and related services were estimated to one billion Euros every year.[119] Today HT technologies are established in several fields of materials science and are applied in the research regarding many types of materials, such as catalysts, electronic devices, magnetic devices, polymers, materials for optical applications, biomaterials, colors, pharmaceuticals, detergents, cosmetics and adhesives.[113]

However, many relevant materials and especially porous materials such as zeolites or inorganic organic hybrid materials are based on chemistry in solution, which poses still many challenges on high throughput methods due to

its complexity. Many of these materials emerge from hydrothermal processes, which are sensitive to a multitude of different parameters for experimental conditions such as high temperatures, pressures, pH values, solvent properties, preparative processes such as the dosing of the reactants, mixing procedures, aging times and work-up procedures such as washing, filtration and drying. To control all these parameters in an integrated workflow is a complex task. On the other hand, by synthesizing and processing these materials numerous open questions can be addressed, such as the nature of active centers, the relationship between activity and process parameters, the possible formation of metastable phases, reproducibility and scalability. In this context a systematic HT parameter screening can be a powerful tool. Since Akporiaye, Bein and Klein implemented HT methods for hydrothermal synthesis in the field of zeolites,[120,121] they and others have proven their potential also in the field of inorganic organic hybrid compounds, e.g., metal carboxylates,[70,122] metalphosphonates[123] and zeolitic imidazolate frameworks[124] and thus substantially contributed to the collection of some key parameters for the understanding of the crystallization conditions of these new and exciting materials. Nevertheless, in academia HT methods are still not established as standard laboratory technology. The following work relies on these techniques to accelerate the discovery of new phases and the optimization of their synthesis conditions. Although the development of HT methods itself was not the aim of this project, the encountered questions were faced by applying a high-throughput approach with the aim to single out positive hits in the screened parameter spaces, and to define ranges and dead ends with certain synthetic approaches.

1.3 Goals

As stated previously, the phosphonate functionality has strong complexation abilities towards many metal ions. Nevertheless its versatile bonding modes and its freedom of rotation in many potential building blocks have prevented a breakthrough of phosphonate-based linkers in the synthesis of open framework materials. The following work contributes to a better performance of phosphonates in metal organic frameworks synthesis. Therefore the initial goal was the development of a new type of building block (Chapter 3). Instead of single phosphonate functionalities it should contain bisphosphonate groups and thus provide large chelating ligands that might bond more specifically to suitable metal centers. Moreover the functional groups should be connected without freedom of rotation to a rigid organic spacer in order to restrict the possibilities of a free assembly of the molecule.

The new ligand 1,4-phenylenebis(methylidyne)tetrakis(phosphonic acid) should then be tested in hydrothermal synthesis as building block for metal organic frameworks (Chapter 4). For this purpose the molecule was combined with lanthanide(III) ions as corresponding metal centers. As discussed above, lanthanide containing MOFs are very promising due to the luminescent and magnetic properties related to their f-electrons but challenging in synthesis. The large bisphosphonate chelate ligand was anticipated to accomplish the requirements of their large ionic radii and to control their versatile coordination modes. A systematic high throughput approach should help to gain an overall understanding of the performance of both components. Using a high-throughput work flow a discovery library should be generated that provides information about the influence of stoichiometry, pH and temperature on the crystallization of possible new compounds. The library should be evaluated by XRD, scanning electron microscopy and EDX analysis. Representative positive

hits should be further characterized with single crystal structure analysis, Raman spectroscopy, thermogravimetric and full elemental analysis. All information was intended to merge into a comprehensive description of the crystallization fields in the screened parameter space.

Once a new MOF material is synthesized and the process parameters that lead to its formation are fully under control it becomes interesting to test its properties as functional material. In the case of a porous material such an investigation is closely related to the investigation of its host guest interactions. Chpater 5 and 6 focus on the understanding of the relation between the framework and the guests of **NaLa(H$_4$L)**, a lanthanide(III)tetrakisphosphonate that turned out to be the most promising positive hit in the discovery library.

As lanthanide phosphonates are expected to have a more polar network than common neutral MOFs, it would be highly interesting to show their performance in an application rather untypical for MOFs, such as ion exchange. Thus, ion exchange and hydration/dehydration properties of **NaLa(H$_4$L)** were studied and discussed against the backround of the flexible framework of the structure. In this context Lynne McCusker from the ETH Zürich contributed a Rietfeld refinement of the structure of a dehydrated sample of **NaLa(H$_4$L)** (Chapter 5).

Usually the structures of metalorganic frameworks are defined by the coordination geometry of the framework metal in combination with the organic ligand. Guest molecules play a minor role and templating effects are rarely observed. The anionic framework of NaLa(H$_4$L) includes Na$^+$ ions that have shown to be important for the network formation. These circumstances afforded the opportunity to investigate the influence of various cationic guests on the synthesis of the anionic host structure using a high-throughput approach (Chapter 6).

Furthermore, in Chapter 6 the sorption properties of thus prepared materials with the general formula **MLa(H$_4$L)** were studied and water sorption isotherms are discussed with respect to the guest ions in the structure.

Solving the aforementioned tasks, starting with the synthesis of a new phosphonate building block *via* its successful implementation in MOF synthesis with lanthanides to the characterization of the material properties of an open framework lanthanum tetrakisphosphonate would essentially promote the role of metal phosphonates in the family of metalorganic open framework materials.

1.4 References

(1)   Cundy, C. S.; Cox, P. A. *Chem. Rev.* 2003, *103*, 663-702.

(2)   Cronstedt, A. F. *Academiens Handlingar Stockholm* 1756, *18*, 120.

(3)   Damour, A. *Annales de mines* 1840, *17*, 191.

(4)   Eichhorn, H. Annalen der Physik und der Chemie 1858, 105, 126.

(5)   O. Weigl, E. S. Z. Kristallogr. Kristallgeom. Kristallphys. Kristallchem. 1925, 61, 125.

(6)   Pauling, L. Z. Kristallogr. Kristallgeom. Kristallphys. Kristallchem. 1930, 74, 213-25.

(7)   Barrer, R. M. *J. Chem. Soc.* 1948, 2158-63.

(8)   Flanigen, E. M. *Introduction to zeolite scince and practice*; Elsevier: Amsterdam, 1991.

(9)   Barrer, R. M.; Denny, P. J. *J. Chem. Soc.* 1961, 971-82.

(10)   Kerr, G. T.; Kokotailo, G. T. *J. Am. Chem. Soc.* 1961, *83*, 4675.

(11)   Kerr, G. T. *Inorg. Chem.* 1966, *5*, 1537-9.

(12)   Wadlinger, R. L.; Kerr, G. T.; Rosinski, E. J. US 3308069, 1967.

(13)   Flanigen, E. M.; Bennett, J. M.; Grose, R. W.; Cohen, J. P.; Patton, R. L.; Kirchner, R. M.; Smith, J. V. *Nature* 1978, *271*, 512-16.

(14)   International Zeolite Association: Database of Zeolite Strucutres 2009

(15)   Millini, R.; Carati, A.; Bellussi, G. *Zeolites* 1992, *12*, 265-8.

(16)   Klotz, M. R. US 836,403 1981.

(17)   Barrer, R. M.; Baynham, J. W.; Bultitude, F. W.; Meier, W. M. *J. Chem. Soc.* 1959, 195-208.

(18)   Kuehl, G. H. *J. Inorg. Nucl. Chem.* 1971, *33*, 3261-8.

(19)   Notari, B. *Adv. Catal.* 1996, *41*, 253-334.

(20)   Wilson, S. T.; Lok, B. M.; Messina, C. A.; Cannan, T. R.; Flanigen, E. M. *J. Am. Chem. Soc.* 1982, *104*, 1146-1147.

(21)   Lok, B. M.; Messina, C. A.; Patton, R. L.; Gajek, R. T.; Cannan, T. R.; Flanigen, E. M. *J. Am. Chem. Soc.* 1984, *106*, 6092-3.

(22)   Parise, J. B. *Inorg. Chem.* 1985, *24*, 4312-16.

(23)   Dhingra, S. S.; Haushalter, R. C. *J. Chem. Soc., Chem. Commun.* 1993, 1665-7.

(24)   Natarajan, S.; Attfield, M. P.; Cheetham, A. K. *Angew. Chem., Int. Ed. Engl.* 1997, *36*, 978-980.

(25)   Adair, B. A.; De Delgado, G. D.; Delgado, J. M.; Cheetham, A. K. *Angew. Chem., Int. Ed.* 2000, *39*, 745-747.

(26)   Haushalter, R. C.; Mundi, L. A. *Chem. Mater.* 1992, *4*, 31-48.

(27)   Soghomonian, V.; Chen, Q.; Haushalter, R. C.; Zubieta, J.; O'Connor, C. J. *Science* 1993, *259*, 1596-9.

(28)   Chen, J.; Jones, R. H.; Natarajan, S.; Hursthouse, M. B.; Thomas, J. M. *Angew.Chem.* 1994, *106*, 667-8

(29)   Neeraj, S.; Noy, M. L.; Cheetham, A. K. *Solid State Sci.* 2002, *4*, 397-404.

(30)   Huang, Q.; Ulutagay, M.; Michener, P. A.; Hwu, S.-J. *J. Am. Chem. Soc.* 1999, *121*, 10323-10326.

(31)   Guillou, N.; Gao, Q.; Nogues, M.; Morris, R. E.; Hervieu, M.; Ferey, G.; Cheetham, A. K. *C. R. Acad. Sci., Ser. IIc: Chim.* 1999, *2*, 387-392.

(32)   Kemnitz, E.; Wloka, M.; Trojanov, S.; Stiewe, A. *Angew. Chem., Int. Ed. Engl.* 1996, *35*, 2677.

(33)   Bortun, A. I.; Khainakov, S. A.; Bortun, L. N.; Poojary, D. M.; Rodriguez, J.; Garcia, J. R.; Clearfield, A. *Chem. Mater.* 1997, *9*, 1805.

(34)   Davis, M. E.; Saldarriaga, C.; Montes, C.; Garces, J.; Crowdert, C. *Nature* 1988, *331*, 698-699.

(35)   Estermann, M.; McCusker, L. B.; Baerlocher, C.; Merrouche, A.; Kessler, H. *Nature* 1991, *352*, 320.

(36)   Van Santen, R. A. *J. Phys. Chem.* 2002, *88*, 5768.

(37)   Cundy, C. S.; Cox, P. A. *Microporous Mesoporous Mater.* 2005, *82*, 1.

(38)   Kerr, G. T. The Journal of Physical Chemistry 1966, 70, 1047.

(39)   Kerr, G. T. *Zeolites* 1989, *9*, 451.

(40)   Zhdanov, S. P. *Molecular Sieve Zeolites - I*; ACS, 1971; Vol. 101.

(41)   Kubota, Y.; Helmkamp, M. M.; Zones, S. I.; Davis, M. E. *Microporous Mater.* 1996, *6*, 213.

(42)   Freyhardt, C. C.; Tsapatsis, M.; Lobo, R. F.; Balkus, K. J.; Davis, M. E. *Nature* 1996, *381*, 295.

(43)   Lawton, S. L.; Rohrbaugh, W. J. *Science* 1990, *247*, 1319.

(44)   Summerville, D. A.; Cape, T. W.; Johnson, E. D.; Basolo, F. *Inorg. Chem.* 1978, *17*, 3297-3300.

(45)   Miller, J. S.; Vazquez, C.; Jones, N. L.; McLean, R. S.; Epstein, A. J. *J. Mater. Chem.* 1995, *5*, 707-11.

(46)   Gravereau, P.; Garnier, E.; Hardy, A. *Acta Crystallogr. Sect. B* 1979, *35*, 2843.

(47)   Hoskins, B. F.; Robson, R. *J. Am. Chem. Soc.* 1989, *111*, 5962-4.

(48)   Eddaoudi, M.; Li, H.; Yaghi, O. M. *J. Am. Chem. Soc.* 2000, *122*, 1391.

(49)   Li, H.; Eddaoudi, M.; O'Keeffe, M.; Yaghi, M. *Nature* 1999, *402*, 276.

(50)   Eddaoudi, M.; Moler, D. B.; Li, H.; Chen, B.; Reineke, T. M.; O'Keeffe, M.; Yaghi, O. M. *Acc. Chem. Res.* 2001, *34*, 319-330.

(51)   Eddaoudi, M.; Kim, J.; Rosi, N.; Vodak, D.; Wachter, J.; O'Keeffe, M.; Yaghi, O. M. *Science* 2002, *295*, 469.

(52)   Rosi, N. L.; Eddaoudi, M.; Kim, J.; O'Keeffe, M.; Yaghi, O. M. *CrystEngComm* 2002, *4*, 401.

(53)   Liu, Y.; Kravtsov, V. C.; Larsen, R.; Eddaoudi, M. *Chem. Commun.* 2006, 1488.

(54)   Chui, S. S. Y.; Lo, S. M. F.; Charmant, J. P. H.; Orpen, A. G.; Williams, I. D. *Science* 1999, *283*, 1148.

(55)   Ferey, G.; Mellot-Draznieks, C.; Serre, C.; Millange, F.; Dutour, J.; Surble, S.; Margiolaki, I. *Science* 2005, *309*, 2040.

(56)   Serre, C.; Millange, F.; Thouvenot, C.; Nogues, M.; Marsolier, G.; Loueer, D.; Ferey, G. *J. Am. Chem. Soc.* 2002, *124*, 13519-13526.

(57)   Loiseau, T.; Serre, C.; Huguenard, C.; Fink, G.; Taulelle, F.; Henry, M.; Bataille, T.; Ferey, G. *Chem. Eur. J.* 2004, *10*, 1373.

(58)   Serre, C.; Mellot-Draznieks, C.; Surble, S.; Audebrand, N.; Filinchuk, Y.; Ferey, G. *Science* 2007, *315*, 1828-1831.

(59)   Kondo, M.; Okubo, T.; Asami, A.; Noro, S.-I.; Yoshitomi, T.; Kitagawa, S.; Ishii, T.; Matsuzaka, H.; Seki, K. *Angew. Chem., Int. Ed.* 1999, *38*, 140.

(60)   Kitaura, R.; Kitagawa, S.; Kubota, Y.; Kobayashi, T. C.; Kindo, K.; Mita, Y.; Matsuo, A.; Kobayashi, M.; Chang, H.-C.; Ozawa, T. C.; Suzuki, M.; Sakata, M.; Takata, M. *Science* 2002, *298*, 2358.

(61)   Nouar, F.; Eckert, J.; Eubank, J. F.; Forster, P.; Eddaoudi, M. *J. Am. Chem. Soc.* 2009, *131*, 2864.

(62)   Cote, A. P.; Benin, A. I.; Ockwig, N. W.; O'Keeffe, M.; Matzger, A. J.; Yaghi, O. M. *Science* 2005, *310*, 1166.

(63)   El-Kaderi, H. M.; Hunt, J. R.; Mendoza-Cortes, J. L.; Cote, A. P.; Taylor, R. E.; O'Keeffe, M.; Yaghi, O. M. *Science* 2007, *316*, 268.

(64)   Hill, R. J.; Long, D.-L.; Hubberstey, P.; Schröder, M.; Champness, N. R. *J. Solid State Chem.* 2005, *178*, 2414.

(65)   Cahill, C. L.; de Lill, D. T.; Frisch, M. *CrystEngComm* 2007, *9*, 15-26.

(66)   D. Long; A. J. Blake; N. R. Champness; C. Wilson; M. Schröder *Angew. Chem., Int. Ed. Engl.* 2001, *40*, 2443.

(67)   D.-L. Long; R. J. Hill; A. J. Blake; N. R. Champness; P. Hubberstey; .D M. Proserpio; C. Wilson; M. Schröder *Angew. Chem., Int. Ed.* 2004, *43*, 1851.

(68)   Long, D.-L.; Blake, A. J.; Champness, N. R.; Wilson, C.; Schroder, M. *J. Am. Chem. Soc.* 2001, *123*, 3401.

(69)   Li, Z.; Zhu, G.; Guo, X.; Zhao, X.; Jin, Z.; Qiu, S. *Inorg. Chem.* 2007, *46*, 5174.

(70)   P. M. Forster; N. Stock; A. K. Cheetham *Angew. Chem. Int., Ed.* 2005, *44*, 7608.

(71)   Stock, N.; Bein, T. *J. Mater. Chem.* 2005, *15*, 1384.

(72)   Mueller, U.; Schubert, M.; Teich, F.; Puetter, H.; Schierle-Arndt, K.; Pastre, J. *J. Mater. Chem.* 2006, *16*, 626.

(73)   Collins, D. J.; Zhou, H.-C. *J. Mater. Chem.* 2007, *17*, 3154.

(74)   Cheon, Y. E.; Suh, M. P. *Chem. Commun.* 2009, 2296.

(75)   Llewellyn, P. L.; Bourrrelly, S.; Serre, C.; Filinchuk, Y.; Ferey, G. *Angew. Chem., Int. Ed.* 2006, *45*, 7751.

(76)   Lee, J. Y.; Farha, O. K.; Roberts, J.; Scheidt, K. A.; Nguyen, S. B. T.; Hupp, J. T. *Chem. Soc. Rev.* 2009, *38*, 1450.

(77)   Scherb, C.; Schoedel, A.; Bein, T. *Angew. Chem., Int. Ed.* 2008, *47*, 5777.

(78)   Gu, X.; Xue, D.; Ratajczak, H. *J. Mol. Struct.* 2008, *887*, 56.

(79)   Kremer, C.; Torres, J.; Dominguez, S. *J. Mol. Struct.* 2008, *879*, 130.

(80)   Quin, L. D. *A Guide To Organophosphorous Chemistry*; 1st ed.; John Wiley & Sons: New York, 2000.

(81)   Maeda, K.; Mizukami, F. *Catal. Surv. Jpn.* 1999, *3*, 119.

(82)   Le Bideau, J.; Payen, C.; Palvadeau, P.; Bujoli, B. *Inorg. Chem.* 1994, *33*, 4885.

(83)   Shimizu, G. K. H.; Vaidhyanathan, R.; Taylor, J. M. *Chem. Soc. Rev.* 2009, *38*, 1430.

(84)   Maeda, K.; Kiyozumi, Y.; Mizukami, F. *Angew. Chem.* 1994, *106*, 2427.

(85)   Maeda, K.; Akimoto, J.; Kiyozumi, Y.; Mizukami, F. *J. Chem. Soc., Chem. Commun.* 1995, 1033.

(86)   Lohse, D. L.; Sevov, S. C. *Angew. Chem., Int. Ed. Engl.* 1997, *36*, 1619.

(87)   Gao, Q.; Guillou, N.; Nogues, M.; Cheetham, A. K.; Ferey, G. *Chem. Mater.* 1999, *11*, 2937.

(88)   Clearfield, A. *Metal Phosphonate Chemistry*; John Wiley & Sons, Inc: New York, 1998; Vol. 47.

(89)   Wang, Z.; Heising, J. M.; Clearfield, A. *J. Am. Chem. Soc.* 2003, *125*, 10375.

(90)   Dines, M. B.; Cooksey, R. E.; Griffith, P. C.; Lane, R. H. *Inorg. Chem.* 1983, *22*, 1003.

(91)   Rabu, P.; Janvier, P.; Bujoli, B. *J. Mater. Chem.* 1999, *9*, 1323.

(92)   Stock, N.; Bein, T. *J. Solid State Chem.* 2002, *167*, 330.

(93)   Irran, E.; Bein, T.; Stock, N. *J. Solid State Chem.* 2003, *173*, 293.

(94)   Gomez-Alcantara, M. d. M.; Cabeza, A.; Moreno-Real, L.; Aranda, M. A. G.; Clearfield, A. *Microporous Mesoporous Mater.* 2006, *88*, 293.

(95)   Konar, S.; Zon, J.; Prosvirin, A. V.; Dunbar, K. R.; Clearfield, A. *Inorg. Chem.* 2007, *46*, 5229.

(96)   Cabeza, A.; Aranda, M. A. G.; Bruque, S.; Poojary, D. M.; Clearfield, A.; Sanz, J. *Inorg. Chem.* 1998, *37*, 4168.

(97)   Serpaggi, F.; Ferey, G. *J. Mater. Chem.* 1998, *8*, 2749.

(98)   Stock, N.; Guillou, N.; Bein, T.; Ferey, G. *Solid State Sci.* 2003, *5*, 629.

(99)   D. Kong, J. Z., J. McBee, A. Clearfield *Inorg.c Chem.* 2006, *45*, 977.

(100)   Liang, J.; Shimizu, G. K. H. *Inorg. Chem.* 2007, *46*, 10449.

(101)   Taylor, J. M.; Mahmoudkhani, A. H.; Shimizu, G. K. H. *Angew. Chem., Int. Ed.* 2007, *46*, 795.

(102)   Kong, D.; Zon, J.; McBee, J.; Clearfield, A. *Inorg. Chem.* 2006, *45*, 977.

(103)   Cao, D.-K.; Li, Y.-Z.; Song, Y.; Zheng, L.-M. *Inorg. Chem.* 2005, *44*, 3599.

(104)   Cao, D.-K.; Liu, Y.-J.; Song, Y.; Zheng, L.-M. *New. J. Chem.* 2005, *29*, 721.

(105)   Bauer, S.; Bein, T.; Stock, N. *J. Solid State Chem.* 2006, *179*, 145.

(106)   Cao, D.-K.; Xiao, J.; Li, Y.-Z.; Clemente-Juan, J. M.; Coronado, E.; Zheng, L.-M. *Eur. J. Inorg. Chem.* 2006, 1830.

(107)   Bauer, S.; Stock, N. *J. Solid State Chem.* 2007, *180*, 3111.

(108)   Cao, D.-K.; Li, Y.-Z.; Zheng, L.-M. *J. Solid State Chem.* 2006, *179*, 573.

(109)   Sonnauer, A.; Naether, C.; Hoeppe, H. A.; Senker, J.; Stock, N. *Inorg. Chem.* 2007, *46*, 9968.

(110)   Bauer, S.; Marrot, J.; Devic, T.; Ferey, G.; Stock, N. *Inorg. Chem.* 2007, *46*, 9998.

(111)   Groves, J. A.; Wright, P. A.; Lightfoot, P. *Inorg. Chem.* 2005, *44*, 1736.

(112)   Clearfield, A. *Dalton Trans.* 2008, 6089.

(113)   W. F. Maier; K. Stöwe; S. Sieg *Angew. Chem.* 2007, *119*, 6122.

(114)   Mittasch, A.; Frankenburger, W. *J. Chem. Educ.* 1929, *6*, 2097.

(115)   Hanak, J. J. *Appl. Surf. Sci.* 2004, *223*, 1.

(116)   Thomas, R.; Moulijn, J. A.; De Beer, V. H. J.; Medema, J. *J. Mol. Catal.* 1980, *8*, 161.

(117)   Xiang, X. D.; Sun, X.; Briceno, G.; Lou, Y.; Wang, K.-A.; Chang, H.; Wallace-Freedman, W. G.; Chen, S.-W.; Schultz, P. G. *Science* 1995, *268*, 1738.

(118)   Brinz, T.; Schrof, W. http:/www.dechema.com/HTT, 2006.

(119)   Frost&Sullivan Strategic Analysis of the World Combinatorial Chemistry Markets, 2003.

(120)   A. Duncan , I. M. Dahl, A. Karlsson, R. Wendelbo, *Angew. Chem.* 1998, *110*, 629.

(121)   Newsam, J. M.; Bein, T.; Klein, J.; Maier, W. F.; Stichert, W. *Microporous Mesoporous Mater.* 2001, *48*, 355.

(122)   Bauer, S.; Serre, C.; Devic, T.; Horcajada, P.; Marrot, J.; Ferey, G.; Stock, N. *Inorg. Chem.* 2008, *47*, 7568.

(123)   N. Stock; T. Bein *Angew. Chem., Int. Ed.* 2004, *43*, 749.

(124)   Banerjee, R.; Phan, A.; Wang, B.; Knobler, C.; Furukawa, H.; O'Keeffe, M.; Yaghi, O. M. *Science* 2008, *319*, 939.

# 2 Preparative Methods and Characterization Techniques

2.1 High-Throughput Method

"High-throughput methods" and "Combinatorial chemistry" have been widely used in the pharmaceutical industry over the past 15 years. In contrast to conventional syntheses, where different substances are synthesized and characterized one by one, the aim of a high-throughput approach is the parallel synthesis of many substances as well as their efficient characterization. This technology has expanded to materials design problems outside the field of drug research, especially in areas where trial and error approaches have to be used. The chemistry involved in the hydrothermal synthesis of porous materials is extremely complex and many experimental variables control the formation of a specific crystalline phase. Thus, high-throughput methods are especially useful for the design of micro- and mesoporous materials. The methodology developed in our group includes automated dosing of liquids, the subsequent parallel synthesis, isolation and the automatic characterization by X-ray diffraction.[1]

Our group has developed a multiclave system permitting the investigation of up to 24 (or 48) hydrothermal syntheses at one time. The core of each multiclave used in this work is a metal block containing 24 cavities equipped with individual Teflon liners of a total volume of 3 mL (Figure 2.1 − 1a). The reaction mixtures are prepared directly in the Teflon vessels, which are therefore previously transferred to a multistirrer and equipped with a magnetic stirring bar. Dosing of the starting materials proceeds most easily volumetrically from previously prepared standard solutions of the reagents. After homogenization, the metal block containing the individual reaction batches is closed with a Teflon plate and clamped into the stainless steel multiclave, in which each batch

can be closed individually (Figure 2.1 - 1b). Hydrothermal heating of the whole multiclave is performed in a conventional oven. After a successful hydrothermal reaction the products in the form of crystals are precipitated on the bottom of the synthesis solutions (Figure 2.1 -1c). They can be separated from the reaction mixtures with the help of a multi frit. After the filtration the solid products are placed on a filter paper which is clamped between two metal plates with 24 voids at the position of the samples. The same plates can be fixed to the sample holder of a STOE high throughput-powder diffractometer (Figure 2.1-d). In the diffractometer the powder patterns are measured successively, and are subsequently folded, exported into ASCI format, imported and plotted in Origin in one step (Figure 2.1 - d).
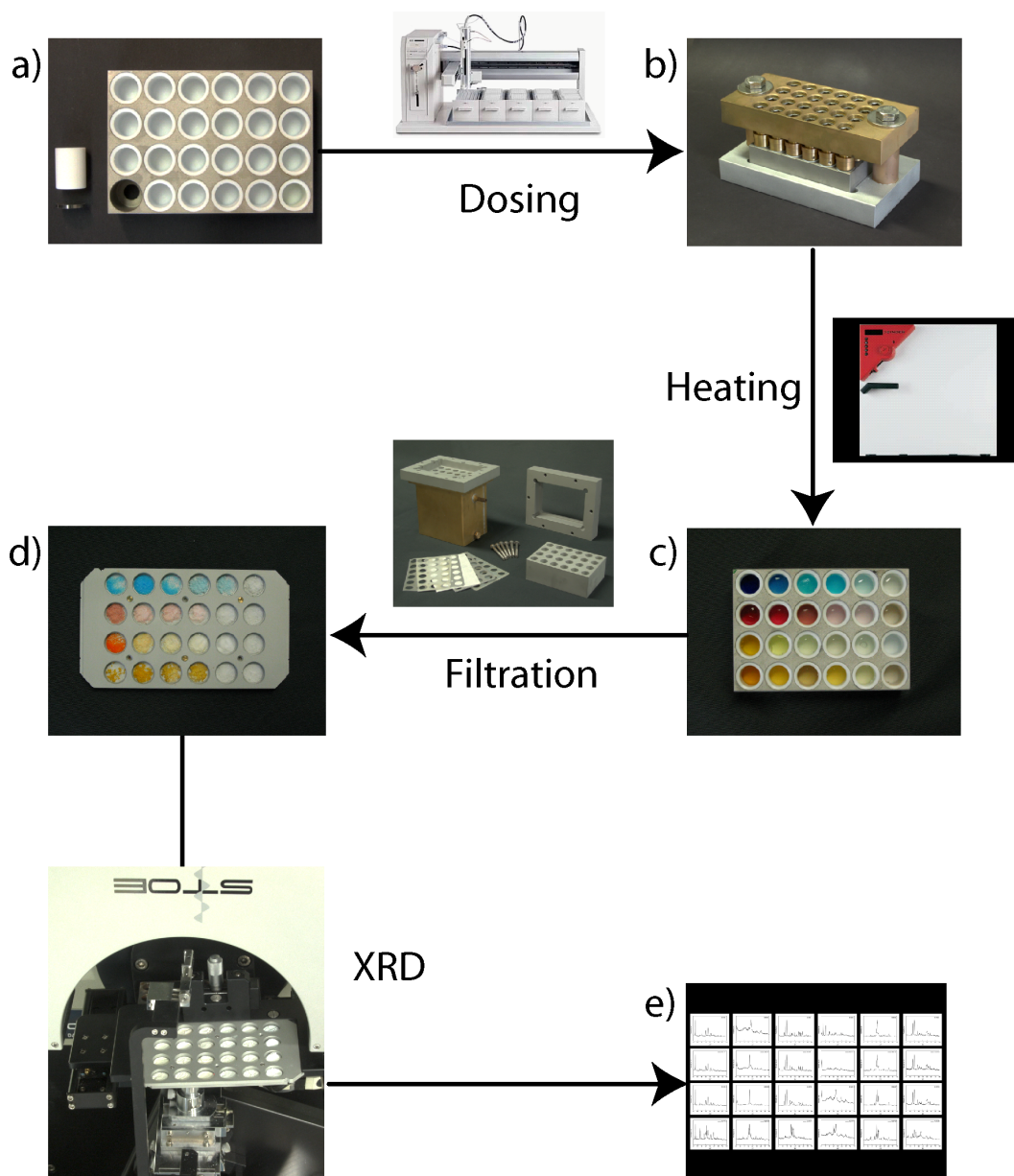
Figure 2.1 - 1: High-throughput workflow for hydrothermal synthesis including dosing and homogenization of the reactants, hydothermal heating, filtration of the solid products, serial characterization by XRD and automated data handling.

2.2 X-Ray Diffractometry

X-Ray diffractometry[2,3] is the most widely used technique for general crystalline materials characterization. Due to the available data base of diffraction patterns of known materials, it is routinely possible to identify known phases in polycrystalline bulk material and to determine their relative amounts from diffraction peak intensities. Beside phase identification XRD is also widely used for strain and particle size determination. Both phenomena can be correlated to the broadening of X-ray signals. However, probably the highest potential of XRD lays in the solution of unknown crystal structures, as XRD patterns provide long-range order information on atomic positions, unit cell dimensions, symmetries and orientation.

2.2.1 Diffraction on a Crystal

In a crystal atoms are located on defined positions of a lattice. Thus, the crystal can be described by planes of atoms that are spaced a distance d apart, but can be resolved into many atomic planes, each with a different d-spacing (Figure 2.2.1 - 1a). To describe the planes a coordinate system for the crystal was introduced, whose unit vectors a, b and c are the edges of the unit cell. Any atomic plane can now be uniquely distinguished by its Miller indices h, k and l. These are the three reciprocal intercepts of the planes with a-, b-, and c-axes and are commonly reduced to the smallest integers having the same ratio. Thus, an (hkl) plane intercepts the crystallographic axes at a/h, b/k and c/l. The d-spacing between (hkl) planes is denoted d_{hkl} and can be related to the axis intercepts by:

$$1/d_{hkl}^2 = h^2/a^2 + k^2/b^2 + l^2/c^2 \qquad (2.2.1 - 1)$$
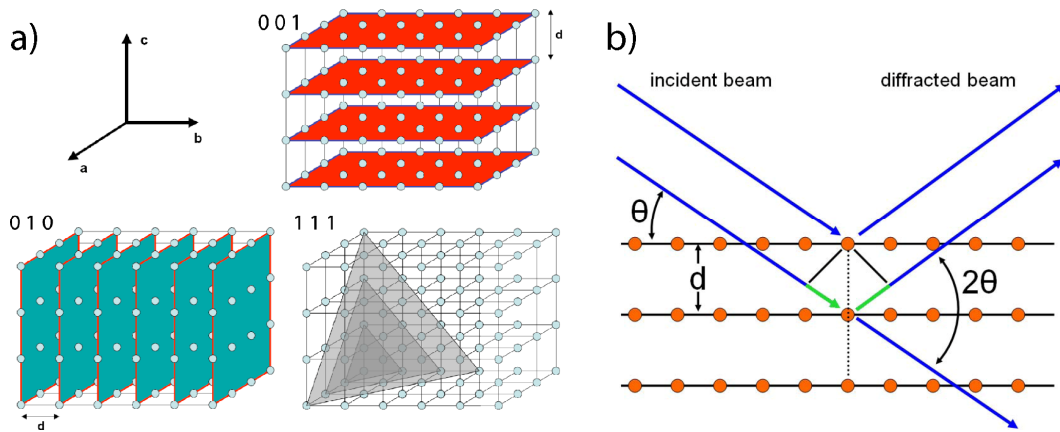
Figure 2.2.1 - 1: a) Several atomic planes and their Miller indices in a cubic crystal. b) Scheme illustrating Bragg's Law: d = distance between two lattice planes; θ diffraction angle.

Solving equation 2.2.1 - 1 in each individual case the crystallographic system, and therefore the respective angles between the a, b and c axis have to be considered. Information about d-values can be obtained from X-ray diffraction experiments. The wavelength of X-rays lies in the Angstrom range, which is the same order of magnitude as the distance between atoms in solid matter. Thus, when X-rays interact with matter, the bonded electrons start to oscillate in the electro-magnetic field generated by the radiation. They become emitters of radially propagating secondary waves, which are coherent to the incident wave but oscillate with a phase shift of π. As atoms in a crystal are ordered periodically, constructive and destructive interference of the elementary waves generated at each atomic position can be observed. If the angular dependent path difference of the single elementary waves is an even multiple of the wavelength, maxima of diffraction emerge form constructive interference. The conditions for constructive interference in a crystal are given by the Bragg Equation (equation 2.2.1-2):

$$2\, d_{hkl} \sin\theta = n\lambda \qquad\qquad (2.2.1\text{-}2)$$

where d_{hkl} is the spacing between the lattice planes and θ the angle between the atomic planes and the incident beam (Figure 2.2.1 - 1b).

2.2.2 Powder Diffraction

A typical powder diffractometer contains an X-ray source, a sample stage and a detector. In most commercial available X-ray tubes, X-rays are produced bombarding a Cu or Mo target with high-energy electrons. When the electrons are slowed down by interaction with the target, part of their energy is radiated as Bremsstrahlung with a continuous background spectrum. Additionally some narrow lines that are characteristic for the elemental composition of the target material are produced by X-ray fluorescence. These lines are selected for diffraction experiments. For the analysis of materials with large unit cell dimension and thus main signals at low angles Cu Kα radiation (λ= 1.5418 Å) is generally more suitable than Mo (λ= 0.07093 Å) radiation, as a lower wavelength leads to a higher resolution in the low angle region of the pattern. Introducing a monochromator into the characteristic beam, one can generate fairly monochromatic X-ray radiation. This radiation is diffracted on the sample. The diffracted intensity is measured as a function of 2θ, which yields the diffraction pattern. As powder samples contain a large number of randomly oriented crystallites, the resulting diffraction patterns are formed by a set of cones from all planes that satisfy the Bragg conditions. Powder diffraction patterns allow quick identification of crystalline phases by comparison with sample libraries. Additionally it is possible to obtain information of the unit cell dimensions. However, due to the loss of information about crystal orientation a complete structure solution from powder data is not straightforward. In this case single crystal methods are more suitable, whenever a single crystal is available.

2.2.3 Single Crystal Structure Analysis

In single crystal structure analysis[2] a suitable crystal is mounted on a goniometer, which allows rotation of the crystal in the X-ray beam. Whenever the Bragg equation is fulfilled, a signal can be observed that lies on the surface of the Ewald sphere. With the positions of an initially detected set of signals the unit cell can be refined and crystal system and orientation matrix determined. The reflexes can be indexed and possible space groups identified with the help of extinction rules. Then intensity data are collected. After the collection, corrections for instrumental factors, polarization effects, X-ray absorption and potentially crystal decomposition must be applied to the entire data set. The next step is the extraction of information about atom types and positions in the unit cell from the experimental data. The principle of structure solution is based upon the crystal interacting with the X-ray beam as a three-dimensional periodic electron density function ρ_{xyz}. From this point of view, diffraction can be considered as a Fourier transformation, thus as a resolution of the electron density function in single waves F_{hkl}. Knowing all single waves, reverse Fourier Transformation allows recalculating the initial complete ρ_{xyz} function and with it the crystal structure. The basic equation for this Fourier synthesis is:

$$
\begin{aligned}
\rho_{xyz} &= \frac{1}{V}\sum_{hkl} F_{hkl} \cdot e^{-i2\pi(hx+ky+lz)} \\
&= \frac{1}{V}\sum_{hkl} F_{hkl} \cdot \left\{ \cos\left[2\pi\left(hx+ky+lz\right)\right] + i\sin\left[2\pi\left(hx+ky+lz\right)\right]\right\}
\end{aligned}
\tag{2.2.2 - 1}
$$

The solution of equation $(2.2.2 - 1)$ allows the calculation of the electron density for each coordinate x, y, z in the unit cell with the Volume V. For this purpose the amplitude of the waves F_{hkl} and the respective phase information must be known. The amplitudes are provided as intensities by the experimental data but phases are not. They can be obtained by iterative calculations with a preliminary
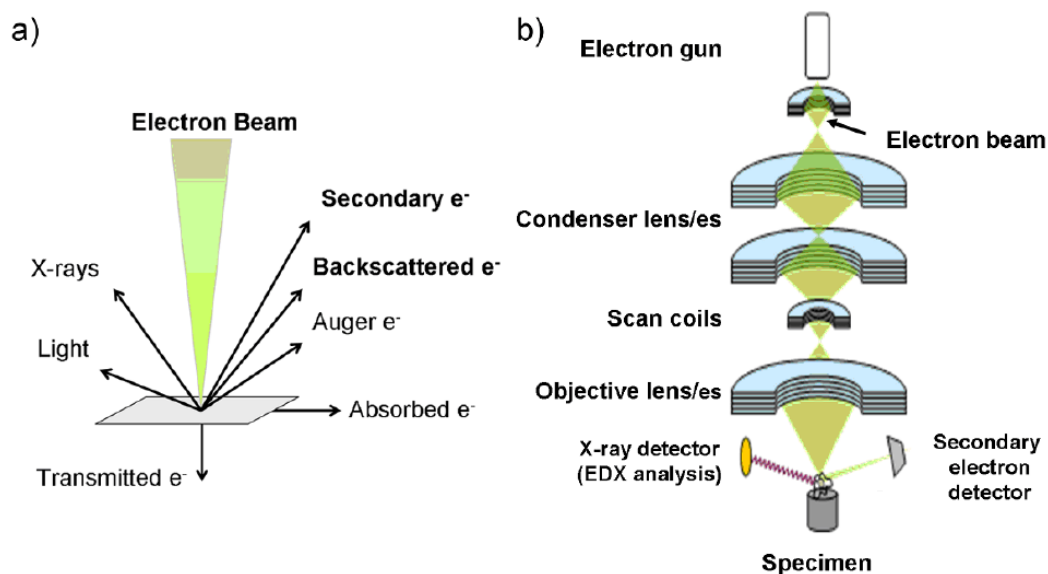
model. This is usually set up with the Patterson Method, relying on having several recognizable heavy atoms in the structure or by an *ab initio* approach using Direct Methods. The newly obtained phases allow the calculation of theoretical structure factors F_c, which contain approximate phase information. These phases are transferred to the experimental F_{hkl}, which allows the calculation of a refined model. The solution of the phase problem finally leads to an initial electron density map. The Fourier Synthesis requires summarizing over all theoretically possible hkl reflexes. However, in a real measurement only a restricted number of reflexes can be detected. This can result false maxima of electron density, due to so called series termination errors. These errors can be reduced by Difference Fourier Synthesis. In this approach, results obtained with theoretically calculated F_c values are subtracted from the equivalent results obtained with experimental F_{hkl} data, so that series termination errors cancel each other. Additionally in this presentation of the electronic map, high electron densities appear only on atom positions that are still missing in the model. This allows completing the model step by step. Once the initial crystal structure is solved, in a successive refinement various parameters such as atomic positions, temperature coefficients and site occupancies can be varied to attain the best possible fit between the observed and calculated crystal structure. The final structure solution will be presented with an R value, which gives the percent variation between the calculated and observed structures.

2.3 Scanning Electron Microscopy and EDX analysis

Offering superior spatial resolution and depth of focus than a conventional light microscope, the scanning electron microscope (SEM) has replaced the optical microscope as a starting tool for materials investigations. The SEM provides topographical information of a sample with a resolution that can approach a few

nm and it can operate at magnifications that are easily adjusted from about 10x-300 000x. In combination with an adequate detector, information about the chemical composition near surface regions of a material can be obtained as well.[4] In an SEM an electron beam is generated under vacuum by accelerating electrons that are emitted from a filament through a high voltage (Figure 2.3 - 1b). The beam is condensed by a set of condenser lenses, directed by scan coils and finally focused through the objective lens on the desired position on the sample. When the incident beam is raster-scanned across the sample, a number of interactions can occur between electron beam and surface. The electron beam penetrating the surface results in the emission of backscattered electrons, secondary electrons, transmitted electrons, Auger electrons, X-rays and photons (Figure 2.3 – 1a). Depending on the desired analysis, the resulting species are detected and evaluated. For SEM imaging, the signal generated by the secondary electrons is amplified and displayed on a screen. The amounts of secondary and backscattered electrons depend on the acceleration voltage of the primary electron beam. However, they are also dependent on the surface morphology and will increase with a decreasing glancing angle of incidence as more scattering occurs closer to the surface. This is the main reason for the excellent topographical contrast in the SE mode: as the surface changes its slope, the number of secondary electrons produced and, thus, the signal intensity changes as well. Scanning electron microscopes are often equipped with an energy dispersive X-ray (EDX) detector that allows elemental analysis of the surface of the samples. X-rays are emitted when outer shell electrons in the sample relax re-occupying the position of inner shell electrons, which were previously ejected by the primary beam. This X-ray radiation is element-specific and can be analyzed to yield qualitative and quantitative information on the sample material.

a)

Electron Beam

X-rays

Light

Secondary e⁻

Backscattered e⁻

Auger e⁻

→ Absorbed e⁻

Transmitted e⁻

b)

Electron gun

Electron beam

Condenser lens/es

Scan coils

Objective lens/es

X-ray detector (EDX analysis)

Secondary electron detector

Specimen

Figure 2.3 ‑ 1: Schematic representation of a Scanning Electron Microscope (SEM). a) Sample electron beam interactions. b) Electron pathway from electron generation to the sample surface.

2.4 Vibrational Spectroscopy

Vibrational spectroscopy[5,6] delivers information about the chemical bonding in a molecule or a material *via* excitation of vibrational modes. For this purpose two physical processes can be used: In IR spectroscopy excitation is achieved by direct coupling between an incident radiation and the electronic structure of the chemical bond. In contrast, in Raman Spectroscopy excitation energy is transferred *via* inelastic scattering of monochromatic light by interaction with the electron clouds surrounding chemical bonds. As both IR and Raman use different physical processes to measure the vibrational spectra, they also display different selection rules for the observable vibrational states and are thus complementary characterization techniques. A general selection rule for photon absorption in IR spectroscopy is the change in the dipole moment of the molecule during vibration. The molecule itself does not need to have a permanent dipole. The general selection rule for Raman scattering is a change

of the polarizability of the bond during vibration. This means that the signal intensity is determined by the degree of deformation of the electron cloud of a chemical bond.

2.4.1 Infrared Spectroscopy

A basic IR experiment can be performed by measuring the intensity of an electromagnetic beam, usually in the IR range from 200 to 4000 cm-1, before and after the interaction with the sample. [5] The sample is irradiated by polychromatic infrared light. To measure the intensity of the absorbed light at each frequency, light is dispersed spatially using a ruled grating or temporally with the help of a Michelson interferometer. If the latter is employed the intensity-time output has to be converted into the familiar intensity-frequency correlation by Fourier transformation. A plot of the resulting difference in intensities versus frequency is the IR spectrum.

2.4.2 Raman Spectroscopy

The main difference of a Raman experiment compared to an IR experiment is the excitation of the sample with monochromatic laser light, usually of a shorter wavelength than infrared.[6] When the intense beam impinges on the sample, it is scattered in all directions. Most scattering is elastic. In this case the re-radiated beam has the same frequency as that of the incident exciting light. This component is known as the Rayleigh scattering and gives a strong central line in the scattering spectrum (Figure 2.4.2 - 1). However a small part of the incident beam is scattered inelastically, exciting or annihilating vibrational modes of the sample. If the excited system was in an energetically low vibrational state, i.e. the ground state, and is excited into higher vibrational states, the energy difference is deducted from the photons of the incident beam. This process is called Stokes scattering. The resulting Raman photons can be observed as weak

side bands in the spectrum at frequencies less than that of the incident beam. Their separation from the Raleigh line is a direct measure of the vibrational frequencies of the sample. The reverse process is called Anti-Stokes Scattering. Thereby existing vibrations that have been excited by thermal processes are annihilated by coupling with the incident beam and add their energy to that of the source. Because anti- Stokes scattering is strongly temperature dependent and weaker, for common Raman measurements only Stokes scattering is used.
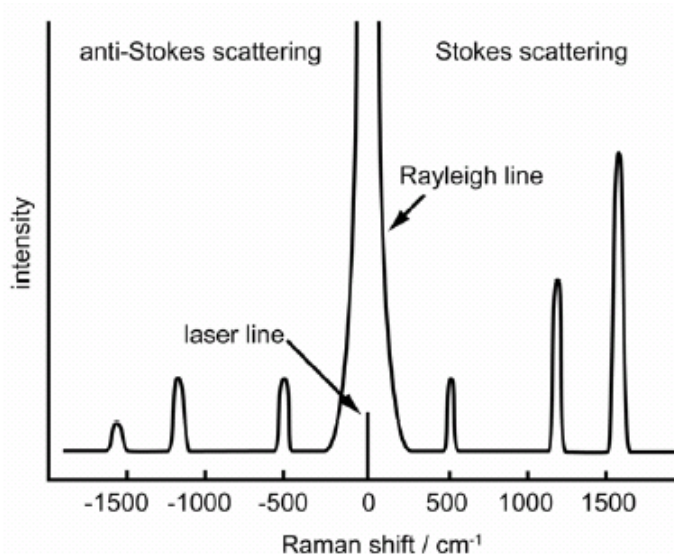
Figure 2.4.2 - 1: Schematic Raman scattering spectrum showing Rayleigh line, Stokes Raman scattering and anti-Stokes Raman scattering

2.5 NMR Spectroscopy

Nuclear magnetic resonance spectroscopy is one of the principal techniques used to obtain physical, chemical, electronic and structural information about molecules.[7] The principle of NMR spectroscopy is based upon the magnetism of certain nuclear isotopes. Nuclei with odd mass, odd atomic number or both have an intrinsic permanent magnetic moment, which can be detected by applying an external magnetic field. Quantum mechanics states that the

magnetic moments adopt only certain discrete orientations relative to the direction of this field. The number of such discrete orientations is 2I+l, where the nuclear spin quantum number I is a half integral or integral constant. In the case I=1/2 two distinct states result with quantized components of the nuclear spin parallel and antiparallel to the direction of the external field. Thereby the parallel orientation is energetically more favourable than the antiparallel one, which leads to an unequal population of both states. In NMR spectroscopy, the energy differences of such two states are measured. For this purpose electromagnetic waves in the radiofrequency region (1-600 MHz) are applied, and the frequency at which the transition occurs between the states is measured. For this to occur the resonance conditions must be fulfilled (equation 2.5-1):

$$\omega = \gamma \, B_{loc} - \gamma \, (B_o + B_{int}) \qquad\qquad (2.5\text{-}1)$$

ω : frequency of the electromagnetic radiation at resonance condition

γ : gyromagnetic ratio

B_{loc} : magnetic field strength at the nuclei

B_0 : externally applied magnetic field

B_{int} : internal field arising from electronic environment and surrounding moments

The measured difference betwen the local magnetic field strength and the applied external field contains information about the electronic and chemical environment of the nuclei.

2.6 Inductive Coupled Plasma - Optical Emission Spectroscopy (ICP-OES)

One of the most important methods for multi-element analysis is optical emission spectroscopy after excitation of the sample by an inductive coupled plasma.[8] With this method the concentration of the element in the sample is determined comparing the intensity of its radiation with an internal standard. The plasma, usually argon, is generated in a high frequency field, where it reaches temperatures of up to 8000°C. At these temperatures ionization of most gas molecules occurs and an external voltage accelerates the free electrons in the plasma. The element-specific radiation is generated by bombardment of the atoms with ions. Radiation of various elements can be detected at the same time. Most commercial spectrometers detect emitted radiation in the range of visible light (200-400 nm). For this reason elements such as halides, nitrogen or oxygen with emit at higher energies (170-200 nm) can't be analyzed. This method can reach a detection limit of down to 0.1 ppb. Limits for detection are defined by the background noise due to radiation emitted during recombination processes of ions with electrons. Samples must be provided in a form that allows easy evaporation, e.g., in solution.

2.7 Thermogravimetric Analysis and Differential Scanning Calorimetry (DSC)

In a typical thermogravimetric analysis (TGA) the change in weight of a sample is detected while the sample is heated on a predefined continuous ramp. The heating can be performed under gas flow of a reactive or inert atmosphere depending on the desired information. For example, combustion via an oxidative process can be controlled or prevent by choosing artificial air or nitrogen as flow gas.

As a complementary technique, Differential Scanning Calorimetry (DSC) can be performed parallel to TGA by measuring the heat needed to hold the sample on the same temperature as an inert reference. DSC delivers information about the exothermic or endothermic character of processes occurring in the sample during heating. Information obtained from TGA and DSC often allows correlating discrete steps of mass loss at specific temperatures with combustion steps, phase transitions or the evaporation of absorbed molecules.

2.8 Sorption

A frequently used method for the determination of porosity, surface area or pore diameter of an open framework is the adsorption of gases. [9,10] It can be measured either with gravimetric or volumetric methods. Depending on the strength of the interactions between the adsorbate and the adsorptive, chemisorption and physisorption can be distinguished. Chemisorption involves the formation of chemical bonds between the gas molecule and the surface, whereas physisorption is mediated by loose interactions, like van-der-Waals forces. In contrast to chemisorption, physisorption is always a reversible process. In this case, the measured adsorbed volume plotted as a function of the relative pressure p/p_0 results in equilibrium isotherms. Such volumetric isotherms are obtained by dosing a certain gas volume into the sample chamber, and by measuring the pressure decrease due to adsorption in the pores. Depending on the types of pores present in the material, the measuring temperature and the probe molecule, different types of isotherms are obtained. According to IUPAC they can be classified into six different types (Figure 2.8 - 1). Microporous materials commonly show isotherms of type I. They are characterized by a steep increase of adsorbed volume at very low relative pressures (typically below 0.1), corresponding to the complete filling of the

pores, as the dimensions of the pores are in the range of the adsorbed gas molecules. No significant further increase of adsorbed volume is observed until a high pressure close to $p/p_0 = 1$ is reached. If the adsorbent particles have nano-scale dimensions, the interparticle voids can be in the mesoporous range leading to textural porosity. Then, a steady increase in adsorbed volume can be observed after complete micropore filling.

Mesoporous materials show type IV isotherms. Characteristic is the formation of adsorbate multilayers in the range of $p/p_0 = 0.05 - 0.25$. Above this pressure, condensation of the gas in the mesopores takes place leading to a step in the adsorbed volume. As the processes of mesopore filling and desorption are different, often a hysteresis loop between the adsorption and desorption curve of the isotherm can be observed.

If the real conditions in a material are close to the conditions described in theoretical models, they can be used to obtain quantitative data about surface area, pore size, diameter and distribution. Traditional models use the interpretation of the isotherm after Langmuir or Brunauer-Emmett–Teller[11] (BET). More precise results are obtained nowadays with models deriving from density functional theory (DFT), which are provided for hydrophobic carbon materials or hydrophilic materials of Si-O in interaction with various non-polar gases such as nitrogen, argon or krypton. However, in the case of flexible metal organic framework materials, these models fail. In this case only qualitative information can be obtained from sorption isotherms.
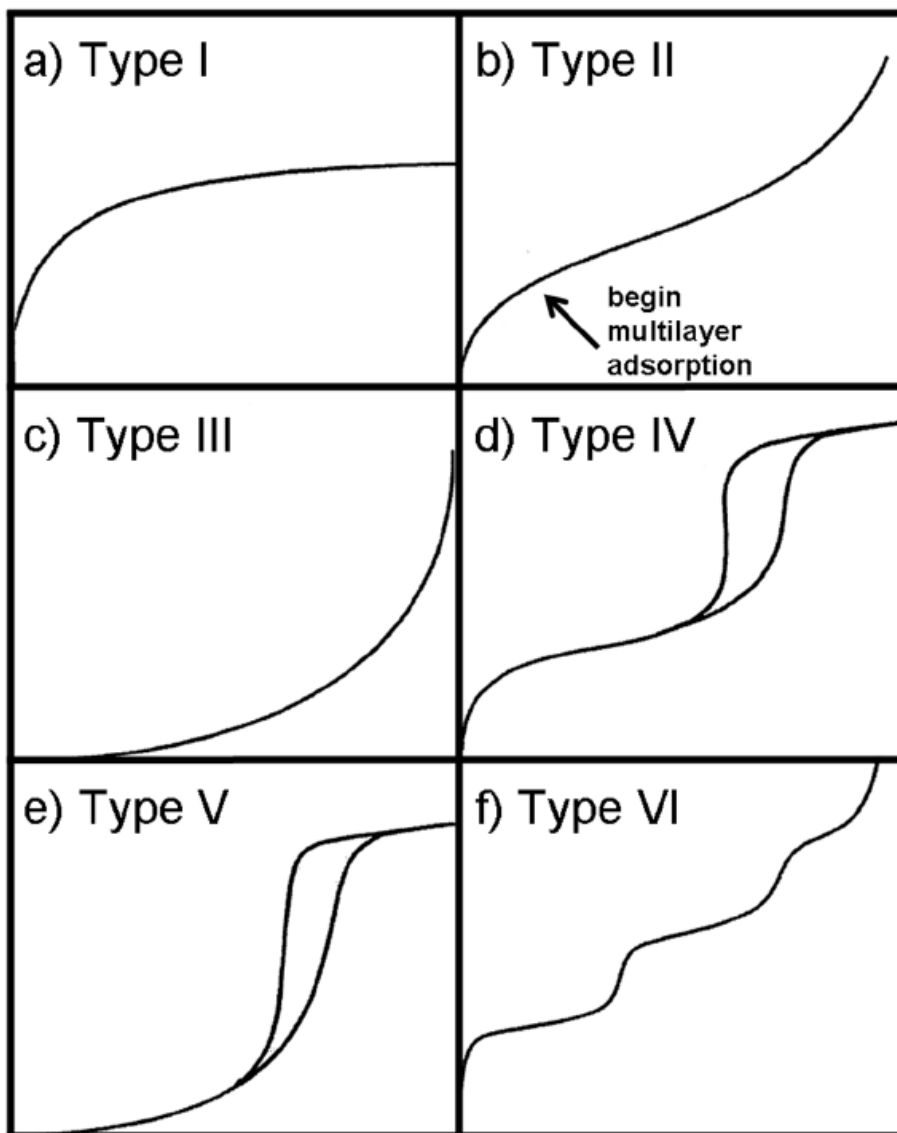
Figure 2.8 - 1: IUPAC classification of isotherms. a) Microporous materials. b) Non-porous material with a high energy of adsorption. c) Non-porous material with a low energy of adsorption. d) Mesoporous materials. The hysteresis loop is associated with the occurrence of pore condensation. e) Mesoporous material with low energy of adsorption. f) Stepwise multilayer adsorption on a uniform non-porous surface.

2.9 References

(1)   Stock, N.; Bein, T. *Angew. Chem., Int. Ed.* 2004, 43, 749.

(2)   Massa, W. *Kristallstrukturbestimmung*; Teubner, 1996.

(3)   Toney, M. F. In Encyclopedia of Materials Characterization - Surfaces, Interfaces, Thin Films; Manning Publications: Greenwich, 1992.

(4)   Roy, H. G. In Encyclopedia of Materials Characterization - Surfaces, Interfaces, Thin Films; Manning Publications: Greenwich, 1992.

(5)   J.N.Cox In Encyclopedia of Materials Characterization - Surfaces, Interfaces, Thin Films; Manning Publications: Greenwich, 1992.

(6)   White, W. B. In Encyclopedia of Materials Characterization - Surfaces, Interfaces, Thin Films;Manning Publications; Greenwich, 1992.

(7)   Friebolin, H. Ein- und zweidimensional NMR Spektroskopie; VCH, Weinheim, 1988.

(8)   Olesik, J. W. In Encyclopedia of Materials Characterization - Surfaces, Interfaces, Thin Films; Manning Publications: Greenwich, 1992.

(9)   Yates, D. J. C. In Encyclopedia of Materials Characterization - Surfaces, Interfaces, Thin Films; Manning Publications: Greenwich, 1992.

(10)   Condon, J. B. Surface Area and Porosity Determination by Physisoprtion Measurements and Theory; Elsevier: Amsterdam, 2006.

(11)   Brunauer, S.; Emmett, P. H.; Teller, E. *J. Am. Chem. Soc.* 1938, 60, 309.

3 Synthesis of 1, 4-Phenylenebis(methylidyne) tetrakis(phosphonic acid), (H_8L)

3.1 Introduction

Diphosphonic acids, PO_3H_2-X-PO_3H_2 constitute a versatile class of bifunctional compounds in which each phosphonate group can provide one, two or three oxygen atoms to coordinate metal ions or to be involved into hydrogen bonds. In addition their chemistry can be modulated by variation in length of the chain X and /or by incorporation of additional functional groups. The presented work focuses on one important subclass of this group that contains a P-C-P backbone. These diphosphonic acids with geminal phosphonate groups, commonly named bisphosphonates, have been known since the 19th century. Initially they were used as antiscaling and anticorrosive agents, but also as complexing agents in textile, oil and fertilizer industries.[1] First discovered in 1960 as non-hydrolysable analogues of pyrophosphate,[2] which is a physiological regulator for calcification and bone resorption, bisphosphonates are today in clinical use and development.[3] Much of the importance of bisphosphonates in bone disorder treatments derives from the ability of gem-bisphosphonate groups to chelate Mg^{2+} and Ca^{2+}. The affinity to Ca^{2+} is required for drug targeting to bone mineral. It was recently found that the activity of bisphosphonates as inhibitors for bone resorption has its origin in the inhibition of an enzyme in the mevalonate pathway, namely the farnesyl pyrophosphate (FPP) synthase.[4,5] As confirmed by X-ray analysis, the binding of the bisphosphonate inhibitor to the active site of this enzyme takes place *via* chelate-complexation of a cluster of three Mg^{2+} ions by the bifunctional ligand.[6] However, despite this excellent performance as chelating agents in biological systems and a notable amount of inorganic coordination compounds[7] that confirm the usefulness of gem-

bisphosphonates as chelating ligands with a variety of metals, this functionality is scarcely used for the synthesis of inorganic-organic hybrid compounds.[8,9] One reason might be the lack of a suitable building block that joins two or more functional groups by a rigid organic linker, similar as they are commonly used for MOF synthesis. In order to fill this gap the present work addresses the synthesis of such a molecule mimicking the overall topology of terephtalic acid, a highly successful building block in MOF synthesis (Scheme 1a).[10] The target compound is 1,4-phenylenebis(methylidyne)tetrakis(phosphonic acid), **H_8L** (Scheme 1b), featuring two bisphosphonate groups as bidentate chelating ligands connected by a rigid benzene unit.

a   **b**
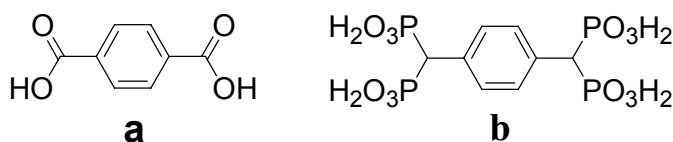
Scheme 1

3.2 Experimental Section

Solvents and chemicals were purchased from Aldrich, Fluka and Merck and were used as received. Organic reactions were carried out under inert gas and glassware was heated before use. Products were dried under high vacuum. Thin-layer chromatography (TLC) and flash column chromatography were performed on silica TLC-plates (Merck, Kieselgel60 F254 Merck) and silica gel 60 (grain size $0.040 - 0.063$ mm), respectively. Elution was performed under pressure. IR spectra were recorded on a Bruker IFS 28 Equinox 55 spectrometer. Liquid samples were measured as films between two KBr plates. Band locations are indicated as wave numbers in cm^{-1}. NMR spectra were recorded at room temperature on a JOEL EX 400 and a JOEL GSX 270. The

chemical shift is given relative to tetramethylsilane (TMS). The solvent signal was used as internal standard. Peaks were assigned with the help of COSY-, HMBC- and HSQC-spectra. Mass spectrometry was carried out on a Finnigan MAT 95Q. Electron bombardment ionization was carried out at a source temperature of 250 °C and with electron energy of 70 eV. For Direct Exposure Probe (DEP) mass spectroscopy samples were heated on a platinum wire from 20 °C to 1600°C with a heating rate of 120°C/min. Elemental analysis was performed on an ELEMENTAR vario EL.

Tetraethyl-[1,4-phenylenbis(methylene)]-bisphosphonate, 1: p-Dibromoxylene (15.40 mmol, 4.07 g) was dissolved in toluene (100 ml) by gentle heating. Then triethyl phosphite was added and the resulting mixture was stirred at 110 °C under a nitrogen flow. The reaction was monitored by TLC. After 20 h the mixture was cooled down to room temperature and the solvent was evaporated *in vacuo*. The resulting solid was purified by flash column chromatography eluting with ethyl acetate / methanol (85:15) to yield 1 (5.41 g, 14.30 mmol, 93 %) as a white solid.

IR (KBr): ν_{max} = 2983, 2952, 2911, 2909, 1514, 1480, 1439, 1430 (sh), 1392, 1367, 1300 (sh), 1242, 1201, 1161, 1140, 1011, 1088, 1033, 961, 864, 833 (sh), 822, 801, 745, 709, 571, 500, 515, 485, 466, 449, 430.

^{31}P-NMR (161.83 MHz, CDCl3): δ = 26.91 ($^2J_{HP}$ = 7.8).

^{1}H-NMR (400 MHz, CDCl$_3$): δ = 1.22, 12H, t, ($^1J_{HH}$ = 7.0), 4 x CH$_2$CH$_3$; 3.11, 4H, d. ($^2J_{HP}$ = 20.2), 2 x CHP; 3.99, 8H, m, 4 x OCH$_2$; 7.23, 4H, s, CH$_{ar.}$

^{13}C-NMR (100.53 MHz, CDCl$_3$): δ = 16.45, 4 x CH$_3$, t, ($^3J_{CP}$ = 3.14), CH$_3$; 33.00, 2 x CH, d, (^1JCP = 139.2), CP; 62.17, 4 x CH$_2$, t, ($^2J_{CP}$ = 3.16), OCH$_2$; 130.00, 4 x CH, C$_{ar}$; 130.33, 2 x C$_q$, C$_{ipso.}$;

HRMS (GC/EI) calcd. for C$_{16}$H$_{28}$O$_6$P$_2$: 378.1361 gmol^{-1} [M$^+$], found: 378.1353.

Octaethyl-[1,4-phenylenebis(methylidyne)tetrakisphosphonate], 2: To a solution of **1** (5 g, 13.2 mmol) in 150 ml of anhydrous THF at −78 °C were added four equivalents of lithium diisopropyl amide (30.1 mL of a 1.8 M solution). After 5 min of stirring diethyl chlorophosphate (4.79 g, 27.78 mmol) was added and the reaction mixture turned green for a moment. The mixture was slowly warmed to room temperature and stirred. After two hours the reaction was quenched by the addition of saturated NH_4Cl solution and the solvent evaporated *in vacuo*. The yellow residue was refluxed in diethyl ether to remove undesired byproducts, then separated from the organic layer by filtration, dissolved in 200 mL of CH_2Cl_2, washed with water and saturated NaCl solution, dried over anhydrous Na_2SO_4, and the solvent evaporated *in vacuo* to yield **2** (3.83 g, 5.9 mmoL, 49 %) as a white powder.

IR (KBr): ν_{max} = 2987, 2932, 2913, 2878, 1511, 1442, 1430 (sh), 1393, 1368, 1304 (sh), 1252, 1239, 1223 (sh), 1179 (sh), 1162, 1098, 1053, 1020, 981 (sh), 965, 949 (sh), 895, 860, 808, 791, 750, 694, 582 (sh), 563, 497, 486, 458, 444(sh), 415.

^{31}P-NMR (161 MHz, $CDCl_3$): δ = 18.81 ($^2J_{HP}$ = 23.5 Hz).

^{1}H-NMR (400 MHz, $CDCl_3$): δ = 1.06, 12H, m, 8 x CH_2CH_3; 1.18, 12H, m, 8 x CH_2CH_3; 3.64, 2H, t, ($^2J_{HP}$ = 24.6), 2 x CHP_2; 3.88, 4H, m, 4 x OCH_AH; 3.98, 4H, m, 4 x OCH_BH; 4.03, 8H, m, 4 x OCH_2; 7.38, 4H, s, $CH_{ar.}$

^{13}C-NMR (100.53 MHz, $CDCl_3$): δ = 16.21, 4 x CH_3, m, CH_2CH_3; 16.32, 4 x CH_3, m, CH_2CH_3; 45.37, 2 x CH, t, ($^1J_{CP}$ = 133.0), CHP_2; 62.92, 4 x CH_2, OCH_2; 63.37, 4 x CH_2, OCH_2; 129.83, 2 x C_q, C_{ipso}; 130.62, 4 x CH; $C_{ar.}$

HRMS (GC/EI) calcd. for $C_{24}H_{46}O_{12}P_4$: 650.1940 [M$^+$], found: 650.1918.

1,4-Phenylenebis(methylidyne)tetrakis(phosphonic acid), H_8L: To a solution of 2 (2.85 g, 4.39 mmol) in 20 ml of dry CH_2Cl_2 was added trimethyl silybromide (5.34 g, 39.50 mmol), and the reaction mixture was stirred under a nitrogen

flow. The reaction was monitored by TLC. After 4 h, the reaction was quenched with 50 ml of MeOH and the solvent evaporated. The residue was recrystallized from diethylether and methanol to obtain **H_8L** as a white powder (4.39 mmol, > 99 %) that reacts acidic in aqueous solution.

IR (KBr): ν_{max} = 2901, 2842, 2278, 1924, 1632, 1506, 1460, 1429, 1306, 1241, 1202, 1156, 1136 (sh), 1031, 1022 (sh), 972 (sh), 962 (sh), 937, 845, 797, 770, 714, 562, 509, 479, 435, 410.

^{31}P-NMR (MHz, D_2O): δ = 17.84 ($^2J_{HP}$ = 24.3 Hz)

^{1}H-NMR (400 MHz, D_2O): δ = 3.78, ^{2}H, t, ($^2J_{HP}$ = 24.39 Hz), CHP_2; 7.24, 4H, s, $CH_{ar.}$

^{13}C-NMR (100.53 MHz, D_2O): 46.67, 2 x CH, t, ($^1J_{CP}$ = 126.10 Hz), CHP_2; 130.60, 4 x CH, C_{ar}; 131.58, 2 x C_q, C_{ipso}.

Anal. calcd for $C_8H_{14}O_{12}P_4 \cdot 1.5\ H_2O$: C, 21.21; H, 3.78; found C, 21.37; H, 3.70.

3.3 Results and Discussion

Mono phosphonic acid esters are usually prepared in conventional Michael-Arbusov reactions. The bisphosphonic acid esters were synthesized introducing a second phosphonate group into the monophosphonic acid ester. First attempts to achieve this via conventional nucelophilic substitution reactions as described by Budnick,[11] Creary[12] and Li[13] failed. The challenge in the case of **H_8L** was to overcome the steric hindrance during the introduction of the second phosphonate group in benzyl position. This was attained following a procedure described by Arstadt[14] that uses the anion-stabilizing effect of the first phosphonate group. Thereby, with the help of a metal organic base, a reactive carbanion is generated in α-position to the electron-withdrawing group that can subsequently attack a phosphorylating agent.
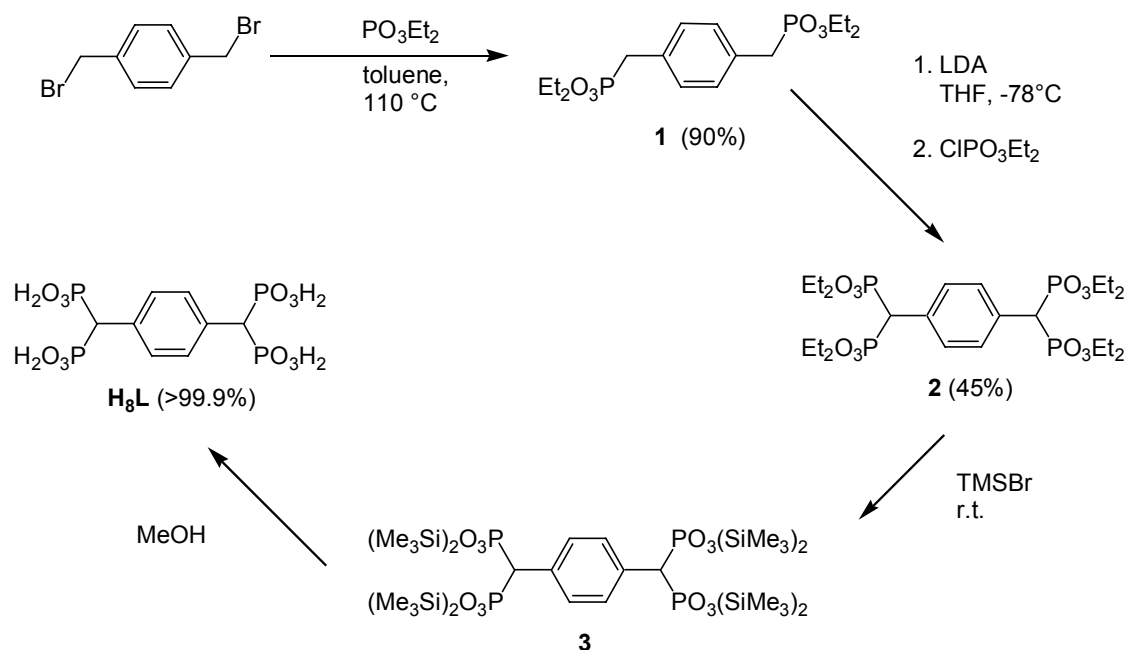
Scheme 2

Thus, **H$_8$L** was prepared in four steps starting from xylylene dibromide (Scheme 2). The monophosphonate groups were introduced via an Arbusov reaction[15]. Treatment of xylylenedibromide with triethyl phosphite under reflux provided tetraethyl-[1,4-phenylenbis(methylen)]-bisphosphonate **1** in 80% yield. The successful C–P bond formation could be confirmed by the observation of a signal at 26.91 ppm in ^{31}P-NMR spectroscopy. The corresponding ^{13}C spectrum showed a doublet signal at 30.00 ppm with a characteristic $^{1}J_{CP}$ - coupling of 139.2 Hz, which could be assigned to the benzylic -CH$_2$- group.

In order to introduce the second phosphonate functionality compound **1** was converted to the corresponding lithium salt using four equivalents of lithium diisopropylamide (LDA). An alternative suitable base resulted to be the lithium salt of 2,2,6,6-tetramethyl piperidine. It was in situ generated from 2,2,6,6-tetramethyl piperidine and n-butyl lithium at − 70 °C. The subsequent reaction

of the lithiated diphosphonate ethylester **1** with diethyl chlorophosphate gave octaethyl-[1,4-phenylenebis(methylidyne)tetrakisphosphonate **2** with a yield of 49 %.[14] The appearance of a triplet ^{13}C-NMR signal at 45.37 ppm (^{1}J$_{CP}$= 133.0 Hz) demonstrated that the second phosphonate group in benzyl position was introduced successfully.

Finally, hydrolysis of **2** was achieved in excellent overall yield by transesterification to the corresponding tetra(trimethylsilyl)ester **3**, followed by addition of methanol.[16] **H$_8$L** was obtained as a white powder that reacts acidic in water. In the IR spectrum the P-O-C band of the ethyl ester group at 1162 cm^{-1} disappeared. The signals of the ethylester group were absent in the ^{1}H NMR spectrum and the signal in ^{31}P-NMR spectroscopy shifted from 18.81 to 17.84 ppm. After extensive recrystallization the compound was proven to be pure by elemental analysis.

3.4 Conclusion

A synthesis route for the introduction of a second phosphonate group in benzyl position was described. In a first step, the lithium ion of the corresponding monophosphorylated compound is produced, which can be subsequently attacked by a phosphorylating agent. Lithium diisopropylamide (LDA) and the lithium salt of 2,2,6,6,-tetramethyl piperidine were found to be suitable metal organic bases for the deprotonation of the mono phosphorylated ester. On that route the title compound 1,4-phenylenebis(methylidyne)tetrakis (phosphonic acid), (H$_2$O$_3$P)$_2$CH-C$_6$H$_4$-CH(PO$_3$H$_2$)$_2$, (**H$_8$L**), was obtained. **H$_8$L**, a ligand with eight replaceable protons, contains two bisphosphonate units that can perform as large bidentate chelates or, considering the phosphonate groups for themselves, as conventional phosphonate ligands in the complexation of metals. The bisphosphonate groups are connected by benzene as a rigid organic linker. The topology of **H$_8$L** resembles benzene dicarboxylic acid, which is a highly

successful ligand in metal organic framework synthesis and a parent compound for a large family of building blocks. The distinctive feature of **H$_8$L** is the enhanced size of the chelating ligand in combination with the strong aciditiy of the phosphonate groups. This new building block might allow access to MOFs in cases when the carboxylate function is too small and unspecific, as for example for large and hard framework metal ions.

3.5 References

(1)   Blomen, L. J. M. J. *Bisphosphonates on Bones*; Elsevier: Amsterdam, 1995.

(2)   Fleisch, H.; Russell, R. G. G.; Straumann, F. *Nature* 1966, *212*, 901.

(3)   Rodan, G. A.; Martin, T. J. *Science* 2000, 289, 1508-14.

(4)   Thompson, K.; Dunford, J. E.; Ebetino, F. H.; Rogers, M. J. *Biochem. Biophys. Res. Commun.* 2002, *290*, 869.

(5)   Russell, R. G. G.; Rogers, M. J. *Bone* 1999, *25*, 97.

(6)   Hosfield, D. J.; Zhang, Y.; Dougan, D. R.; Broun, A.; Tari, L. W.; Swanson, R. V.; Finn, J. *J. Biol. Chem.* 2004, *279*, 8526.

(7)   Matczak-Jon, E.; Videnova-Adrabinska, V. *Coord. Chem. Rev.* 2005, *249*, 2458.

(8)   Bonavia, G.; Haushalter, R. C.; O'Connor, C. J.; Zubieta, J. *Inorg. Chem.* 1996, *35*, 5603.

(9)   Riou-Cavellec, M.; Serre, C.; Robino, J.; Noguès, M.; Grenèche, J. M.; Férey, G. *J. Solid State Chem.* 1999, *147*, 122.

(10)   Eddaoudi, M.; Moler, D. B.; Li, H.; Chen, B.; Reineke, T. M.; O'Keeffe, M.; Yaghi, O. M. *Acc. Chem. Res.* 2001, *34*, 319.

(11)   Budnick, E. G.; US 3,471,406, 1975.

(12)   Creary, X.; Geiger, C. C.; Hilton, K. *J. Am. Chem. Soc.* 1983, *105*, 2851.

(13)   Li, C.; Yuan, C. *Tetrahedron Lett.* 1993, *34*, 1515.

(14)   Arstad, E.; Hoff, P.; Skattebol, L.; Skretting, A.; Breistol, K. *J. Med. Chem.* 2003, *46*, 3021.

(15)   Quin, L. D. *A Guide To Organophosphorous Chemistry*; 1st ed.; John Wiley & Sons: New York, 2000.

(16)   McKenna, C. E.; Higa, M. T.; Cheung, N. H.; McKenna, M. C. *Tetrahedron Lett.* 1977, 155.

4 1, 4-Phenylenebis(methylidyne)tetrakis (phosphonic acid) − A New Building Block in Metal Organic Framework Synthesis

4.1 Introduction

Metal Organic Frameworks (MOFs) have raised considerable interest in both academia and industry due to their fascinating structural chemistry and their potential applications in the field of gas separation and storage, as well as catalysis and chemical sensing. They are composed of organic linkers and metal complexes or clusters, both units acting as building blocks that are often intended to assemble into a three-dimensional open framework. The majority of MOF structures rely on carboxylate derivatives as bidentate ligands having a regular coordination mode with d-block metal ions.[64,145] Conceptually this leads to the secondary building unit (SBU) approach.[60,146] In contrast, in organometalphosphonate chemistry control over the formation of geometrically well-defined structures has not been obtained yet due to the highly variable coordination modes of the phosphonate group. It can act as mono- or bidentate ligand for one, or in combination for various metal centers. In most cases this flexibility allows the metal phosphonate groups to pack efficiently in inorganic layers. This explains the propensity of phosphonate ligands towards layered or pillared solids.[96,99-106] With pillared solids for the first time phosphonates with significant porosity were obtained.[97,120] Unfortunately these materials are low crystalline and therefore hard to define. Only few crystalline three-dimensional coordination polymers with open frameworks are described up to now. [107,108] Nowadays, when searching for three-dimensional inorganic-organic hybrid networks, the phosphonate functionality is often used in combination with other

functional groups such as carboxylates, sulfonates or pyridinium groups.[103,112-119] Similar to the challenges found in phosphonate structural chemistry, a lack of control is often observed in synthesis approaches using lanthanides as metal centers for coordination polymers.[147] Their fluorescence[148-156] and magnetic[149,157] properties make lanthanides highly attractive for the synthesis of functional materials. However, in the absence of design strategies it is difficult to target materials with specific structures and hence properties. With their high and flexible coordination numbers lanthanides extend the number of coordination geometries covered by transition metals, which are typically used in MOF synthesis. On the other hand, due to the high coordination numbers, lanthanide coordination geometries are difficult to control with common small MOF ligands such as carboxylates [80,158-161] or even monophosphonates.[162]

In order to address these issues, we have explored the potential of the new ligand 1,4-phenylenbis(methylidyne)tetrakis (phosphonic acid), **H_8L**, as a new building block in the phosphonate family (Scheme 4.1. - 1). Featuring two bisphosphonate groups as bidentate chelating ligands, **H_8L** is able to complex large ions with high coordination numbers, such as lanthanides, with a well-defined geometry that is common for carboxylate ligands and small ions such as zinc or copper.[163] Using a synthetic high-throughput approach, **H_8L** was screened in combination with different lanthanides and under different synthesis conditions. For this purpose we have developed a multiclave system permitting the investigation of up to 24 hydrothermal syntheses at once. The methodology includes automated dosing of liquids, subsequent parallel synthesis, isolation and the automatic characterization by X-ray diffraction.[121]

$$H_2O_3P \quad \overbrace{\qquad} \quad PO_3H_2$$
$$H_2O_3P \quad \underbrace{\qquad} \quad PO_3H_2$$

H_8L
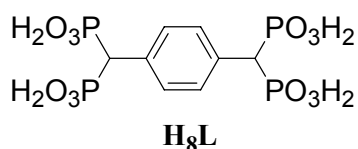
Scheme 4.1 - 1

4.2 Experimental Section

Solvents and chemicals were purchased from Aldrich, Fluka and Merck and were used as received. Bi-distilled water was used from a Millipore system (Milli-Q Academic A10). 1,4-Phenylenebis(methylidyne)tetrakis(phosphonic acid), **H$_8$L** was prepared as described in chapter 1. In order to facilitate the dosing, solutions were prepared from all reagents. In a volumetric flask 25 mL of a 0.5 M solution of **H$_8$L** were prepared by dissolving 5.663 g of the ligand in deionized water. 1 M solutions of lanthanide salts were prepared of La(NO$_3$)$_3$·6 H$_2$O, Nd(NO$_3$)$_3$·6 H$_2$O, Gd(NO$_3$)$_3$·6 H$_2$O and Dy(NO$_3$)$_3$·6 H$_2$O in deionized water. A 1 M NaOH standard solution was purchased.

High-throughput screening experiments with **H$_8$L** were performed in custom-made multiclaves with 24 cavities containing individual Teflon liners of an individual total volume of 3 mL. Before each synthesis the liners were cleaned in concentrated HCl and rinsed with water. Then they were deposited on a multistirrer device and equipped with small magnetic stirring bars. Reaction gels were prepared according to the following general procedure: The ligand solution was filled into the Teflon liner, deionized water was added and stirring was started. If applicable, NaOH was added. After subsequent addition of the metal-salt solution, a precipitation occurred. The reaction mixture was stirred for 30 minutes until a homogenous gel was formed. After the removal of the stirring bars the pH was measured and the Teflon liners were transferred to the reactor block, closed and mounted into the multiclave. Subsequently they were heated for 7 days at 75 °C, 100 °C, 150 °C or 180 °C, respectively. After the heating procedure the pH was measured again and crystals were separated from the reaction mixture by filtration under reduced pressure with the help of a custom-made multi-frit and washed with water. Products were dried at room

temperature and XRDs were recorded. The discovery library was prepared from reactions with the following batch compositions:

x La(NO$_3$)$_3$: H_8L :y NaOH: 830 H_2O x = 1, 2, 4 and 6

x Nd(NO$_3$)$_3$: H_8L :y NaOH: 830 H_2O y = 0, 4 and 8

x Dy(NO$_3$)$_3$: H_8L :y NaOH: 830 H_2O

x Gd(NO$_3$)$_3$: H_8L :y NaOH: 830 H_2O
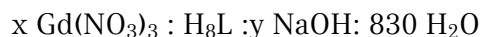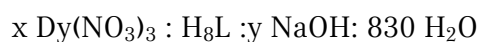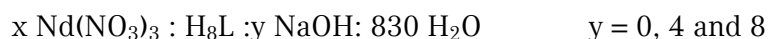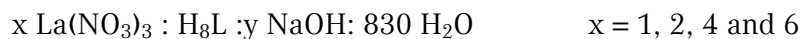
A typical batch volume was 1.5 mL. In order to obtain crystals suitable for single crystal structure analysis, dilution series of all new compounds were generated at the conditions that provided best crystallinity according to XRD, or that showed large crystals in the optical microscope, respectively. For this purpose, the synthesis time, temperature and composition of the respective batches were maintained, except for the water content z:

x La(NO$_3$)$_3$: H_8L :y NaOH: z H_2O z = 830, 1660, 2075, 8300, 16600, 83000
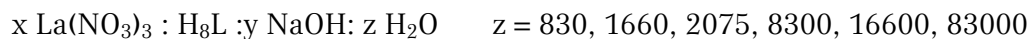
The highest dilution degree at z = 83000 corresponds, in a typical batch with 1.5 mL volume, to a total amount of reactants of about 1 mg. This was the lowest amount that could be accurately dosed. The best crystallization conditions for each new phase and the conditions that allowed the growth of single crystals are listed in Table 4.2 - 1. A detailed description of the respective syntheses including the information about yield, EDX characterization and elemental analysis are given below:

Table 4.2 - 1: Optimal synthesis conditions for the new lanthanide-phosphonates and single crystals if available:

Compound	batch composition	T / °C
La(H$_5$L) a	La(NO$_3$)$_3$: H$_8$L : 830 H$_2$O	150
La(H$_5$L) c	La(NO$_3$)$_3$: H$_8$L : 830 H$_2$O	180
NaLa(H$_4$L)	La(NO$_3$)$_3$: H$_8$L : 4 NaOH: 830 H$_2$O	100
NaLa(H$_4$L), singl. crystal	La(NO$_3$)$_3$: H$_8$L : 4H$_2$O : 8300 H$_2$O	100
La$_2$(H$_2$L)	4 La(NO$_3$)$_3$: H$_8$L : 4 NaOH: 830 H$_2$O	100
La$_2$(H$_2$L), singl. crystal	6 La(NO$_3$)$_3$: H$_8$L : 830 H$_2$O	100
La(H$_5$L) b, singl. crystal	La(NO$_3$)$_3$: H$_8$L : 8300 H$_2$O	150
Nd(H$_5$L) d	Nd(NO$_3$)$_3$: H$_8$L: 830 H$_2$O	150
NaNd(H$_4$L)	Nd(NO$_3$)$_3$: H$_8$L : 4 NaOH : 830 H$_2$O	150
Nd$_2$(H$_2$L)	6 Nd(NO$_3$)$_3$: H$_8$L : 830 H$_2$O	100
Nd(H$_5$L) b	Nd(NO$_3$)$_3$: H$_8$L: 830 H$_2$O	180
Nd(H$_5$L) a, singl. crystal	Nd(NO$_3$)$_3$: H$_8$L : 4 NH$_3$: 16660 H$_2$O	150
Gd(H$_5$L) d	Gd(NO$_3$)$_3$: H$_8$L: 830 H$_2$O	75
NaGd(H$_4$L)	Gd(NO$_3$)$_3$: H$_8$L : 4 NaOH : 830 H$_2$O	100
Gd$_2$(H$_2$L)	2 Gd(NO$_3$)$_3$: H$_8$L : 4 NaOH : 830 H$_2$O	100
Dy(H$_5$)L e	Dy(NO$_3$)$_3$: H$_8$L: 830 H$_2$O	100
NaDy(H$_4$L)	Dy(NO$_3$)$_3$: H$_8$L : 4 NaOH : 830 H$_2$O	150
Dy$_2$(H$_2$L)	6 Dy(NO$_3$)$_3$: H$_8$L : 4 NaOH : 830 H$_2$O	75

La(H$_5$L) a: To 0.40 mL of a 0.5M aqueous solution of **H$_8$L**, 2.40 mL of deionized water was added. Stirring was started and 0.2 mL of a 1M solution of La(NO$_3$)$_3$ in deionized water was added. The gel with the batch composition La(NO$_3$)$_3$: H$_8$L: 830 H$_2$O was stirred for 30 minutes and then heated under hydrothermal conditions for one week at 150°C. The precipitated crystals were separated from the reaction mixture by filtration under reduced pressure, washed with deionized water and dried at room temperature. The pH of the reaction mixture was 1.0 before and after the heating process. (Yield: 79.0 mg, 0.125 mmol, 63 %). **EDX**: La: P atomic ratio = 0.9 : 4.0. **Anal. Calcd** for C$_8$H$_{19}$LaO$_{16}$P$_4$: C, 15,15; H, 3,02; La, 21.91; P, 19,54 found: C15,35; H,2.86; La, 22.11; P, 19.28.

La(H_5L) c: To 0.20 mL of a 0.5 M aqueous solution of **H_8L**, 1.20 mL of deionized water was added. Stirring was started and 0.1 mL of a 1 M solution of La(NO_3)$_3$ in deionized water was added. The gel with the batch composition La(NO_3)$_3$: H_8L: 830 H_2O was stirred for 30 minutes and then heated under hydrothermal conditions for one week at 180 °C. The precipitated crystals were separated from the reaction mixture by filtration under reduced pressure, washed with deionized water and dried at room temperature. The pH of the reaction mixture was 1.0 before and after the heating process. (Yield: 70 mg). **EDX**: La : P atomic ratio = 0.9 : 4.0.

NaLa(H_4L)*:* To 2.00 mL of a 0.5M aqueous solution of H_8L, 7.94 mL (830 mmol) of deionized water and 4.00 mL of 1m NaOH solution was added. Stirring was started and 1 mL of a 1M solution of La(NO_3)$_3$ in deionized water was added. The gel with the batch composition La(NO_3)$_3$: H_8L : 4 NaOH : 830 H_2O was stirred for 30 minutes and then heated under hydrothermal conditions for 24 h at 100°C. The precipitated crystals were separated from the reaction mixture by filtration under reduced pressure, washed with deionized water and dried at room temperature. The pH of the reaction mixture was 1.0 before and 1.5 after the heating process. (Yield: 630 mg, 0.96 mmol, 96 %). **EDX**: La : Na : P atomic ratio = 1.1 : 1.3 : 4.0. **Anal. Calcd** for $C_8H_{18}LaNaO_{16}P_4$: C, 14.65; H, 2.77; La, 21.17; Na, 3.50; P, 18.89 found: C, 14.70; H, 2.75; La, 21.95; Na, 3.53; P, 18.23. Single crystals were obtained with the same procedure and a batch composition of La(NO_3)$_3$: H_8L: 4 NaOH : 8300 H_2O.

La$_2$(H_2L): To 0.2 mL of a 0.5M aqueous solution of **H_8L** 0.5 mL of deionized water and 0.4 mL of a 1 m NaOH solution was added. Stirring was started and 0.4 mL of a 1M solution of La(NO_3)$_3$ in deionized water was added. The gel with the batch composition 4 La(NO_3)$_3$: H_8L : 4 NaOH : 830 H_2O was stirred for 30 minutes and then heated under hydrothermal conditions for 1 week at 100 °C. The precipitated crystals were separated from the reaction mixture by filtration

under reduced pressure, washed with deionized water and dried at room temperature. The pH of the reaction mixture was 1.0 before and after the heating process. Yield: 80 mg, 0.095 mmol (95%). **EDX**: La : P atomic ratio = 1 : 2. **Anal. Calcd** for C$_8$H$_{24}$La$_2$O$_{20}$P$_4$: C, 11.41; H, 2.87; La, 33.00; O, 38.00; P, 14.71 found: C, 11.52; H, 2.91; La, 31.12; P, 14.56.

La(H$_5$L) b: Single crystals were obtained adding 1.470 mL of deionized water to 0.02 mL of a 0.5M aqueous solution of **H$_8$L**. Stirring was started and 0.01 mL of a 1M solution of La(NO$_3$)$_3$ in deionized water was added. The mixture with the batch composition La(NO$_3$)$_3$: H$_8$L : 8300 H$_2$O was stirred for 30 minutes and then heated for one week under hydrothermal conditions at 150°C. The precipitated crystals were separated from the reaction mixture by filtration under reduced pressure, washed with deionized water and dried at room temperature. The pH of the reaction mixture was 2.0 before and after the heating process.

Nd(H$_5$L) d: To 0.20 mL of a 0.5M aqueous solution of **H$_8$L**, 1.20 mL of deionized water was added. Stirring was started and 0.1 mL of a 1M solution of Nd(NO$_3$)$_3$ in deionized water was added. The gel with the batch composition Nd(NO$_3$)$_3$: H$_8$L: 830 H$_2$O was stirred for 30 minutes and then heated under hydrothermal conditions for one week at 150°C. The precipitated crystals were separated from the reaction mixture by filtration under reduced pressure, washed with deionized water and dried at room temperature. The pH of the reaction mixture was 1.0 before and after the heating process. (Yield: 61.0 mg). **EDX:** Nd: P atomic ratio = 0.8 : 4.0.

NaNd(H$_4$L): To 0.20 mL of a 0.5M aqueous solution of **H$_8$L**, 0.8 mL of deionized water and 0.4 mL of 1M NaOH solution was added. Stirring was started and 0.1 mL of a 1M solution of Nd(NO$_3$)$_3$ in deionized water was added. The gel with the batch composition Nd(NO$_3$)$_3$: H$_8$L : 4 NaOH : 830 H$_2$O was stirred for 30 minutes and then heated under hydrothermal conditions for one week at 150°C.

The precipitated crystals were separated from the reaction mixture by filtration under reduced pressure, washed with deionized water and dried at room temperature. The pH of the reaction mixture was 1.0 before and after the heating process. (Yield: 65.0 mg, 0.098 mmol, 98 %). **EDX:** Nd: Na : P atomic ratio = 1.2 : 0.9 : 4.0.

$Nd_2(H_2L)$: To 0.16 mL of a 0.5M aqueous solution of **H_8L** 0.86 mL of deionized water was added. Stirring was started and 0.48 mL of a 1M solution of $Nd(NO_3)_3$ in deionized water was added. The gel with the batch composition 6 $Nd(NO_3)_3$: H_8L : 830 H_2O was stirred for 30 minutes and then heated under hydrothermal conditions for 1 week at 100 °C. The precipitated crystals were separated from the reaction mixture by filtration under reduced pressure, washed with deionized water and dried at room temperature. The pH of the reaction mixture was 1.0 before and after the heating process. Yield: 65.6 mg, 0.077 mmol (96%). **EDX**: Nd : P atomic ratio = 1 : 2.

$Nd(H_5L)$ b: To 0.20 mL of a 0.5M aqueous solution of **H_8L**, 1.20 mL of deionized water was added. Stirring was started and 0.1 mL of a 1M solution of $Nd(NO_3)_3$ in deionized water was added. The gel with the batch composition $Nd(NO_3)_3$: H_8L: 830 H_2O was stirred for 30 minutes and then heated under hydrothermal conditions for one week at 180°C. The precipitated crystals were separated from the reaction mixture by filtration under reduced pressure, washed with deionized water and dried at room temperature. The pH of the reaction mixture was 1.0 before and after the heating process. (Yield: 60.0 mg, 0.093 mmol, 93 %). **EDX**: Nd : P atomic ratio = 0.9 : 4.0. **Anal. Calcd** for $C_8H_{19}NdO_{16}P_4$: C, 15.03; H, 3.00; Nd, 22.56; P, 19.38 found: C, 14.80; H, 2.49; Nd, 25.72; P, 16.50.

$Nd(H_5L)$ a: Single crystals were obtained adding 1.493 mL of deionized water and 0.02 mL of a 1M NH_3 solution to 0.01 mL of a 0.5M aqueous solution of **H_8L**. Stirring was started and 0.005 mL of a 1M solution of $Nd(NO_3)_3$ in deionized water was added. The mixture with the batch composition $Nd(NO_3)_3$:

H$_8$L : 4 NH$_3$: 16660 H$_2$O was stirred for 30 minutes and then heated for ten days under hydrothermal conditions at 150°C. The precipitated crystals were separated from the reaction mixture by filtration under reduced pressure, washed with deionized water and dried at room temperature. The pH of the reaction mixture was 4.0 before and 2.5 after the heating process. **EDX**: Nd: P atomic ratio = 0.8 : 4.0.

Gd(H$_5$L) d: To 0.20 mL of a 0.5M aqueous solution of **H$_8$L**, 1.20 mL of deionized water was added. Stirring was started and 0.1 mL of a 1M solution of Gd(NO$_3$)$_3$ in deionized water was added. The gel with the batch composition Gd(NO$_3$)$_3$: H$_8$L: 830 H$_2$O was stirred for 30 minutes and then heated under hydrothermal conditions for one week at 75°C. The precipitated crystals were separated from the reaction mixture by filtration under reduced pressure, washed with deionized water and dried at room temperature. The pH of the reaction mixture was 1.0 before and after the heating process. (Yield: 55 mg). **EDX**: Gd: P atomic ratio = 0.8: 4.0.

NaGd(H$_4$L): To 0.20 mL of a 0.5M aqueous solution of **H$_8$L**, 0.8 mL of deionized water and 0.4 mL of 1M NaOH solution was added. Stirring was started and 0.1 mL of a 1M solution of Gd(NO$_3$)$_3$ in deionized water was added. The gel with the batch composition Gd(NO$_3$)$_3$: H$_8$L : 4 NaOH : 830 H$_2$O was stirred for 30 minutes and then heated under hydrothermal conditions for one week at 100°C. The precipitated crystals were separated from the reaction mixture by filtration under reduced pressure, washed with deionized water and dried at room temperature. The pH of the reaction mixture was 1.0 before and after the heating process. (Yield: 64.1 mg, 0.095 mmol, 95 %). **EDX**: Gd : Na : P atomic ratio = 0.8 : 1.3 : 4.0.

Gd$_2$(H$_2$L): To 0.2 mL of a 0.5M aqueous solution of **H$_8$L** 0.7 mL of deionized water and 0.4 ml of 1m NaOH solution was added. Stirring was started and 0.2 mL of a 1M solution of Gd(NO$_3$)$_3$ in deionized water was added. The gel with the

batch composition 2 Gd(NO$_3$)$_3$: H$_8$L : 4 NaOH : 830 H$_2$O was stirred for 30 minutes and then heated under hydrothermal conditions for 1 week at 100 °C. The precipitated crystals were separated from the reaction mixture by filtration under reduced pressure, washed with deionized water and dried at room temperature. The pH of the reaction mixture was 1.0 before and after the heating process. Yield: 79 mg, 0.09 mmol (93%). **EDX** : Gd : P atomic ratio = 0.7 : 2.

Dy(H$_5$L) e: To 0.20 mL of a 0.5M aqueous solution of **H$_8$L**, 1.20 mL of deionized water was added. Stirring was started and 0.1 mL of a 1M solution of Dy(NO$_3$)$_3$ in deionized water was added. The gel with the batch composition Dy(NO$_3$)$_3$: H$_8$L: 830 H$_2$O was stirred for 30 minutes and then heated under hydrothermal conditions for one week at 100°C. The precipitated crystals were separated from the reaction mixture by filtration under reduced pressure, washed with deionized water and dried at room temperature. The pH of the reaction mixture was 1.0 before and after the heating process. (Yield: 50.0 mg). **EDX**: Dy: P atomic ratio = 0.8: 4.0.

NaDy(H$_4$L): To 0.20 mL of a 0.5M aqueous solution of **H$_8$L**, 0.8 mL of deionized water and 0.4 mL of 1M NaOH solution was added. Stirring was started and 0.1 mL of a 1M solution of Dy(NO$_3$)$_3$ in deionized water was added. The gel with the batch composition Dy(NO$_3$)$_3$: H$_8$L : 4 NaOH : 830 H$_2$O was stirred for 30 minutes and then heated under hydrothermal conditions for one week at 150°C. The precipitated crystals were separated from the reaction mixture by filtration under reduced pressure, washed with deionized water and dried at room temperature. The pH of the reaction mixture was 1.0 before and after the heating process. (Yield: 65.9 mg, 0.097 mmol, 97 %). **EDX**: Dy : Na : P atomic ratio = 0.8 : 1.3 : 4.0.

Dy$_2$(H$_2$L): To 0.16 mL of a 0.5M aqueous solution of **H$_8$L** 0.54 mL of deionized water and 0.32 ml of 1m NaOH solution was added. Stirring was started and

0.48 mL of a 1M solution of Dy(NO$_3$)$_3$ in deionized water was added. The gel with the batch composition 6 Dy(NO$_3$)$_3$: H$_8$L : 4 NaOH : 830 H$_2$O was stirred for 30 minutes and then heated under hydrothermal conditions for 1 week at 75 °C. The precipitated crystals were separated from the reaction mixture by filtration under reduced pressure, washed with deionized water and dried at room temperature. The pH of the reaction mixture was 1.0 before and after the heating process. Yield: 67.6 mg, 0.076 mmol (95 %). **EDX**: Dy : P atomic ratio = 0.83 : 2.

Characterization: High-throughput X-ray analysis of all samples of the discovery library was carried out using a Stoe high-throughput powder diffractometer equipped with an image plate detector system [121]. Higher resolution X-ray powder diffraction patterns were recorded from all new phases in theta-theta geometry with a Bruker D8 Discover instrument using monochromatic CuK$_\alpha$ radiation and a Vantec detector. Morphology and stoichiometry were studied with a Joel JSM 6500 F scanning electron microscope equipped with an EDX detector. The respective samples were applied to an adhesive carbon film on the sample holder and coated with carbon by a BAL-TEC MED 020 Coating System. Raman spectra were recorded on a Jobin Yvon Horiba HR800 UV Raman microscope using a HeNe laser emitting at 632.8 nm. Thermogravimetric analyses (TGA) were performed on a Netzsch STA 449 C TG/DSC (heating rate of 10 K/min in a stream of synthetic air of ~25 mL/min). The chemical compositions of representatives of each new structure type were determined by inductively coupled plasma optical emission spectroscopy (ICP-OES, VARIAN VISTA) and an ELEMENTAR vario EL.

Crystallography: Cell determination and data collection for single-crystal structure analysis by X-ray diffraction was performed on an Enraf-Nonius Kappa-CCD diffractometer equipped with a rotating anode (MoK$_\alpha$ radiation, λ =

71.073 pm). All single crystal structures were solved by direct methods and refined using the program package SHELXTL[164].

Nd(H$_5$L) a: Structure analysis of the rods revealed the composition Nd[(PO$_3$H)$_2$CH-C$_6$H$_4$-CH(PO$_3$H)(PO$_3$H$_2$)]·4H$_2$O. The structure was solved with direct methods in the triclinic space group P-1. All hydrogen atoms except those from water could be localized in the difference Fourier map. Crystallographic data are listed in Table 8.1.5 - 1[165], selected bond distances in Tables 8.1.5 - 2/3/4.

La(H$_5$L) b: Structure analysis of the colorless rods revealed the composition La[(PO$_3$H)$_2$CH-C$_6$H$_4$-CH(PO$_3$H)(PO$_3$H$_2$)]·4H$_2$O. Structure solution succeeded in the triclinic space group P-1. All hydrogen atoms could be localized in the difference Fourier map. The positions of the hydrogen atoms next to O2 and O12 are only half occupied. Crystallographic data are listed in Table 8.1.5 - 1, selected bond distances are listed in the Tables 8.1.5 - 5/6/7.

La$_2$(H$_2$L): Structure analysis of the colorless blocks revealed the composition La$_2$[(HO$_3$P)(O$_3$P)-CH-C$_6$H$_4$-CH-(PO$_3$)(PO$_3$H)]·8H$_2$O. Structure solution succeeded in the triclinic space group P-1. All hydrogen atoms could be localized in the difference Fourier map. Crystallographic data are listed in Table 8.1.5-1, selected bond distances are listed in the Tables 8.1.5 - 8/9/10.

NaLa(H$_4$L): Structure analysis of the rhombic crystals revealed the composition LaNa[(PO$_3$H)$_2$CH-C$_6$H$_4$-CH(PO$_3$H)$_2$]·4H$_2$O. The structure was solved with direct methods in the monoclinic space group P2$_1$/n. All hydrogen atoms with exception of the water-hydrogen bonded to O15 could be localized in the difference Fourier map. Crystallographic data are listed in Table 8.1.5-1, selected bond distances are listed in Tables 8.1.5 - 11/12/13.

4.3 Results and Discussion

In the high-throughput screening the organic building block **H$_8$L** was reacted with La^{3t}, Nd^{3+}, Dy^{3+} and Gd^{3+} ions under hydrothermal conditions. The metal-to-ligand ratio in the synthesis solutions was selected as 1:1, 2:1, 4:1 and 6:1, considering the possible formation of single-metal nodes and cluster nodes in three-dimensional open frameworks. The pH was adjusted with sodium hydroxide. The NaOH-to-ligand ratio was 0:1, 4:1 and 8:1, thus covering a pH range from pH = 1 to pH = 7-8. No reactions were carried out under alkaline conditions because of the expected precipitation of lanthanide hydroxides in basic media. Crystallization proceeded under hydrothermal conditions for 10 days at 75 °C, 100°C, 150°C or 180°C. Thus, a discovery library of 96 samples was generated and evaluated by comparing the X-ray powder patterns of all products. Four important crystallization fields could be identified, represented here in a three-dimensional plot of the reaction parameters as green, blue, yellow and red regions (Figure 4.3 - 1). Within the described parameter range 14 new compounds were found, that could be assigned to three structure types with the general formulas **(Ln(H$_5$L)**, **Ln$_2$(H$_2$L)** and **NaLn(H$_4$L)** (Figure 4.3 - 2). The six compounds within structure type I were further sub-classified in **(Ln(H$_5$L) a-e** due to their different layer stacking.

Generally the parameter range for successful crystallization was limited by the pH. The reaction media were strongly acidic at NaOH-to-H$_8$L ratios of 0:1 and 4:1 and neutral to slightly basic at a NaOH-to-H$_8$L ratio of 8:1. Highly crystalline products were observed in the blue, yellow and red regions, which are located in the parameter field with acidic conditions. In neutral to slightly basic media, crystallization was only observed at a metal-to-ligand ratio of 1:1 (Figure 4.3 − 1, green), where the poorly crystalline phases 1-3 were observed. They show powder patterns consisting of only few broad signals (Figures 8.1.1 - 1 IV,
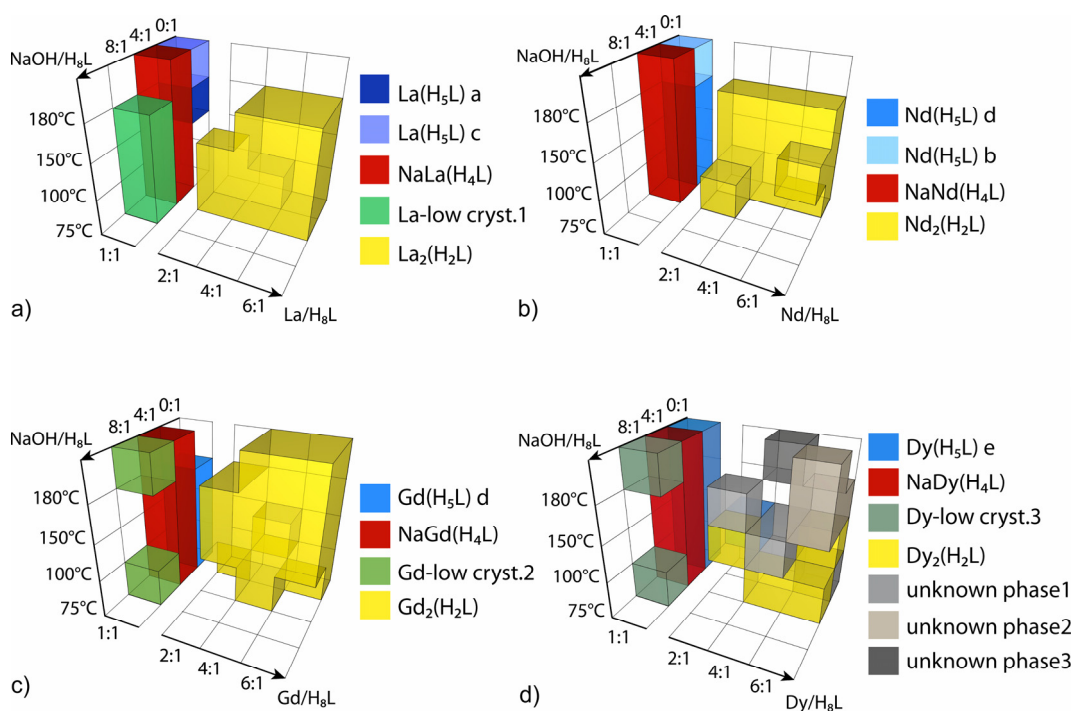
Figure 4.3 − 1: Results of the high-throughput screening of H8L with La3+ (a), Nd3+ (b), Gd3+ (c) and Dy3+ (d). Only roentgenographical pure phases are represented. A XRD of each phase is shown in the supporting information in chapter 8.1.1.
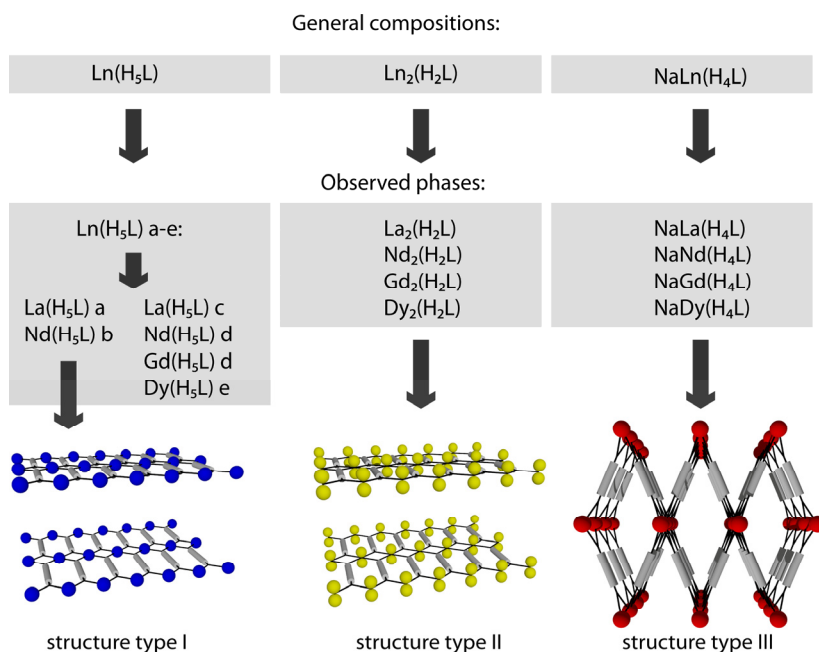
Figure 4.3 − 2: Assignment of the phases that crystallize in the blue, yellow and red coded regions of the parameter field, to three structure types. The subcategories (a-e) in structure type I stand for different layer stackings.

8.1.1 − 3 II and VI). Additionally, their morphology indicates the formation a poorly ordered layered material.

4.3.1 Structure type I

More interesting are the blue regions, which represent layered compounds with the composition Ln(H$_5$L). They were all formed at a lanthanide to ligand ratio of 1:1 without any NaOH addition. Slight changes in this crystallization system, such as variation of the lanthanide or the crystallization temperature, led to the formation of phases **Ln(H$_5$L) a-e** (Figure 4.3 − 2). Providing La^{3+} as framework metal, **La(H$_5$L) a** crystallized at 150 °C and **La(H$_5$L) c** at 180°C (Figure 4.3 − 1a). When NdNO$_3$ was the metal source, **Nd(H$_5$L) b** was formed in the temperature range from 75°C to 150°C and **Nd(H$_5$L) d** at 180°C (Figure 4.3 − 1b). In the Gd^{3+}-containing system **Gd(H$_5$L) d** crystallized in the range of 75°C to 150°C (Figure 4.3 − 1c). With Dy^{3+}, **Dy(H$_5$L) e** was formed over the whole temperature range (Figure 4.3 - 1d). A comparison of the powder patterns of these six compounds reveals the presence of five crystallographic different phases **(a - e)** (Figure 4.3 - 3). **Nd(H$_5$L) d** and **Gd(H$_5$L) d** are isomorphous. The structures of **Ln(H$_5$L) a** and **Ln(H$_5$L) b** could be solved.

The fine needles of **La(H$_5$L) a** were not suitable for single crystal structure analysis. However, performing a synthetic dilution series, the same structure type could be obtained with Nd^{3+} as lattice metal under more dilute conditions and in the presence of small amounts of ammonia **(Nd(H$_5$L) a)**. **Nd(H$_5$L) a** was obtained in the form of single crystals. The powder pattern simulated from the data of the structure solution of **Nd(H$_5$L) a** corresponds well with the experimental powder pattern of **La(H$_5$L) a** (Figure 8.1.1-1). Therefore the structure of **Nd(H$_5$L) a** (Figure 4.3 - 4) will be discussed as a representative for **Ln(H$_5$L) a** (Figure 4.3 - 2).
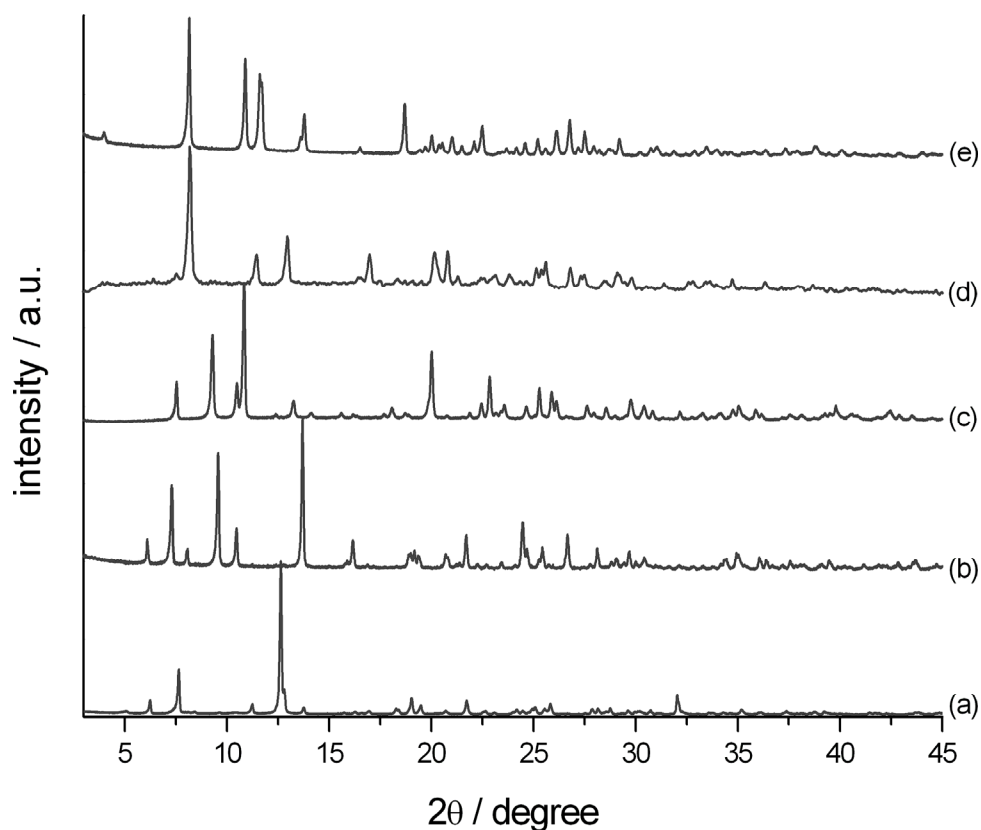
Figure 4.3 - 3: Powder patterns of phases crystallized at a lanthanide-to-H$_8$L ratio of 1:1: a) La(H$_5$L) a; b) **La(H$_5$L) c)** c) **Nd(H$_5$L) d** similar to **Gd(H$_5$L) d**; d) **Nd(H$_5$L) b**; e) **Dy(H$_5$L) e**.

The asymmetric unit of **Nd(H$_5$L) a** contains 29 non-hydrogen atoms and 19 hydrogen atoms (Figure 4.3 - 4a). The crystal structure is composed of [(PO$_3$H)$_2$CH-C$_6$H$_4$-CH(PO$_3$H)(PO$_3$H$_2$)]$^{3-}$ ions, La^{3+}-ions and water molecules. According to the P-O distances (Table 8.1.5 - 2) the phosphonate groups around P1, P3 and P4 are singly deprotonated while the group around P2 is not deprotonated. Additionally, at O1, O5, O6 and O12 hydrogen atoms could be localized and refined. At O7 a hydrogen atom could be found but not be refined. Nd^{3+} is eightfold coordinated (Figure 4.3 - 4b, Table 8.1.5 - 3). Four coordination sites are occupied by two bisphosphonate groups. The metal ion is chelated via O3 and O4 and via O9 and O10 forming a ring with chair conformation with each bisphosphonate group. Two other phosphonate groups
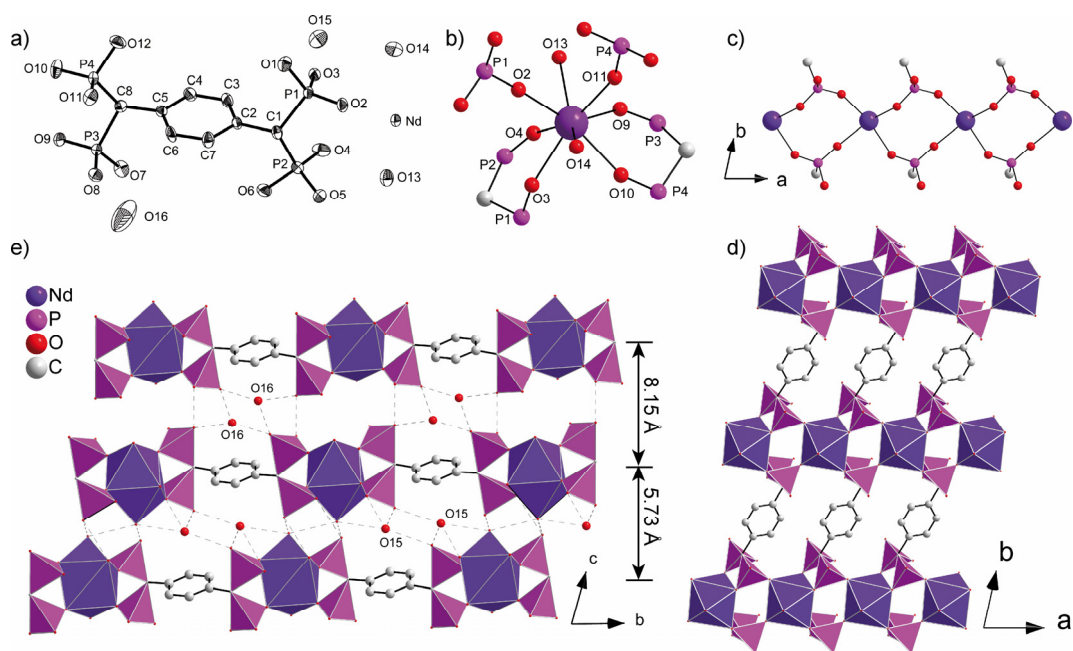
Figure 4.3 - 4: Structure of Nd[(PO$_3$H)$_2$CH-C$_6$H$_4$-CH(PO$_3$H)(PO$_3$H$_2$)]·4H$_2$O, **Nd(H$_5$L) a** (Hydrogens are omitted for clarity) : a) asymmetric unit (thermal ellipsoids are represented with a probability factor of 70 %) b) coordination of Nd^{3+} c) phosphonate-bridged chain of Nd^{3+} along **c** d) 2 D coordination network in the (010) plane; e) projection along **a** showing a cross section of the layers.

coordinate via O2 and O11, acting as monodentate ligands. The remaining two coordination sites are occupied by the water molecules around O13 and O14. Adjacent Nd^{3+} ions are linked into rows along a by bridging phosphonate groups (Figure 4.3 - 4c). The organic linker, which coordinates in bidentate fashion to Nd^{3+} ions of two neighboring rows, extends these chains into a two-dimensional coordination network in the (001) plane (Figure 4.3 - 4d). The phosphonate groups that do not participate in the bridging of the metal polyhedra, all stick out to one side of the layer. The layers stack in *c*-direction on top of each other (Figure 4.3 - 4e) and are staggered in AABB mode. Two adjacent layers are orientated face to face with a short interlayer distance of 5.73 Å. They are joined together by hydrogen bonds between phosphonate groups and the coordinating water molecules of the next layer. Additionally, the free water molecule (O15) assists in the bonding interactions between layers. The distance between such a layer pair is 8.15 Å. Between the layer pairs the non-bridging phosphonate

groups form hydrogen bonds among each other and with the water molecule around O16 (Table 8.1.5 - 4).

The second phase whose structure was solved, corresponds to **Ln(H$_5$L) b** (Figure 4.3 - 2). The crystals of **Nd(H$_5$L) b** are large blocks that grew readily in the concentrated synthesis mixture of the initial high-throughput reaction to an average size of about 100 μm. Under more diluted conditions and at lower temperature single crystals of an isotypical compound with La^{3+} as lattice metal could be obtained (**La(H$_5$L) b**). The experimental powder pattern of **Nd(H$_5$L) b** agrees well with the one simulated from the data of the structure solution of **Nd(H$_5$L) b** and **La(H$_5$L) b** (Figure 8.1.1.-2). Here the structure of **La(H$_5$L) b** will be discussed representatively. With regard to the content of the asymmetric unit, the metal coordination and the formation of the coordination network, the structure of **La(H$_5$L) b** coincides with **Ln(H$_5$L) a**. The asymmetric unit of **La(H$_5$L) b** contains 29 non-hydrogen atoms and 19 hydrogen atoms. The crystal structure is assembled of $[(PO_3H)_2CH-C_6H_4-CH(PO_3H)(PO_3H_2)]^{3-}$ ions, La^{3+}-ions and water molecules (Figure 4.3 - 5a). The hydrogen atom positions H2 and H12 close to O2 and O12 are half occupied. The O2-H2 distance and the O12-H12 distance are both very long (1.21 Å) because the hydrogen atoms are located in the middle of a symmetric hydrogen bond. Consequently three phosphonic acid groups are singly deprotonated and one is not deprotonated. This can be reaffirmed by the P-O distances (Table 8.1.5 - 5). The La^{3+}-ion is coordinated by eight oxygens (Figure 4.3 - 5b, Table 8.1.5 - 6). Four coordination sites are occupied by bidentate chelating bisphosphonate ligands (O1, O5, O7, O10), two by monodentate phosphonate ligands (O6, O8), and two by water molecules (O13, O14), respectively. The monodentate coordinating phosphonate group bridges the La^{3+}-ions into rows parallel to the a-axis (Figure 4.3 - 5c). The organic linker, which coordinates in a bidentate fashion to La^{3+} ions of two neighboring rows, extends these rows into a two-dimensional coordination
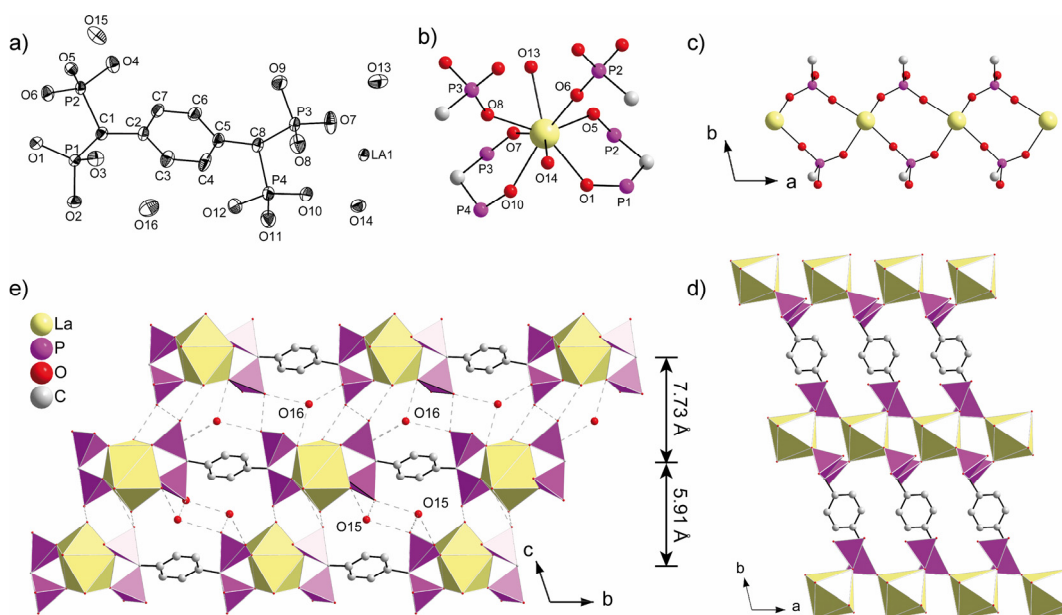
Figure 4.3 - 5: Structure of La[(PO$_3$H)$_2$CH-C$_6$H$_4$-CH(PO$_3$H)(PO$_3$H$_2$)]·4H$_2$O, **La(H$_5$L) b** (Hydrogens are omitted for clarity): a) asymmetric unit (thermal ellipsoids are represented with a probability factor of 70 %.) b) coordination of La^{3+} c) phosphonate-bridged chain of lanthanum along *a* d) 2D coordination network in the (001) plane; e) projection along a showing a cross section of the layers .

network in the (001) plane (Figure 4.3 - 5d). The layers are staggered in AABB mode along *c* (Figure 4.3 - 5e). Two adjacent layers are oriented face to face with a short interlayer distance of 5.91 Å. They are joined together by hydrogen bonds between phosphonate groups and the coordinating water molecules of the next layer. Additionally, the free water molecule around O 15 holds the layers together. Similar as in **Nd(H$_5$L) a**, the phosphonate groups that do not participate in the bridging of the metal polyhedra, all stick out on one side of a layer. Unlike **Nd(H$_5$L) a,** the non-bridging phosphonate group around P1 is 120 ° twisted (Figure 4.3 - 5d) against the phosphonate group around P2. This allows the formation of two short and symmetrical hydrogen bonds, O2-H···O2 and O12-H···O12, and additional hydrogen bridging between the phosphonate group around P1 and the coordinating water molecule around O14 (Table 8.1.5 - 7). Thus, the distance between to layer pairs decreases from 8.15 Å in

Nd(H$_5$L) a to 7.73 Å in **La(H$_5$L) b.** The denser packing in the stacking direction may favor the growth of compact blocks over flat needles like in **Nd(H$_5$L) a**.

Ln(H$_5$L) a and **Ln(H$_5$L) b** are very similar. Nevertheless they have different powder patterns due to their different layer stacking, as all five phases found in this parameter range. On the other hand all five phases coincide in the metal-to-ligand ratio, based on EDX analysis. They exhibit similar Raman spectra that confirm the presence of **H$_5$L** in all compounds (Figure 4.3 - 6). **La(H$_5$L) a** crystallized in the form of fine needles, **La(H$_5$L) c** as rods and **Nd(H$_5$L) b** in the shape of blocks. **Nd(H$_5$L) d** and **Gd(H$_5$L) d** show both intergrown platelets and **Dy(H$_5$L) e** grows in the shape of small rods (Figure 8.1.2 - 1). For all compounds, images at higher magnification revealed features that indicate a layered assembly, such as smooth top faces and lengthwise fissured side faces (Figure 4.3 - 7). Furthermore, thermogravimetric analysis showed that they are very similar in their combustion behavior. They all degrade in three main steps (Figure 8.1.4 - 1): After a water loss of about 10 %, a second endothermal phase transformation occurs between 300 °C and 400 °C, until at 600 °C an exothermal oxidative destruction of the carbon network begins. Summarizing all these features, it can be stated that all five phases show similar two-dimensional coordination frameworks and vary mainly in the stacking mode of their layers. Therefore they can be combined as isotypical and described with **Structure type I** (Figure 4.3 - 2).
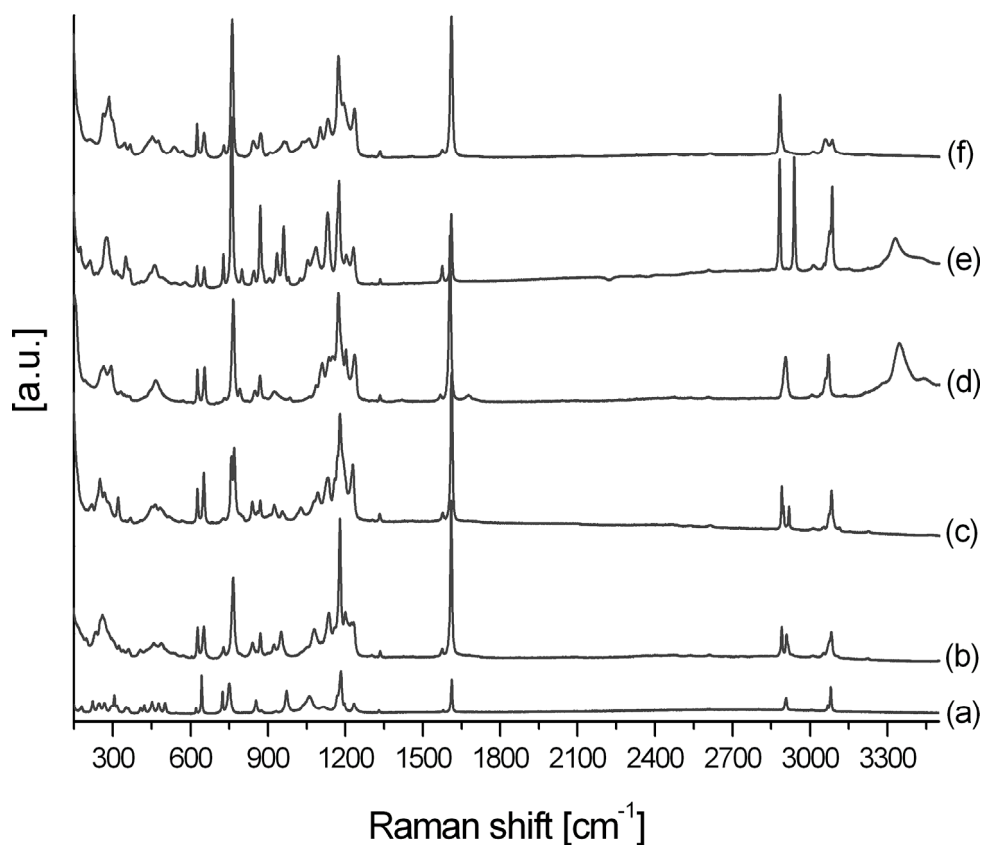
Figure 4.3 - 6: Raman spectra of H$_8$L and the phases crystallized at a lanthanide-to-H$_8$L ratio of 1:1: a) **H$_8$L**; b) **La(H$_5$L) a**; c) **La(H$_5$L) c**; d) **Nd(H$_5$L) d**; e) **Nd(H$_5$L) b**; f) **Dy(H$_5$L) e**.
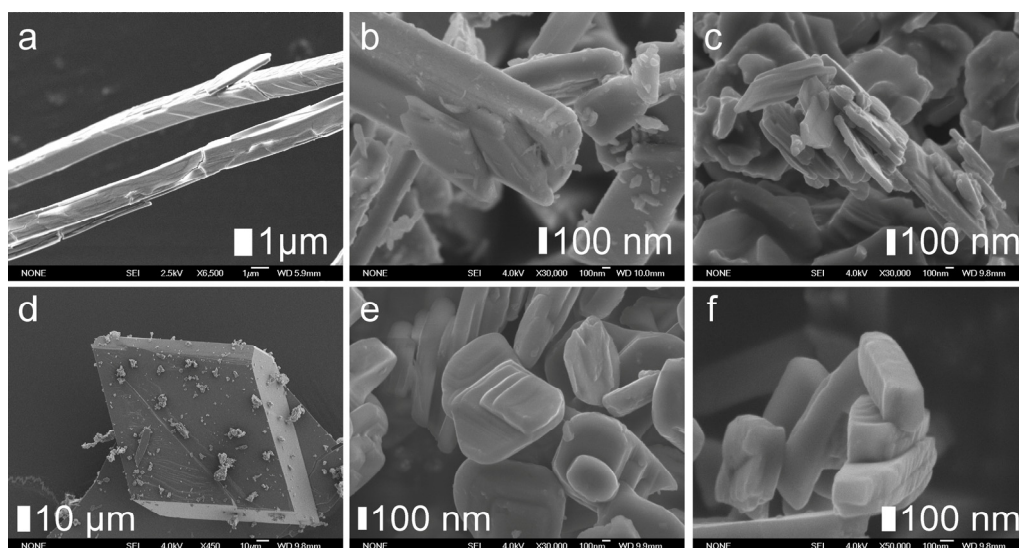
Figure 4.3 - 7: SEM micrographs of compounds crystallized at a batch composition of Ln^{3+}: H$_8$L = 1:1: a) La(H$_5$L) a; b) **La(H$_5$L) c**; c) **Nd(H$_5$L) d**; d) **Nd(H$_5$L) b**; e) **Gd(H$_5$L) d**; f) **Dy(H$_5$L) e** (high magnification).

4.3.2 Structure type II

The yellow regions in Figure 4.3 - 1 describe the crystallization fields of layered compounds with the composition Ln$_2$(H$_2$L), which correspond to structure type II (Figure 4.3 - 2). Their crystallization was achieved by an increase of the metal-to-ligand ratio. In the La^{3+} containing system, four equivalents of NaOH facilitate the crystallization process (Figure 4.3 - 1a). With NaOH, **La$_2$(H$_2$L)** crystallized between 75 °C and 100 °C at metal-to-ligand ratios between 2 :1 and 6:1. At 150 °C it could be observed at metal-to-ligand ratios of 4:1 and 6:1. Without NaOH, more drastic conditions were necessary. Then the formation of **La$_2$(H$_2$L)** required at 75 °C a metal-to-ligand ratio of 6:1. Between 100 °C and 150 °C an excess metal-to-ligand ratio between 4:1 and 6:1 had to be provided. In the Nd^{3+} containing system four equivalents of NaOH are less favorable (Figure 4.3 - 1b). Without NaOH, **Nd$_2$(H$_2$L)** is formed at 75 °C at metal-to-ligand ratios between 4:1and 6:1. From 100°C to 150 °C it could be obtained at metal-to-ligand ratios between 2:1 and 6:1. In the presence of NaOH, **Nd$_2$(H$_2$L)** crystallized only at 75°C at a metal-to-ligand ratio of 2:1 and at 100 °C at a metal-to-ligand ratio of 6:1. In the Gd^{3+} containing system, 4 equivalents of NaOH did not have a significant influence, as **Gd$_2$(H$_2$L)** crystallized with and without NaOH in nearly the whole temperature range at all excess metal-to-ligand ratios (Figure 4.3 - 1c). Exceptions in the presence of NaOH were the metal-to-ligand ratios of 2:1 and 6:1 at 75 °C, and the metal-to-ligand ratio of 2:1 at 180°C. Without NaOH, **Gd$_2$(H$_2$L)** was not formed at the metal-to-ligand ratio of 4:1 at 100 °C and at the metal to ligand ratio of 2:1 at 180 °C. In the Dy^{3+} containing system, the yellow crystallization field is small compared to the other lanthanides (Figure 4.3 - 1d). In the presence of four equivalents NaOH, pure phase Dy$_2$**(H$_2$L)** was observed at 75°C at metal-to-ligand ratios between 4:1 and 6:1. At 100°C it was formed at a metal-to-ligand ratio of 2:1. Without NaOH, **Dy$_2$(H$_2$L)** was generated at 100°C

and a metal-to-ligand ratio of 6:1. Furthermore, three unkown phases were observed.

La₂(H₂L), **Nd₂(H₂L)**, **Gd₂(H₂L)** and **Dy₂(H₂L)** are isomorphous (Figure 4.3 - 8). Raman spectra show that the ligand **H₂L** was incorporated in the structure (Figure 8.1.3 - 1). EDX analysis reveals an increased lanthanide to ligand ratio of 2:1 (Ln : P = 1 : 2) for all four compounds. Depending on the reaction media, they crystallize in the shape of large blocks or as intergrown platelets. Single crystalline blocks of **La₂(H₂L)** were obtained from concentrated and metal-rich synthesis mixtures (Figure 4.3 - 9a). Under more dilute conditions, **La₂(H₂L)** forms agglomerates of twisted sheets (Figure 4.3 - 9b). The structure could be solved from the single crystalline blocks. The simulated theoretical pattern fits well with the experimental data (Figure 8.1.1-2). Therefore the structure of **La₂(H₂L)** can be discussed exemplarily for structure type **II** (Figure 4.3 - 1): Single crystal structure analysis revealed the composition of $La_2[(HO_3P)(O_3P)$-CH-C_6H_4-CH-$(PO_3)(PO_3H)]\cdot8H_2O$. The asymmetric unit contains 17 non-hydrogen atoms and 12 hydrogen atoms. The crystal structure is composed of $[(HO_3P)(O_3P)$-C_6H_4-$(PO_3)(PO_3H)]^{6-}$ ions, La^{3+}-ions and water molecules (Figure 4.3 - 10a). According to the P-O distances, the phosphonic acid group around P1 is fully deprotonated and the phosphonic acid group around P2 is only once deprotonated (Table 8.1.5 - 8). In good agreement, one hydrogen atom could be located next to O5. The La^{3+}-ion has eightfold coordination geometry (Figure 4.3 - 10b). It is coordinated by two bidentate chelating bisphosphonate units (O2; O1 and O4; O6), one bidentate coordinating phosphonate group (O3; O4) and two water molecules (O7, O6). The phosphonate La-O distances are in the range between 2.66 Å and 2.44 Å, which is comparable to those reported for $LaPO_4$ [166] (Table 8.1.5 - 9). The La-O$_{water}$ distances are 2.51 Å and 2.61 Å. O4 coordinates to two La^{3+} ions. This associates two La^{3+} complexes into dimeric units (Figure 4.3 - 10c). The lanthanum dimers can be represented as two edge-
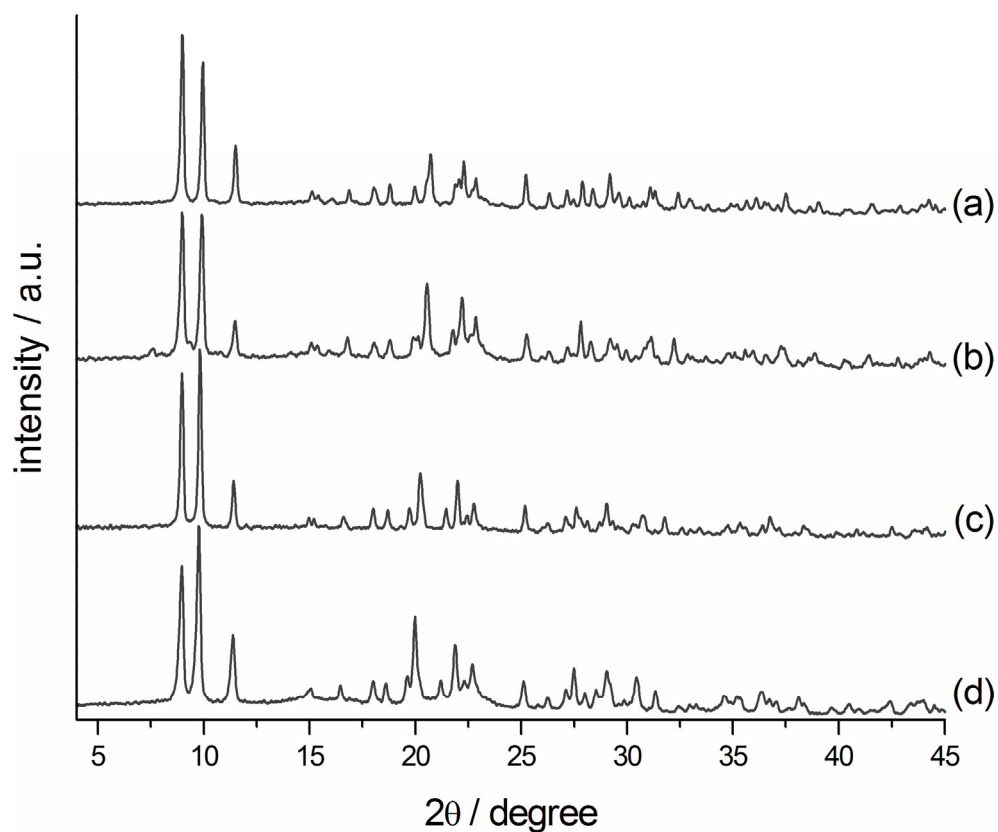
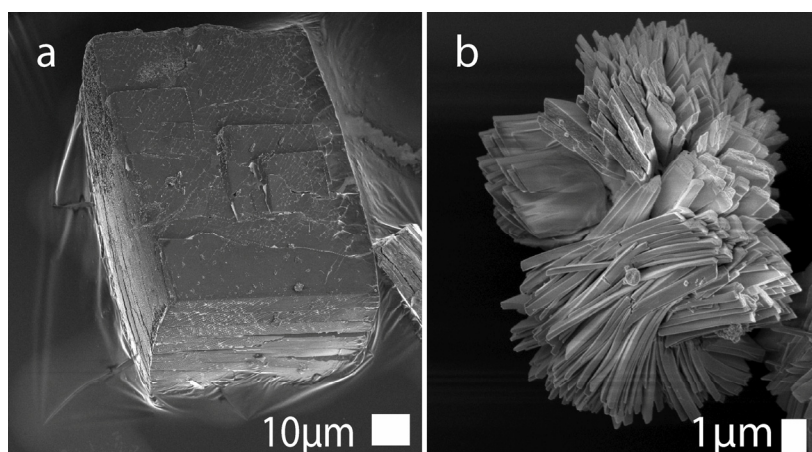Figure 4.3 - 8: Powder pattern of a) Dy$_2$(H$_2$L), b) Gd$_2$(H$_2$L), c) Nd$_2$(H$_2$L) and d) La$_2$(H$_2$L)

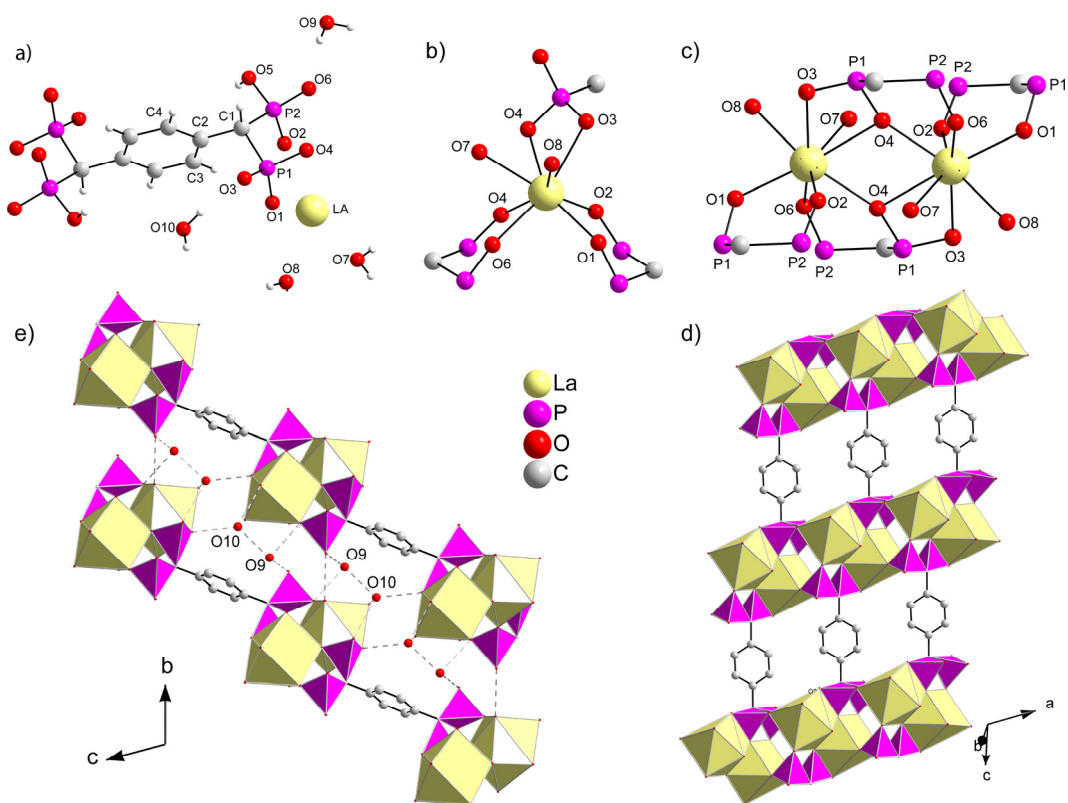Figure 4.3 - 9: crystal morphologies of La$_2$(H$_2$L): a) single crystalline blocks b) twisted sheets.

Figure 4.3 - 10: Structure of La$_2$[(HO$_3$P)(O$_3$P)-CH-C$_6$H$_4$-CH-(PO$_3$)(PO$_3$H)] ·8H$_2$O, La$_2$(H$_2$L) (hydrogen atoms are omitted for clarity) : a) asymmetric unit with completed molecular fragments b) coordination of La^{3+} c) association of two La^{3+} ions into a dinuclear cluster via two La-O-La bridges. d) 2D coordination network; e) projection along [100] showing a cross section of the layers.

sharing coordination polyhedra; they are connected along (100) into a chain by bridging phosphonate groups (Figure 4.3 - 10d). The chains are linked by the organic spacer of **H$_2$L**, resulting in a two-dimensional coordination network in the (001) plane. The remaining two crystallographically independent water molecules around O9 and O10 are located between the layers (Figure 4.3 - 10e). The layers stick together by weak interactions such as hydrogen bonds and Van-der-Waals interactions. The interlayer distance is 9.91 Å. In good agreement with this structure description, thermogravimetric analysis of the compounds **La$_2$(H$_2$L)**, **Nd$_2$(H$_2$L)**, **Gd$_2$(H$_2$L)** and **Dy$_2$(H$_2$L)** show a weight loss of 16 − 18 % in two endothermic steps between 60°C and 150°C as well as 150°C and 250°C that correspond to the loss of the eight stoichiometric equivalents of water in

the structure formula (Figure 8.1.4 - 2). The two steps can be explained by the different bonding modes of water. Coordinating water is supposed to leave the structure at higher temperatures compared to free crystal water.

4.3.3 Structure type III

The red regions in Figure 1 describe the crystallization field of compounds with the composition **NaLn(H$_4$L)** (Figure 4.3 - 1), which corresponds to **structure type III** (Figure 4.3 - 2). They crystallize from the batch composition La^{3+} : H$_8$L : NaOH = 1 : 1 : 4. Their formation seems strongly favorable, and is not affected by either significant temperature changes or a variation of the nature of the lanthanide. This structure type was observed with all four metals and over the whole temperature range. In dilution series the crystal size of **NaLa(H$_4$L)** could be tuned from 10 μm to 150 μm. Up to a synthesis temperature of 100 °C, crystals appear nearly square bipyramidal (Figure 4.3 - 11a). At elevated temperatures of 150 °C, crystal growth becomes faster in one preferential direction. The crystals grew as rods with rhombs on the top and at the bottom (Figure 4.3 - 11b). The crystals of **NaDy(H$_4$L)** showed a curious hole in the middle (Figure 4.3 - 11c). **NaLa(H$_4$L)**, **NaNd(H$_4$L)**, **NaGd(H$_4$L)** and **NaDy(H$_4$L)** are all isomorphous (Figure 4.3 - 12). Raman spectra show that they incorporate the ligand **H$_4$L** (Figure 8.1.3-2). With EDX analysis, in all four compounds one equivalent of sodium was detected for each equivalent of lanthanide and ligand. Single crystals of **NaLa(H$_4$L)** were obtained and its structure could be resolved. The experimental powder pattern of **NaLa(H$_4$L)** matches very well with the pattern simulated from the structure solution (Figure 8.1.1-1). Therefore the structure of **NaLa(H$_4$L)** will be discussed representatively for **structure type III.** The asymmetric unit of **NaLa(H$_4$L)** contains 30 non-hydrogen atoms and 17 hydrogen atoms (Figure 4.3 - 13a). The crystal structure is composed of [(PO$_3$H)$_2$CH-C$_6$H$_4$-CH(PO$_3$H)$_2$]$^{4-}$ ions, La^{3+} ions, Na$^+$ ions and four
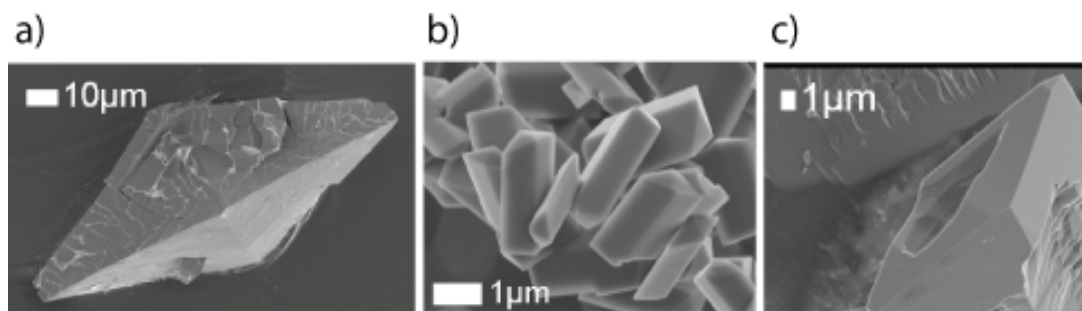
Figure 4.3 - 11: Crystal morphologies of LnNa[(PO$_3$H)$_2$CH-C$_6$H$_4$-CH(PO$_3$H)$_2$]·4H$_2$O: a) **NaLa(H$_4$L)** synthesised at 100 °C; b) **NaGd(H$_4$L)** synthesised at 150 °C; c) **NaDy(H$_4$L)** synthesised at 150°C.
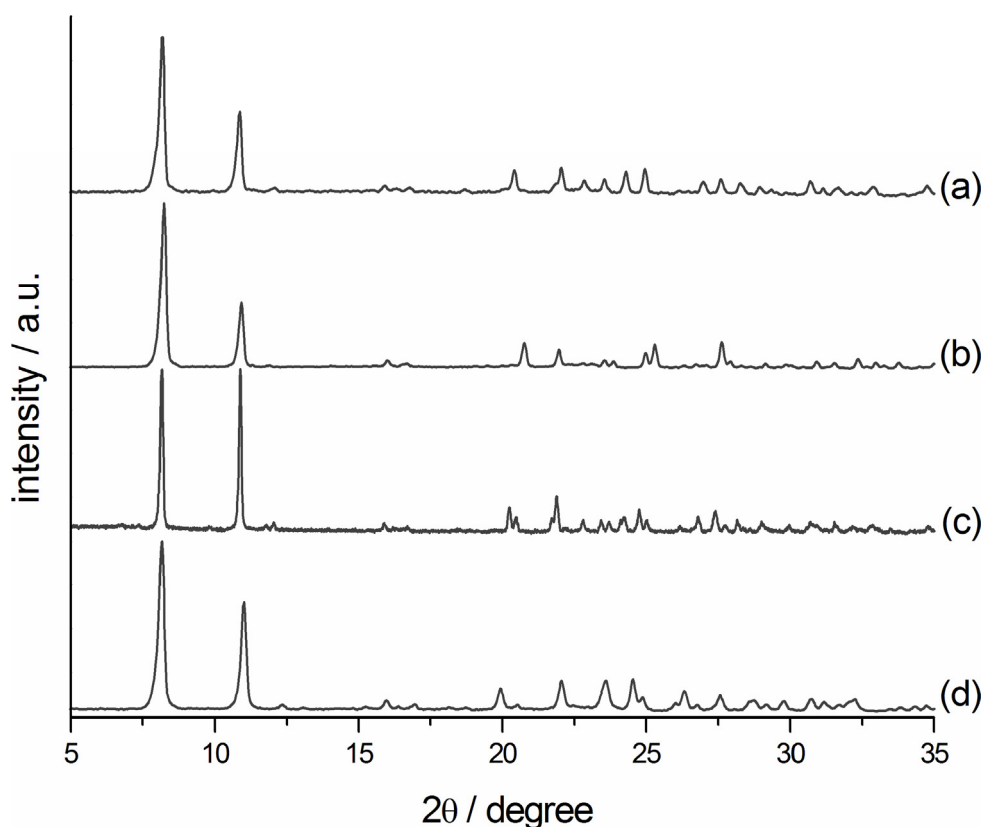

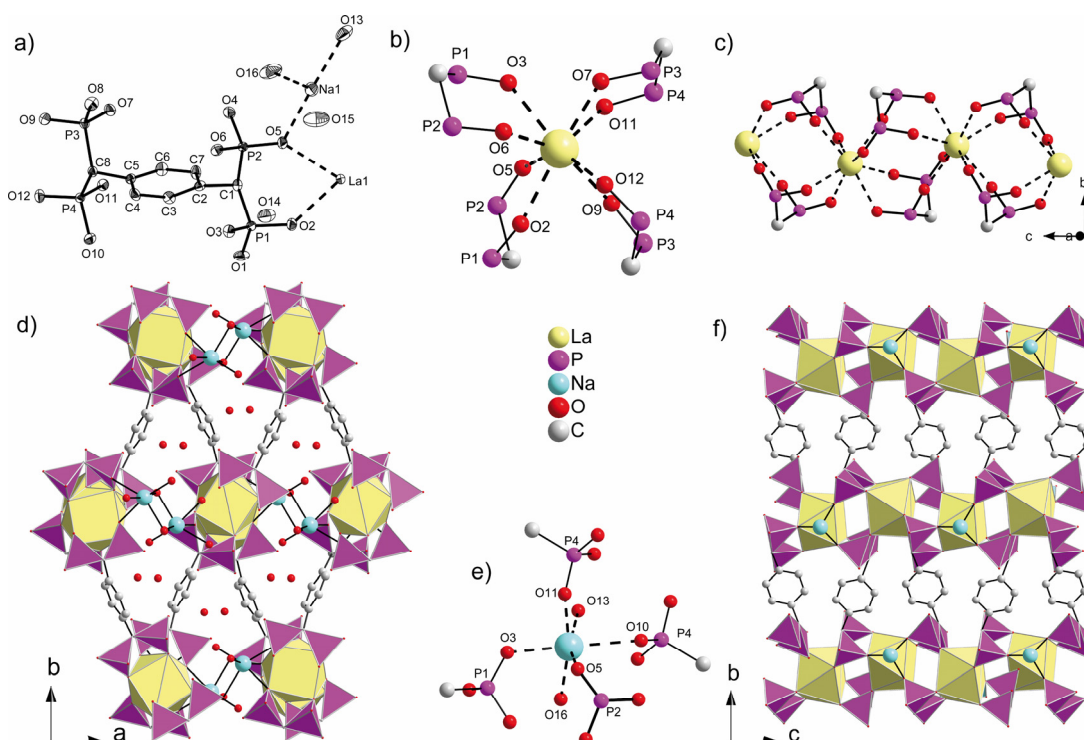Figure 4.3 - 12: Powder patterns of NaDy(H$_4$L) (a), NaGd(H$_4$L) (b), NaNd(H$_4$L) (c), and NaLa(H$_4$L) (d).

Figure 4.3 - 13: Structure of LaNa[(PO$_3$H)$_2$CH-C$_6$H$_4$-CH(PO$_3$H)$_2$]·4H$_2$O, **NaLa(H$_4$L)** (hydrogen atoms are omitted for clarity): a) asymmetric unit (thermal ellipsoids are represented with a probability factor of 70 %.) b) coordination of La^{3+} c) phosphonate-bridged chain of La^{3+} running along **c.** d) Cross section of the one-dimensional rhombic channels formed by the connection of the chains with the organic spacer. e) coordination of Na$^+$ f) Projection along **a** showing the decoration of the chains with sodium ions.

crystallographically independent water molecules. According to the P-O distances, all four phosphonic acid groups are singly deprotonated (Table 8.1.5 - 11). Additionally, hydrogen atoms could be refined at O1, O4, O8 and O10. As in structure types **I** and **II**, the La^{3+} ions are eightfold-coordinated by phosphonate oxygens from four (H$_4$L)$^{4-}$ ligands. The La-O distances are between 2.44 Å and 2.60 Å, which is comparable to those reported for LaPO$_4$[166] (Table 8.1.5 - 12). The distinctive feature of structure type **III** is the exclusive coordination of the lanthanide ions by bisphosphonate groups. Four bidentate ligands are chelating one La^{3+}-ion, two in chair and two in boat conformation

(Figure 4.3 - 13b). Additionally, each phosphonate group bridges to a neighboring La^{3+} ion in a way that a chain is built along **c** (Figure 4.3 - 13c). The organic spacer of the ligand connects the chains among each other (Figure 4.3 - 13d and f). The coordinating oxygen atoms around La^{3+} form a square antiprism. The top square of this antiprism is decorated by bisphosphonates around P1 and P2, the bottom square of bisphosphonates around P3 and P4. The coordination geometry of the lanthanide is transferred to the structure of the coordination polymer through the twist angle between the two squares. Thus a three-dimensional open framework with a one-dimensional channel system along [001] is generated (Figure 4.3 - 13d). Sodium ions and water molecules reside as guests in the channels. Sodium has a strongly distorted octahedral coordination by four phosphonate oxygens and two water molecules (Figure 4.3 - 13e). The Na-O distances range from 2.22 Å to 2.66 Å (Table 8.1.5 - 13)[167]. With three bonds it coordinates to one side of the channel wall. Sodium is connected via O11, O5 and O3 to the triangular side-face of the La^{3+} polyhedra alternating on both sides of the chain (Figure 13f). On the side that points into the channel center, Na$^+$ is coordinated by two water molecules (O11, O16). The sixth interaction with a Na-O distance of 2.67 Å is very weak. It reaches to the chain running on the opposite side of the channel. The two remaining water molecules that do not coordinate to sodium reside as free crystal water above and below the sodium ions in the center of the channels.

Furthermore, compounds with structure type **III** stand out from type **I** and **II** compounds by a distinctive and consistent TGA profile (Figure 8.1.4 - 3). Thermogravimetric analysis shows three prominent steps of weight loss for **NaLa(H$_4$L)**, **NaNd(H$_4$L)**, **NaGd(H$_4$L)** and **NaDy(H$_4$L)**. Step 1 with a weight loss of 11 % corresponds to the loss of the four water molecules per asymmetric unit. Remarkably, the temperature necessary for the removal of water increases from La^{3+} (60°C − 160 °C) to Dy^{3+} (110°C − 210 °C). Similar to phases with

structure type **I**, an endothermal phase transformation takes place between 300 °C and 450 °C (step 2). Between 500 °C and 600 °C oxidation and combustion of the carbon framework occurs in an exothermal third step.

4.4 Conclusions

In this study we could show that H_8L, providing two bisphosphonate moieties as large chelating ligands that are separated by a phenyl spacer, is a suitable ligand for lanthanides in the synthesis of metal-organic frameworks. In high-throughput screening experiments we discovered three new structure types of lanthanide tetrakisphosphonates. Structure type **I** is formed by H_8L with one equivalent of metal. It comprises various layered structures on the basis of a two-dimensional coordination network where the lanthanide is coordinated by bisphosphonate groups, phosphonate groups and water molecules. If an excess of lanthanide ions is present during synthesis, compounds with structure type **II** are formed, where the metal centers of the two-dimensional coordination network are associated to dimers. The most interesting structure type emerges when four equivalents of NaOH are added to the reaction mixture of H_8L, with one equivalent of metal. With this synthesis stoichiometry, crystals with the three-dimensional open framework of structure type **III** were obtained over a broad range of temperatures and concentrations. In this structure type, a well-defined coordination geometry was achieved with the lanthanide ions coordinated by bisphosphonate units in an exclusively bidentate fashion. This structure features a one-dimensional rhombic channel system with sodium ions and water molecules acting as guests. This shows that the bisphosphonate group connected to an aromatic spacer provides excellent access to MOFs of metals with high coordination numbers that are not easily synthesized with other ligands. H_8L can be obtained by a general synthesis route that will also permit the preparation of building blocks with larger organic spacers. This

would open the way to the synthesis of isoreticular MOFs with the general motif of structure type **III**. Additionally, the expansion of the range of synthesis parameters, which is currently still limited to aqueous media, might lead to new and interesting three-dimensional networks.

4.5 References

(1)   Cheetham, A. K.; Rao, C. N. R.; Feller, R. K. *Chem.Commun.* 2006, 4780.

(2)   Rosseinsky, M. J. Microporous and Mesoporous Mater. 2004, 73, 15.

(3)   Eddaoudi, M.; Moler, D. B.; Li, H.; Chen, B.; Reineke, T. M.; O'Keeffe, M.; Yaghi, O. M. *Acc. Chem. Res.* 2001, *34*, 319.

(4)   Tranchemontagne, D. J.; Ni, Z.; O'Keeffe, M.; Yaghi, O. M. *Angew.Chem., Int. Ed.* 2008, *47*, 5136.

(5)   Clearfield, A. *Metal Phosphonate Chemistry*; John Wiley & Sons, Inc: New York, 1998; Vol. 47.

(6)   Rabu, P.; Janvier, P.; Bujoli, B. *J. Mater. Chem.* 1999, *9*, 1323.

(7)   Stock, N.; Bein, T. *J. Solid State Chem.y* 2002, *167*, 330.

(8)   Irran, E.; Bein, T.; Stock, N. *J. Solid State Chem.* 2003, *173*, 293-298.

(9)   Gomez-Alcantara, M. d. M.; Cabeza, A.; Moreno-Real, L.; Aranda, M. A. G.; Clearfield, A. *Microporous Mesoporous Mater.* 2006, *88*, 293-303.

(10)   Konar, S.; Zon, J.; Prosvirin, A. V.; Dunbar, K. R.; Clearfield, A. *Inorg.Chem.* 2007, *46*, 5229.

(11)   Cabeza, A.; Aranda, M. A. G.; Bruque, S.; Poojary, D. M.; Clearfield, A.; Sanz, J. *Inorg. Chem.* 1998, *37*, 4168.

(12)   Serpaggi, F.; Ferey, G. *J. Mater. Chem.* 1998, *8*, 2749.

(13)   Stock, N.; Guillou, N.; Bein, T.; Ferey, G. *Solid State Sci.* 2003, *5*, 629.

(14)   Clearfield, A. *Dalton Trans.* 2008, 6089.

(15)   Wang, Z.; Heising, J. M.; Clearfield, A. *J. Am. Chem. Soc.* 2003, *125*, 10375.

(16)   D. Kong, J. Z., J. McBee, A. Clearfield *Inorg. Chem.* 2006, *45*, 977.

(17)   Liang, J.; Shimizu, G. K. H. *Inorg. Chem.* 2007, *46*, 10449-10451.

(18)   Cao, D.-K.; Li, Y.-Z.; Song, Y.; Zheng, L.-M. *Inorg. Chem.* 2005, *44*, 3599.

(19)   Cao, D.-K.; Liu, Y.-J.; Song, Y.; Zheng, L.-M. *New J. Chem.* 2005, *29*, 721.

(20)   Bauer, S.; Bein, T.; Stock, N. *J. Solid State Chem.* 2006, *179*, 145-155.

(21)   Cao, D.-K.; Xiao, J.; Li, Y.-Z.; Clemente-Juan, J. M.; Coronado, E.; Zheng, L.-M. *Eur. J. Inorg. Chem.* 2006, 1830.

(22)   Bauer, S.; Stock, N. *J. Solid State Chem.* 2007, *180*, 3111.

(23)   Cao, D.-K.; Li, Y.-Z.; Zheng, L.-M. *J. Solid State Chem.* 2006, *179*, 573.

(24)   Sonnauer, A.; Naether, C.; Hoeppe, H. A.; Senker, J.; Stock, N. *Inorg. Chem.* 2007, *46*, 9968.

(25)   Bauer, S.; Marrot, J.; Devic, T.; Ferey, G.; Stock, N. *Inorg. Chem.* 2007, *46*, 9998.

(26)   Hill, R. J.; Long, D.-L.; Hubberstey, P.; Schroeder, M.; Champness, N. R. J. Solid State Chem. 2005, 178, 2414-2419.

(27)   Glover, P. B.; Bassett, A. P.; Nockemann, P.; Kariuki, B. M.; Van Deun, R.; Pikramenou, Z. *Chem. Eur. J.* 2007, *13*, 6286.

(28)   Harbuzaru, B. V.; Corma, A.; Rey, F.; Atienzar, P.; Jorda, J. L.; Garcia, H.; Ananias, D.; Carlos, L. D.; Rocha, J. *Angew. Chem., Int. Ed.* 2008, *47*, 1080.

(29)   Park, O.-H.; Seo, S.-Y.; Bae, B.-S.; Shin, J. H. *App. Phys. Let.* 2003, *82*, 2787.

(30)   Romanelli, M.; Kumar, G. A.; Emge, T. J.; Riman, R. E.; Brennan, J. G. *Angew. Chem., Int. Ed.* 2008, *47*, 6049.

(31)   Sun, L.-N.; Zhang, H.-J.; Fu, L.-S.; Liu, F.-Y.; Meng, Q.-G.; Peng, C.-Y.; Yu, J.-B. *Adv. Funct. Mater.* 2005, *15*, 1041.

(32)   Tang, Z.-H.; Liu, D.-Y.; Tang, Y.; Cao, X.-P. *Z. Anorg. Allg. Chem.* 2008, *634*, 392.

(33)   Yanagida, S.; Hasegawa, Y.; Murakoshi, K.; Wada, Y.; Nakashima, N.; Yamanaka, T. *Coord. Chem. Rev.* 1998, *171*, 461.

(34)   Yang, J.; Zhang, C.; Li, C.; Yu, Y.; Lin, J. *Inorg. Chem.* 2008, *47*, 7262.

(35)   Zhong, J.; Liang, H.; Lin, H.; Han, B.; Su, Q.; Zhang, G. *J. Mater. Chem.* 2007, *17*, 4679.

(36)   Lin, P.-H.; Burchell Tara, J.; Clerac, R.; Murugesu, M. *Angew Chem Int Ed* 2008, *47*, 8848.

(37)   Qiu, Y.; Liu, H.; Ling, Y.; Deng, H.; Zeng, R.; Zhou, G.; Zeller, M. *Inorg. Chem. Commun.* 2007, *10*, 1399.

(38)   Zhao, J.; Long, L.-S.; Huang, R.-B.; Zheng, L.-S. *Dalton Trans.* 2008, 4714.

(39)   Guo, X.; Zhu, G.; Li, Z.; Chen, Y.; Li, X.; Qiu, S. *Inorg. Chem.* 2006, *45*, 4065.

(40)   Guo, X.; Zhu, G.; Sun, F.; Li, Z.; Zhao, X.; Li, X.; Wang, H.; Qiu, S. *Inorg. Chem.* 2006, *45*, 2581.

(41)   Li, Z.; Zhu, G.; Guo, X.; Zhao, X.; Jin, Z.; Qiu, S. *Inorg. Chem.* 2007, *46*, 5174.

(42)   Clearfield, A. *Chem. Mater.* 1992, *4*, 864.

(43)   Platt, A. W. G. *Inorg Chim. Acta* 1994, *223*, 43.

(44)   Stock, N.; Bein, T. *Angew. Chem., Int. Ed.* 2004, *43*, 749.

(45)   Sheldrick, G. *Acta Cryst. Sect. A* 2008, *64*, 112.

(46)   Cheetham, A. K.; Ferey, G.; Loiseau, T. *Angew. Chem., Int. Ed.* 1999, *38*, 3268.

(47)   Jaulmes, S. *Bull. Soc. Fr. Min. Crist.* 1972, *95*, 42.

(48)   Averbuch-Pouchot, M. T.; Durif, A. *J. Solid State Chem.* 1983, *46*, 193.

5 Exceptional Ion-Exchange Selectivity in a Flexible Open Framework Lanthanum(III)tetrakisphosphonate

5.1 Introduction

In the early days of research in the field of metal organic frameworks (MOFs), it was believed that rigidity of the host network was a prerequisite for their successful performance as porous materials, because it was assumed that flexibility would lead to a collapse of the structure[1]. This perspective has changed fundamentally. The discovery of a series of flexible porous coordination frameworks demonstrated that some MOF materials can change their cell volumes significantly (some of them by up to 40%[2] or even 170%[3]) while preserving their basic structures.[4-12] Representative examples include flexible porous carboxylates formed by chains of metallic centers[2,13,14] or metal-center trimers[15,16] (M = Cr^{3+}, Al^{3+}, Fe^{3+}) that are connected by organic linkers to form three-dimensional coordination networks. It could be shown that these structures adapt their pore sizes to the type and number of guest species, while the connections between the inorganic nodes via organic linkers remain intact[3,13]. In this process, weak interactions such as hydrogen bonding between the guest molecules and the framework play a decisive role,[17] and can lead to selectivity for specific guest species[18,19].

The adaptation of a framework to accommodate a specific guest has also been observed to a lesser extent in inorganic ion-exchange materials. In layered mixed oxides[20,21] and M(IV)phosphates,[22] for example, the spacing between two layers changes with the intercalated ion. The rigid three-dimensional open frameworks of zeolites, however, tend to be less affected by ion exchange. They

have well-defined channels and cages that permit only ions up to a certain size to enter. For example, the zeolite analcime[23,24] excludes Cs$^+$ ions, and zeolite A excludes large tetraalkylammonium ions from its sodalite cages.[25] Nevertheless, most zeolites can accommodate a considerable number of uni- and/or divalent cations in their larger cavities. In equilibrium experiments, in which two different cations are present, a specific zeolite often shows a preference for certain types or sizes of ions[26,27]. The selectivity depends mainly on the size of the pore opening, the electrostatic interactions between the anionic framework and the cationic guest and the concentration of the ions in solution. As selectivity becomes more specific, the ability of the framework to adapt can also play a significant role in zeolitic three-dimensional structures. It was shown quite recently that the Cs$^+$-exchange mechanism in a tunnel-type titanium silicate[28], which selectively captures Cs$^+$ and Sr^{2+} from highly concentrated NaNO$_3$ solutions[29], is mediated by conformational changes in the framework[30-32]. These results suggest that flexible metal organic frameworks might be predestined to be selective ion exchangers. However, as most MOFs have neutral frameworks, the incorporation of ionic guests in this type of material has only been investigated in a limited number of cases.[33-37]

In order to examine this issue more carefully, a combined study was undertaken of the ion-exchange properties and the framework flexibility of the recently discovered NaLa[(PO$_3$H)$_2$CH-C$_6$H$_4$-CH(PO$_3$H)$_2$]·4H$_2$O, **NaLa(H$_4$L)**, a lanthanum tetrakisphosphonate with a three-dimensional coordination network. Its anionic framework is constructed from La^{3+} ions and (PO$_3$H)$_2$CH-C$_6$H$_4$-CH(PO$_3$H)$_2$ **(H$_4$L^{4-})**, a ligand with two bisphosphonate groups connected via a rigid benzene linker. The La^{3+} ions are bridged by the phosphonate groups of the **H$_4$L^{4-}** ligand to form -La-O-P-O-La- chains, and these chains are linked via the organic spacer to form a three-dimensional anionic open framework. The framework features rhombic channels, which are defined by the chains located at the corner of each

rhombus, and are filled with Na$^+$ ions and water molecules as guests (Figure 5.1 - 1).
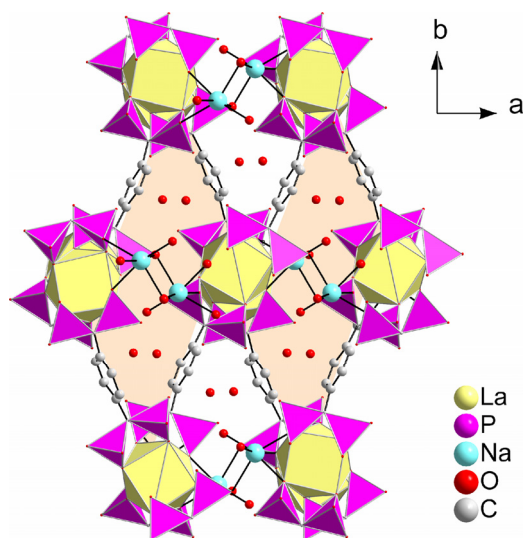
Figure 5.1 - 1: Projection of the **NaLa(H₄L)** structure showing the rhombus (shaded) formed by the connection of phosphonate bridged chains of La^{3+} ions (perpendicular to the page) and the H₄L^{4-} ligand. The channels are filled with Na$^+$ ions and H₂O molecules.

5.2 Experimental Section

Metal salts were purchased from Aldrich in the purity degrees extra pure, p.a., puriss. or had a purity of more than 99.5 %. NaOH was purchased as a 1 M volumetric standard solution. Bidistilled water from a Millipore system (Milli-Q Academic A10) was used throughout. The molecular building block 1, 4-phenylen bis(methylidyne)tetrakis(phosphonic acid), **H₈L**, was prepared as described in chapter 3 and provided as a 0.5 M aqueous solution.

Synthesis of NaLa[(PO₃H)₂CH-C₆H₄-CH(PO₃H)₂]·4H₂O, NaLa(H₄L). 7.94 mL (830 mmol) of water and 4.00 mL of 1.0 M NaOH were added to 2.00 mL of a 0.5 M aqueous solution of **H₈L**. Stirring was started and 1 mL of 1 M La(NO₃)₃ was added. The gel with the batch composition La(NO₃)₃ : H₈L : 4 NaOH : 830 H₂O was stirred for 30 minutes and then heated under hydrothermal conditions

for 36 h at 100°C. The precipitated crystals were separated from the reaction mixture by filtration under reduced pressure, washed with water and dried at room temperature. The pH of the reaction mixture was 1.0 before and 1.5 after the heating process. (Yield: 630 mg, 0.96 mmol, 96 %). Chemical analysis by EDX yielded La : Na : P = 1.1 : 1.3 : 4.0, and by ICP-OES La : Na : P = 1.0 : 1.1 : 4.0. Dehydration of **NaLa(H$_4$L)** was effected by heating the as-synthesized form for 2 h at 180 °C in air. The dehydrated form NaLa[(PO$_3$H)$_2$CH-C$_6$H$_4$-CH(PO$_3$H)$_2$], **NaLa(H$_4$L)$_{dehyd.}$,** is stable if stored under vacuum, argon or nitrogen, but exposure to moist air results in rapid re-hydration.

Ion-exchange. For the ion-exchange experiments, saturated aqueous solutions of LiCl, KCl, RbCl, CsCl, MgCl$_2$, CaCl$_2$, Sr(NO$_3$)$_2$, BaCl$_2$, NiCl$_2$, CuCl$_2$, ZnCl$_2$, MnCl$_2$, Fe(NO$_3$)$_3$ were prepared. Ion-exchange was performed by stirring 100 mg of **NaLa(H$_4$L)** in 10 mL of the salt solution for three days at room temperature. Then the solid was separated from the solution by filtration under reduced pressure, briefly washed with water and dried at room temperature.

Powder Diffraction Data Collection. Several different X-ray powder diffractometers were used for the characterization of these materials. A Stoe Stadi P high-throughput powder diffractometer[38] (CuKα radiation, Ge monochromator, transmission geometry) equipped with an image plate detector system and an *xy* sample stage was used for initial identification. A Bruker D8 Discover diffractometer (CuKα$_1$, θ-θ reflection geometry, Vantec detector) was used to record the patterns of the alkali-ion-exchanged samples. For these measurements, the samples of **KLa(H$_4$L)** were first exposed to bidistilled water to keep the K$^+$ guest ions hydrated. A Stoe Stadi P diffractometer (MoKα radiation, Ge monochromator, transmission geometry) equipped with a high temperature cell was used for the *in situ* temperature-dependent measurements of **NaLa(H$_4$L)**. For these measurements, X-ray powder diffraction patterns were recorded from 25 °C to 700 °C in steps of 25 °C, at 800°C, and after cooling

down to 100°C. The sample was heated at each target temperature for 20 minutes before the diffraction measurement was started. Finally, a Stoe Stadi P diffractometer (CuKα$_1$, transmission mode, linear position-sensitive detector) was used to record the pattern of **NaLa(H$_4$L)$_{dehyd}$** (sealed in a 0.3mm glass capillary) for structure analysis.

Further characterization methods. All of these characterization methods were applied on samples dried in air for two weeks to assure that the samples had reached their equilibrium in the hydration/dehydration process. Morphology and stoichiometry were studied with a Joel JSM 6500 F scanning electron microscope equipped with an EDX detector. Each sample was applied to an adhesive carbon film on the sample holder and coated with carbon using a BAL-TEC MED 020 Coating System. Thermogravimetric analyses (TGA) were performed on a Netzsch STA 449 C TG/DSC (heating rate of 10 K/min in a ~25 mL/ min stream of synthetic air). The chemical compositions of the alkali-ion-exchanged samples were determined by inductively coupled plasma optical emission spectroscopy (ICP-OES, VARIAN VISTA) and compared with the EDX analysis results.

Unit Cell Determination. The powder diffraction patterns of **NaLa(H$_4$L)$_{dehyd}$** and the alkali ion-exchanged samples **LiLa(H$_4$L)**, humidified **KLa(H$_4$L)** and **RbLa(H$_4$L)** were indexed using the Visser algorithm implemented in the program WinXPOW[39]. The results of a subsequent refinement of the lattice parameters in P2$_1$/n are given in Table 5.2 − 1. Lattice parameters of the as-synthesized NaLa(H4L) were obtained from a single-crystal structure analysis described in chapter 4.

Table 5.2 − 1: Lattice parameters of NaLa(H$_4$L)$_{dehyd}$, LiLa(H$_4$L)·4H$_2$O, NaLa(H$_4$L)·4H$_2$O, KLa(H$_4$L)(2+x)·H$_2$O, and RbLa(H$_4$L)·2H$_2$O.

	NaLa(H$_4$L)$_{dehyd}$	LiLa(H$_4$L)	NaLa(H$_4$L)	KLa(H$_4$L)	RbLa(H$_4$L)
cryst. system	monoclinic	monoclinic	monoclinic	monoclinic	monoclinic
space group	$P2_1/n$	$P2_1/n$	$P2_1/n$	$P2_1/n$	$P2_1/n$
a (Å)	7.165(2)	8.760(2)	8.975	9.162(5)	9.291(3)
b (Å)	22.758(5)	22.09(1)	21.691	21.88(1)	21.717(7)
c (Å)	10.147(2)	10.146(3)	10.186	10.284(9)	10.324(7)
β (°)	100.98(2)	104.40(2)	105.56	106.49(6)	109.03(4)
V (Å^3)	1624(4)	1902(1)	1910.2	1977(2)	1969(1)
FOM (F30)*	38.7	20.1	-	18.3	16.7
020 (°2θ)	7.769	8.007	8.145	8.052	8.107
110 (°2θ)	11.802	11.158	11.006	10.823	10.838

* Lattice parameters of NaLa(H$_4$L) were obtained from a single-crystal structure analysis described elsewhere[40]. FOM = figure of merit

5.3 Results and Discussion

Ion exchange. The Na$^+$ ions in the channels of **NaLa(H$_4$L)** are exchangeable. Ion exchange reactions were performed with monovalent ions (Li$^+$, K$^+$, Rb$^+$ and Cs$^+$), divalent ions (Mg^{2+}, Ca^{2+}, Sr^{2+}, Ba^{2+}, Ni^{2+}, Cu^{2+}, Zn^{2+}, Mn^{2+}) and the trivalent Fe^{3+} ion. The saturated solutions of FeCl$_3$ (pH = 0) and ZnCl$_2$ (pH = 2) proved to be too acidic, and the **NaLa(H$_4$L)** decomposed. In all other cases, the XRD patterns and SEM images showed that the structure and morphology remained intact during the treatment (Figure 8.2.4 - 1). Strikingly, EDX analysis and ICP-OES revealed that ion exchange was selective towards monovalent ions (Table 2). Na$^+$ (r = 1.02 Å)[41] could be replaced almost completely by Li$^+$ (r = 0.76 Å)[41], K$^+$ (r = 1.38 Å)[41] and Rb$^+$ (r = 1.52 Å)[41]. However, the Cs$^+$ ion, with an ionic

Table 5.3 − 1: Chemical Composition of ion-exchanged samples as determined by ICP-OES

Sample	Na/P	M/P	La/P	P
NaLa(H$_4$L)	1.0	-	1.1	4.0
Na$_{(1-x)}$Li$_x$La(H$_4$L)	0.1	1.4	1.1	4.0
Na$_{(1-x)}$K$_x$La(H$_4$L)	0.1	1.2	1.1	4.0
Na$_{(1-x)}$Rb$_x$La(H$_4$L)	0.1	1.1	1.1	4.0
Na$_{(1-x)}$Cs$_x$La(H$_4$L)	0.9	*	1.1	4.0

*Cesium could not be detected in ICP-OES analysis. EDX analysis confirms a very low Cs content of the sample (Na$_{0.9}$Cs$_{0.2}$La$_{1.1}$(H$_4$L)).

radius of 1.67 Å,[41] appears to be too large. Only a slight decrease in the sodium content was observed in that sample. In contrast, samples that were treated with solutions of divalent ions showed no decrease in the sodium content (Table 8.2.5 - 1), although they are smaller in size than most of the monovalent ions. The small amounts of divalent ions detected in the samples can be attributed to adsorption on the surface of the crystals. The discrimination for monovalent ions is remarkable, as absolute selectivity is rare in inorganic open-framework ion-exchange materials, and is usually related to size rather than charge. To the best of our knowledge, no open framework that accepts monovalent ions, but totally excludes more highly charged ions has ever been reported. A better understanding of this enhanced selectivity could be gained by studying the relationships between the guest ions, the water molecules and the framework of **NaLa(H$_4$L)**.

Hydration and dehydration. The as-synthesized form of **NaLa(H$_4$L)**, with the chemical composition NaLa[(PO$_3$H)$_2$CH-C$_6$H$_4$-CH(PO$_3$H)$_2$]·4H$_2$O has four water molecules per unit cell. Heating the compound to 100 °C leads to an endothermal mass loss of 11% (Figure 5.3 - 1). This corresponds exactly to the nominal mass fraction of water in the crystal. After the water loss, a plateau that is stable up to 375 °C is reached in the TGA diagram, indicating the presence of

a stable dehydrated phase **NaLa(H$_4$L)$_{dehyd.}$**. Temperature-dependent XRD measurements support this conclusion (Figure 5.3 - 2). The X-ray diffraction pattern of **NaLa(H$_4$L)** remains unchanged up to 100 °C, and then a phase change occurs. The second phase is stable up to 375 °C, and between 400 and 500 °C, an amorphous product is formed. At 525 °C, oxidation leads to the formation of dense NaLa(PO$_3$)$_4$. Although the formation of the dense high-temperature phase is an irreversible process, the first phase transformation is reversible. The water is removed upon heating, and **NaLa(H$_4$L)$_{dehyd}$** is formed. Cooling **NaLa(H$_4$L)$_{dehyd}$** to room temperature in the presence of water (e.g., from moisture in the air) allows it to transform back to the original hydrated form **NaLa(H$_4$L)**. If no water is present in the atmosphere, **NaLa(H$_4$L)$_{dehyd}$** is stable at room temperature. During this transformation, the lanthanum phosphonate framework of **NaLa(H$_4$L)** remains intact, but the unit cell changes significantly. A comparison of the powder patterns of **NaLa(H$_4$L)** and **NaLa(H$_4$L)$_{dehyd}$** shows that they are similar, but that the peaks are shifted substantially in 2θ (Figure 5.3 - 3). The most obvious changes are the shifts of the 020 reflection to a lower 2θ value (corresponding to a stretching of the *b*-axis from 21.691 Å to 22.758(5) Å), and of the 011 reflection to a much higher value (corresponding to a shortening of the *a*-axis from 8.975 Å to 7.165(2) Å). Refinement of the lattice parameters shows that the cell volume decreases by 15 % upon dehydration, from 1910 to 1624 Å^3 (Table 5.2 - 1). The change in the unit cell volume reflects the shrinking of the channels upon dehydration that was found in the structure refinement.
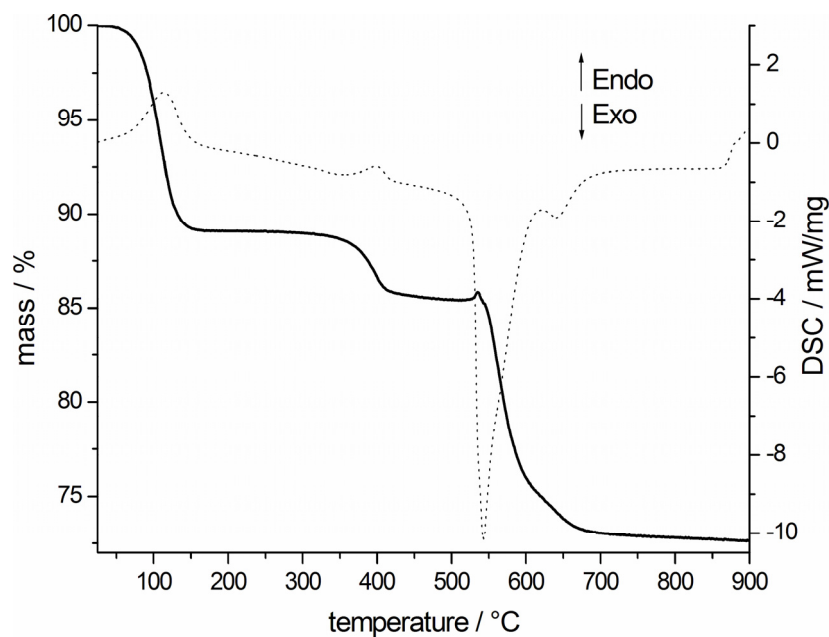
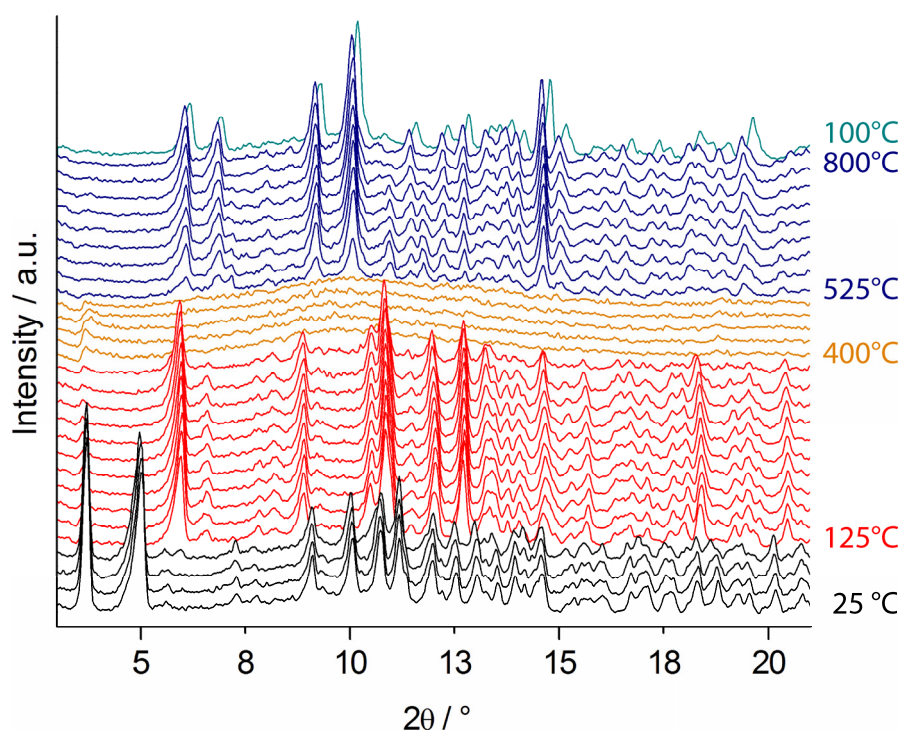**Figure 5.3 - 1**: Thermogravimetric analysis and DSC of **NaLa(H$_4$L)**.

Figure 5.3 - 2: X-ray powder diffraction patterns (MoKα, in air) of **NaLa(H$_4$L)** (black) as a function of temperature. It transforms first to **NaLa(H$_4$L)$_{dehyd.}$** (red), and then, via an amorphous region (yellow), to dense NaLa(PO$_3$)$_4$ (blue). The first low-angle peak for **NaLa(H$_4$L)$_{dehyd}$** was not recorded, because it lies outside the 2θ window of the furnace.
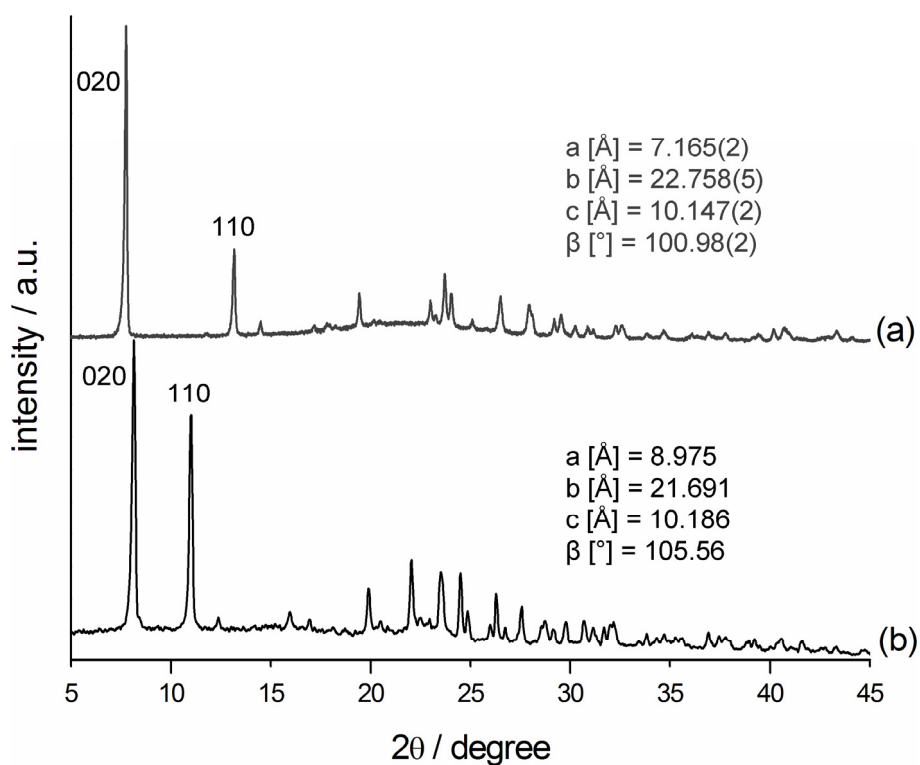
Figure 5.3 - 3: X-Ray powder diffraction patterns (CuKα₁) and the corresponding lattice parameters of (a) **NaLa(H₄L)dehyd** under vacuum, and (b) **NaLa(H₄L)** in air.
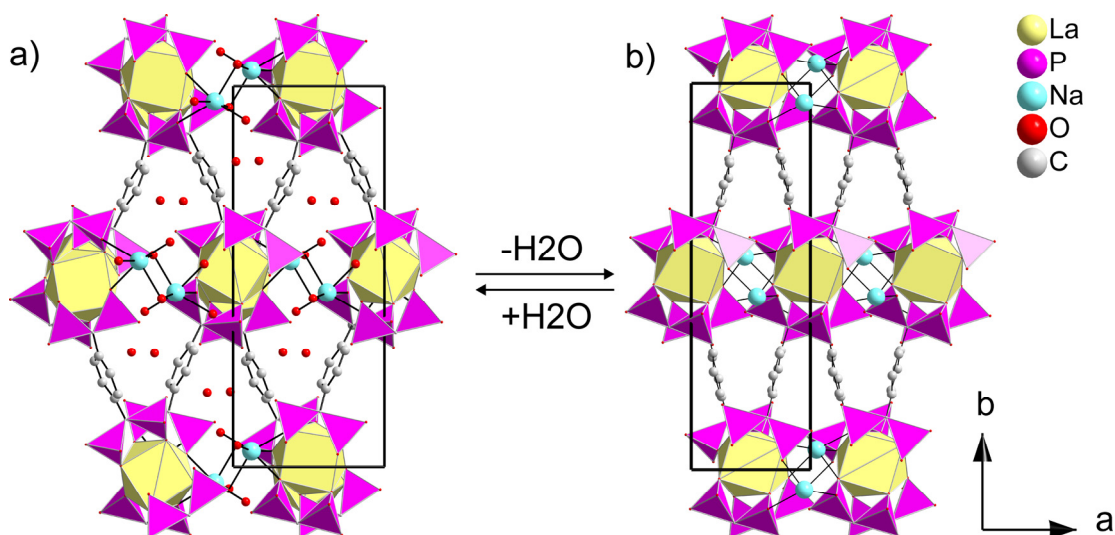
Figure 5.3 - 4: Contraction and expansion of the channels in **NaLa(H₄L)** during the dehydration/hydration process: [001] projection of the crystal structure of (a) **NaLa(H₄L)**, and (b) **NaLa(H₄L)dehyd** . Hydrogen atoms have been omitted for clarity.

A complete model of the structure of **NaLa(H$_4$L)$_{dehyd}$** could be derived from the Rietveld refinement (Figure 5.3 - 4). The fractional coordinates of the La, Na, P, C and phosphonate O atoms from the single-crystal structure analysis of **NaLa(H$_4$L)** were used to generate a structural model for **NaLa(H$_4$L)$_{dehyd}$**. The two free waters and the two coordinated to Na were not included, so it was assumed that the Na+ ions would adopt a tetrahedral geometry. Restraints were imposed on the bond distances (C-C, C-P, P-O, La-O, Na-O) and angles (tetrahedral P, trigonal planar C, tetrahedral Na), and the geometry was optimized for the smaller unit cell. The powder diffraction pattern of this idealized structure appeared to match the measured one quite well, so it was used as a starting point for Rietveld refinement using the XRS-82 suite of programs[42]. It soon became apparent that the angle restraints on the Na position were hindering the refinement, so they were removed. This resulted in a significant improvement in the R-values and a new coordination environment for the Na$^+$ ions. Further refinement of the atomic positions and displacement factors converged with RF = 0.056 and Rwp = 0.086 (Rexp = 0.075). Positions for the H atoms bonded to C atoms were calculated and added to the final model, but were not refined. The positions of the H atoms of the terminal P-OH groups could not be calculated, so the occupancy parameters for these O atoms were increased to 1.125 to approximate the extra electron of the H atom. All displacement factors were refined isotropically, and those for similar atoms were constrained to be equal to keep the number of parameters to a minimum. Neutral scattering factors were used for all atoms. The final atomic parameters for this model are provided as a CIF file in the supporting information. Details of the refinement are given in Table 8.2.1 − 1, and selected bond distances in Table 8.2.2 − 1/2/3. The fit of the calculated powder diffraction pattern to the measured data is shown in Figure 8.2.1 − 1.

The asymmetric unit of **NaLa(H₄L)ₐₑₕᵧₐ** contains 26 non-hydrogen atoms (Figure 5.3 - 5a). The crystal structure is composed of $[(PO_3H)_2CH\text{-}C_6H_4\text{-}CH(PO_3H)_2]_4$-, La^{3+}, and Na^+ ions. From the P-O distances it is apparent that all four phosphonic acid groups are singly deprotonated (Table 8.2.2 - 1). As in **NaLa(H₄L)**,[40] the La^{3+} ions are each coordinated to 8 phosphonate oxygens of four **(H₄L)⁴⁻** ligands. The La-O distances range from 2.47(2) Å to 2.70(2) Å (Table 8.2.2 - 2). These are slightly longer than those in **NaLa(H₄L)**, but are still comparable to those reported for $LaPO_4$.[43] As in **NaLa(H₄L)**, lanthanum is coordinated only to bisphosphonate oxygen atoms (Figures 6b). Each phosphonate group bridges between neighboring lanthanum ions in such a way that an -La-O-P-O-La- chain is built along c (Figure 5.3 - 5c). The coordinating oxygen atoms around lanthanum form a distorted square antiprism with the top square decorated with the P1 and P2 and the bottom square with the P3 and P4 phosphonate groups. The structure is completed with the benzene spacer connecting the bisphosphonate groups (Figure 5.3 - 5d and 5f) to form a three-dimensional open framework with the -La-O-P-O-La- chains located at the corners of a rhombus (Figure 5.3 - 5d). The rhombic channels along c that are observerd in **NaLa(H₄L)** are contracted in **NaLa(H₄L)ₐₑₕᵧₐ**. The main openings in this contracted form are small apertures between terminal P-OH groups (O···O: 3.60 Å) and between the benzene linkers (C···C: 4.52 Å) that can be observed along the [101] direction (Figure 8.2.3 - 1). Sodium ions reside as guests in the pores, where each is coordinated to five phosphonate oxygens in a square pyramidal arrangement (Figure 5.3 - 5e) with Na-O distances ranging from 2.30(2) Å to 2.73(2) Å (Table 8.2.2 - 3)[44]. The Na^+ ion coordinates to three phosphonate oxygens bridging to one La^{3+} ion (O3, O5 and O11) and to two others (O12 and O6) bridging to a second La^{3+} ion in an adjacent -La-O-P-O-La- chain. Thus, the Na^+ ions are located opposite triangular faces of the lanthanum polyhedron on both sides of the -La-O-P-O-La- chain (Figure 5.3 - 5f).
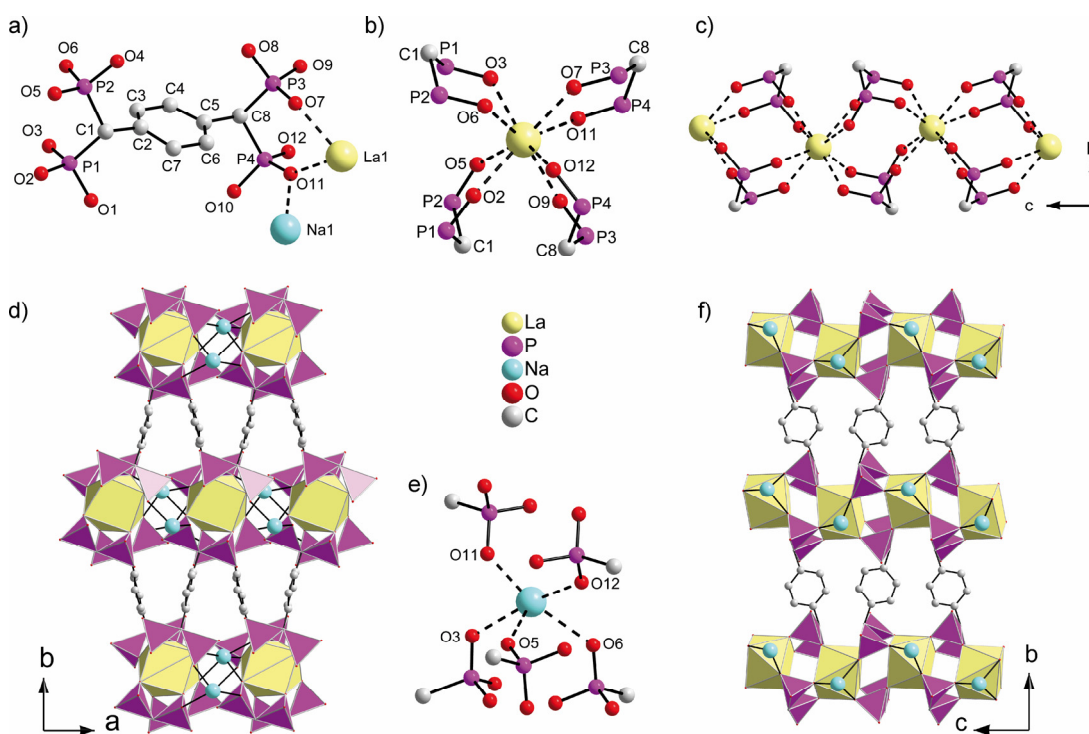
Figure 5.3 - 5: Structure of LaNa[(PO$_3$H)$_2$CH-C$_6$H$_4$-CH(PO$_3$H)$_2$], **NaLa(H$_4$L)$_{dehyd}$**. (Hydrogen atoms are omitted for clarity): (a) asymmetric unit, (b) coordination of La^{3+}, (c) phosphonate-bridged chain of lanthanum running along *c*, (d) projection down [001] showing the rhombus formed by the La^{3+} ions and the biphosphonate linkers, (e) coordination of Na$^+$, (f) projection of down [100] showing the decoration of the -La-O-P-O-La- chains with sodium ions.
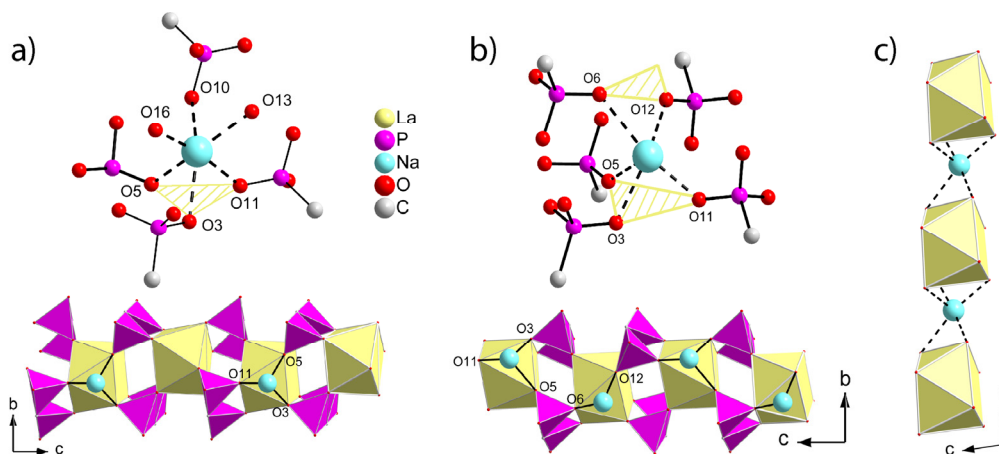
Figure 5.3 - 6: Coordination sphere of sodium and its location in the metal phosphonate chain in (a) **NaLa(H$_4$L)**, and (b) **NaLa(H$_4$L)$_{dehyd}$**, and (c) the -La-O-Na-O-La- chain along *a* in **NaLa(H$_4$L)$_{dehyd}$**.

A comparison of the structure of **NaLa(H₄L)ₐₑₕᵧd** with that of **NaLa(H₄L)** gives detailed insights into the mechanism of the channel shrinkage and the role of the guest ion in this process. Of the four water molecules in the channels of **NaLa(H₄L)**, two are free and two are coordinated to sodium (Na-O13, 2.402(2) Å and Na−O16, 2.215(2) Å). In this hydrated expanded form, each Na^+ ion is also coordinated to three phosphonate O atoms (O3, O5 and O11 with Na-O distances of 2.531(2)Å, 2.353(2)Å and 2.296(2) Å), which bridge to a single La^{3+} ion. Sodium ions decorate alternating sides of the lanthanide phosphonate chains running along the [001] direction (Figure 5.3 - 4a, Figure 5.3 - 6a). The octahedral coordination sphere of Na^+ is completed with a rather weak bond (Na-O10 = 2.665(2) Å) to a protonated P-OH group of a neighboring lanthanum phosphonate chain. Upon dehydration, all of the water molecules leave the structure, and the Na^+ ion compensates for the loss of two of its ligands by forming two new bonds with phosphonate oxygens (O6 and O12) in the adjacent -La-O-P-O-La- chain (Figure 5.3 − 4b, Figure 5.3 − 6b). In this process, its sacrifices the weak Na-O10 bond, and its coordination becomes square pyramidal. As a result, an -La-O-Na-O-La- chain is generated along *a* (Figure 5.3 − 6c, Figure 8.2.3 - 2). The formation of this second chain requires a shortening of *a* with a concomitant shrinking of the channels. The connectivity of the lanthanum-bisphosphonate framework remains intact, but the square antiprism coordination polyhedron of the lanthanum ions distorts by twisting the two squares with respect to one another to accommodate the effects of the dehydration (Figure 8.2.3 - 3). This results in a decrease in the acute angle of the rhombus from 41.1° in **NaLa(H₄L)** to 26.4 ° in **NaLa(H₄L)ₐₑₕᵧd**.

The -La-O-Na-O-La- chain formation can be considered to be the driving force for the channel shrinkage, and is therefore the key to understanding the flexibility of the framework. An equilibrium exists between the expanded (hydrated) and the contracted form (Figure 5.3 - 4). In this equilibrium, the

hydration energy of the guest ion competes with the lattice energy that is gained by chain formation. In the as-prepared sodium compound (in air and at room temperature), the equilibrium favors the expanded form.

MLa(H$_4$L)	x H$_2$O	expanded		contracted
LiLa(H$_4$L)	4 H$_2$O	◇	⇌	◇
NaLa(H$_4$L)	4 H$_2$O	◇	⇌	◇
KLa(H$_4$L)	2 H$_2$O	◇	⇌	◇
RbLa(H$_4$L)	2 H$_2$O	◇	⇌	◇

Figure 5.3 - 7: Water content and equilibrium between the expanded and contracted forms of MLa(H$_4$L) in air and at room temperature.

The exchanged forms **LiLa(H$_4$L)** and **KLa(H$_4$L)** can also exist in both forms (Figure 5.3 - 7). TGA analysis shows that **LiLa(H$_4$L)** contains 4 equivalents of water (Figure 8.2.6 - 1), and like **NaLa(H$_4$L)**, is stable in the expanded form at room temperature. In **KLa(H$_4$L)** and **RbLa(H$_4$L)**, the mass losses upon heating to 100°C correspond to only two water molecules per unit cell (Figure 8.2.6 - 1c,d). The XRD pattern of **KLa(H$_4$L)** shows a slow transformation when the sample is dried in air (Figure 5.3 - 8), and the directions of the shifts of the 020 and 110 reflections correspond to those observed for **NaLa(H$_4$L)** upon dehydration. It can be concluded that in the case of **KLa(H$_4$L)**, the equilibrium favors the contracted form, but that the energy barrier between the two forms is very low. Hydrating the sample with a drop of water causes an immediate shift back to the expanded form. Under the same conditions, only one XRD pattern is observed for **RbLa(H$_4$L)** (Figure 8.2.4 - 1). The lower water content and the positions of the reflections in the XRD pattern are indicative of a contracted form. All attempts to obtain an expanded form by hydrating the sample were unsuccessful. It appears that **RbLa(H$_4$L)** has a strong preference for a contracted form. This can be explained by the fact that Rb$^+$ has a lower enthalpy

of hydration than do the smaller alkali metal ions and that the larger Rb$^+$ ion is well-accommodated in a more contracted coordination environment.

The ionic guests play a crucial role in the chain-forming/breaking mechanism that determines the flexibility of the framework. Different monovalent ions with different ionic radii and enthalpies of hydration influence the equilibrium between the expanded and the contracted forms differently. Although they are exchangeable, the monovalent ions are located at a specific site in the structure, where they contribute significantly to its stabilization. The strong interaction between the guest and the framework becomes even more apparent when the positions of the reflections in the diffraction patterns of the exchanged samples are compared. It can be seen that the framework not only changes by forming a -La-O-M(I)-O-La- chain, but that it also adapts to the size of the incorporated ion (Figure 5.3 - 9). In the pattern of the Li$^+$ exchanged samples, the 110 reflection is shifted to a 2θ value higher than that of **NaLa(H$_4$L)**. This corresponds to a contraction of the channels and is therefore in good agreement with the fact that lithium is smaller than sodium. The pattern of the K$^+$-exchanged sample shows a shift of the 110 reflection in the opposite direction, as would be expected for the expansion needed to accommodate the larger cation. As **RbLa(H$_4$L)** is present in a contracted form, the shifts are reversed. The 2θ value of the 100 reflection is larger than that for **KLa(H$_4$L)**, indicating a decrease in the channel size. As Cs$^+$ does not enter the channels, the sample treated with cesium does not show any change in the powder diffraction pattern from that of the Na-form. The adaptation of the framework to the size of the guest ion is reflected in the unit cell volumes (Figure 5.3 − 10). The changes are smaller than that observed for **NaLa(H$_4$L)** upon dehydration, but still noticeable, and range from 1902 Å^3 for **LiLa(H$_4$L)** to 1977 Å^3 for **KLa(H$_4$L).** Comparison of the five materials discussed in this study shows that a change in the unit cell volume of 22 % is observed in going from **NaLa(H$_4$L)$_{dehyd}$** to **KLa(H$_4$L)**.

126
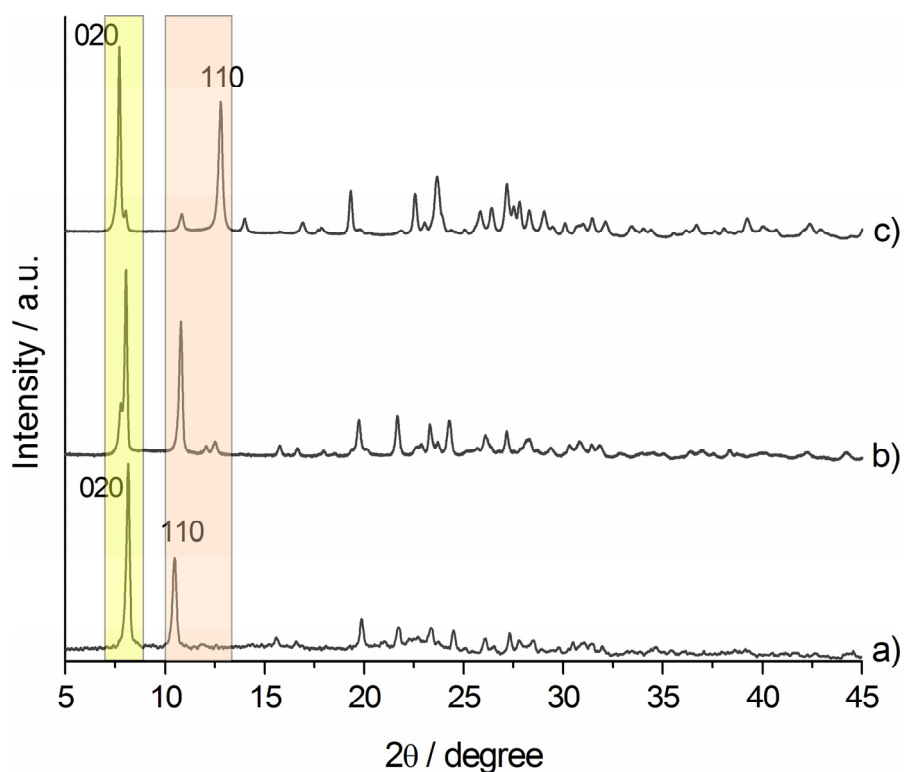
Figure 5.3 - 8: XRD patterns of KLa(H$_4$L) (a) immediately after hydration, (b) after 4 hours, and (c) after one week, show that the structure slowly shifts from the expanded to the contracted form, while it is drying in air at room temperature. Yellow region: 020 shift; Red region: 110 shift.
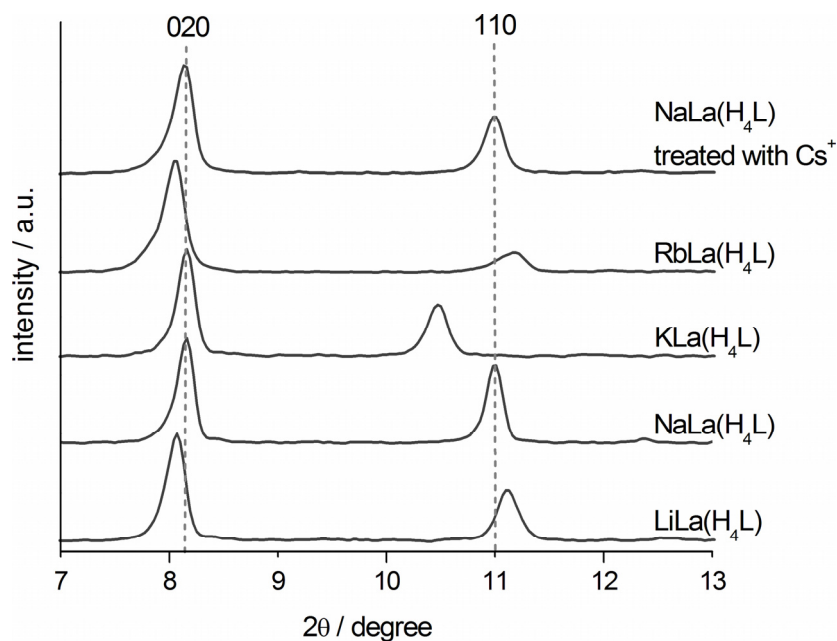
Figure 5.3 − 9: Shifts of the 020 and the 110 reflections in the powder patterns of **LiLa(H$_4$L)**, **NaLa(H$_4$L)**, **KLa(H$_4$L)**, **RbLa(H$_4$L)**, and of **NaLa(H$_4$L)** after the treatment with Cs$^+$.
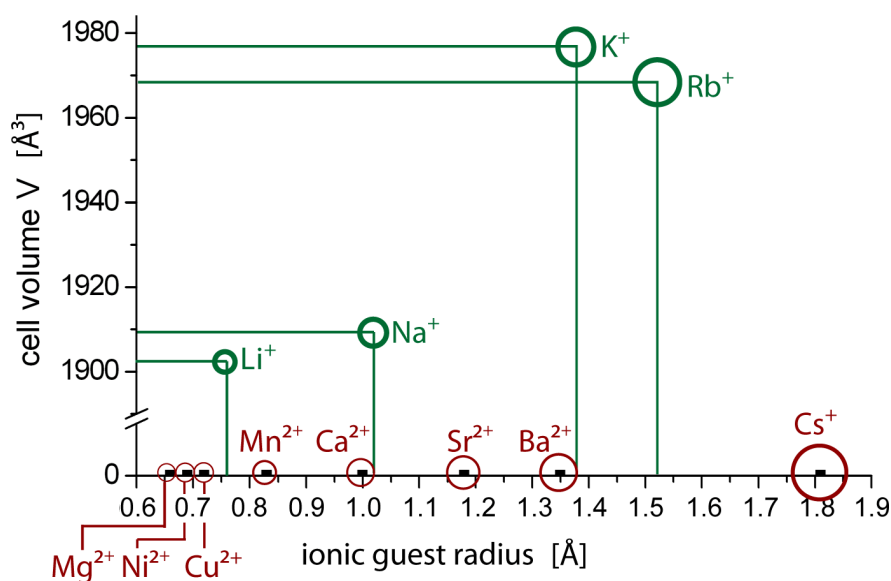
Figure 5.3 − 10: Radii of the ions, which are uptaken (green) or not uptaken (red) by the framework of **MLa(H$_4$L)** and correlation with the respective cell volume in its highest observed hydrated state: **LiLa(H$_4$L)·4H$_2$O** dried in air, **NaLa(H$_4$L)·4H$_2$O**, dried in air; **KLa(H$_4$L)·(2+x)H$_2$O**, humidified; **RbLa(H$_4$L)·2H$_2$O** humidified or dried in air.

From these observations it can be deduced that the ionic guests are more than charge equalizers and space fillers. The strong response of the framework to the ionic guest explains the enhanced selectivity of **NaLa(H$_4$L)** for monovalent cations. To maintain charge balance, divalent cations could only occupy every second guest site, and this might reduce the stability of the framework and make its incorporation difficult. **NaLa(H$_4$L)** has been shown to be an ion exchanger, where the effect of framework adaptation on ion-exchange selectivity, which plays only a minor role in zeolites, is fundamental.

5.4 Conclusion

The sodium lanthanide tetrakisphosphonate NaLa[(PO$_3$H)$_2$CH-C$_6$H$_4$-CH(PO$_3$H)$_2$]·4H$_2$O, **NaLa(H$_4$L)** features a flexible open-framework anionic host with an extraordinary charge selectivity for its guest cations. In aqueous media, the Na$^+$ ions hosted in the channels of the structure can be exchanged with

other monovalent ions with ionic radii ranging from 0.76 Å (Li$^+$) to 1.52 Å (Rb$^+$), while divalent ions in the same size range are rejected. The water molecules in the channels can be removed by heating, and this causes a shrinking of the channels and a decrease in the cell volume of 15 %. Upon dehydration, the Na$^+$ ions compensate for the loss of coordinated water by forming new bonds with phosphonate oxygens, and in the process generate an -La-O-Na-O-La- chain perpendicular to the lanthanum phosphonate chain of the original coordination network. The formation of this second chain stabilizes the framework and can be considered to be the driving force for the structural transformation. This dehydration process is fully reversible. The ion-exchanged compounds **LiLa(H$_4$L)** and **KLa(H$_4$L)** can exist in both the expanded and the contracted forms, whereas **RbLa(H$_4$L)** is found only in a contracted form. The ionic radius and the enthalpy of hydration of the guest cation were seen to influence the equilibrium between the two forms. The framework adapts to the water content or the guest cation, and a volume change of 22% was observed in going from the dehydrated contracted Na$^+$ form to the expanded hydrated K$^+$ form. The key role played by the ionic guest in the chain-forming mechanism and the adaptation of the framework to the size of the cation both show the relevance of the exchangeable cations to framework stabilization and charge balance. The monovalent guest cations are located at specific sites in the structure, where they can satisfy their coordination requirements. Divalent ions could occupy only half of these sites, and this might explain the unusual selectivity of this material for monovalent cations. The type of framework flexibility observed for the lanthanide tetrakisphosphonate **NaLa(H$_4$L)** suggests new opportunities for the design of chemically selective sensors and selective ion-exchange materials from MOF materials with flexible anionic frameworks.

5.5 References

(1)   Kitagawa, S.; Kondo, M. 1998, *71*, 1739.

(2)   Serre, C.; Millange, F.; Thouvenot, C.; Nogues, M.; Marsolier, G.; Loueer, D.; Ferey, G. *J. Am. Chem. Soc.* 2002, *124*, 13519.

(3)   Serre, C.; Mellot-Draznieks, C.; Surble, S.; Audebrand, N.; Filinchuk, Y.; Ferey, G. *Science* 2007, *315*, 1828.

(4)   Fletcher, A. J.; Cussen, E. J.; Prior, T. J.; Rosseinsky, M. J.; Kepert, C. J.; Thomas, K. M. *J. Am. Chem. Soc.* 2001, *123*, 10001.

(5)   Barthelet, K.; Marrot, J.; Riou, D.; Ferey, G. 2002, *41*, 281.

(6)   R. Kitaura, K. S., G. Akiyama, S. Kitagawa, *Angew. Chem., Int. Ed.* 2003, *42*, 428.

(7)   Y. Kubota, R. Matsuda, R. Kitaura, S. Kitagawa, T. C. Kobayashi, *Angew. Chem., Int. Ed.* 2006, *45*, 4932.

(8)   Zhao, X.; Xiao, B.; Fletcher, A. J.; Thomas, K. M.; Bradshaw, D.; Rosseinsky, M. J. *Science* 2004, *306*, 1012.

(9)   Takamizawa, S.; Saito, T.; Akatsuka, T.; Nakata, E.-i. *Inorg. Chem.* 2005, *44*, 1421.

(10)   Li, D.; Kaneko, K. *Chem. Phys. Lett.* 2001, *335*, 50.

(11)   Fletcher, A. J.; Thomas, K. M.; Rosseinsky, M. J. *J. Solid State Chem.* 2005, *178*, 2491.

(12)   Uemura, K.; Matsuda, R.; Kitagawa, S. 2005, *178*, 2420.

(13)   Millange, F.; Serre, C.; Ferey, G. *Chem. Commun.* 2002, 822.

(14)   Whitfield, T. R.; Wang, X.; Liu, L.; Jacobson, A. J. *Solid State Sci.* 2005, *7*, 1096.

(15)   C. Serre, S. Surblé, G. Férey, *Angew. Chem., Int. Ed.n* 2004, *43*, 6285.

(16)   Mellot-Draznieks, C.; Serre, C.; Surble, S.; Audebrand, N.; Ferey, G. *J. Am. Chem.Soc.* 2005, *127*, 16273.

(17)   Loiseau, T.; Serre, C.; Huguenard, C.; Fink, G.; Taulelle, F.; Henry, M.; Bataille, T.; Ferey, G. *Chem. Eur. J.* 2004, *10*, 1373.

(18)   Bourrelly, S.; Llewellyn, P. L.; Serre, C.; Millange, F.; Loiseau, T.; Ferey, G. *J. Am. Chem. Soc.* 2005, *127*, 13519.

(19)   Llewellyn, P. L.; Bourrrelly, S.; Serre, C.; Filinchuk, Y.; Ferey, G. *Angew. Chem., Int. Ed.* 2006, *45*, 7751.

(20)   England, W. A.; Goodenough, J. B.; Wiseman, P. J. *J. Solid State Chem.* 1983, *49*, 289.

(21) England, W. A.; Birkett, J. E.; Goodenough, J. B.; Wiseman, P. J. *J. Solid State Chem.* 1983, *49*, 300.

(22) Clearfield, A. *Chem. Rev.* 1988, *88*, 125.

(23) Barrer, R. M.; Sammon, D. C. *J. Chem. Soc.* 1956, 675.

(24) Barrer, R. M.; Hinds, L. *J. Chem. Soc.* 1953, 1879.

(25) Barrer, R. M.; Meier, W. M. *Trans. Faraday Soc.* 1958, *54*, 1074.

(26) Sherry, H. S. *Handb. Zeolite Sci. Technol.* 2003, 1007.

(27) Kuronen, M.; Harjula, R.; Jernstrom, J.; Vestenius, M.; Lehto, J. *Phys. Chem. Chem. Phys.* 2000, *2*, 2655.

(28) Clearfield, A. *Solid State Sci.* 2001, *3*, 103.

(29) Zheng, Z.; Gu, D.; Anthony, R. G.; Klavetter, E. *Ind. Eng. Chem. Res.* 1995, *34*, 2142.

(30) Celestian, A. J.; Clearfield, A. *J. Mater. Chem.* 2007, *17*, 4839.

(31) Celestian, A. J.; Kubicki, J. D.; Hanson, J.; Clearfield, A.; Parise, J. B. *J. Am. Chem. Soc.* 2008, *130*, 11689.

(32) Celestian, A. J.; Parise, J. B.; Smith, R. I.; Toby, B. H.; Clearfield, A. *Inorg. Chem.* 2007, *46*, 1081.

(33) Sava, D. F.; Kravtsov, V. C.; Nouar, F.; Wojtas, L.; Eubank, J. F.; Eddaoudi, M. *J. Am. Chem. Soc.* 2008, *130*, 3768.

(34) Fang, Q.; Zhu, G.; Xue, M.; Wang, Z.; Sun, J.; Qiu, S. *Cryst. Growth Des.* 2008, *8*, 319.

(35) Yan Liu, G. L., Xing Li, Yong Cui, *Angew. Chem., Int. Ed.* 2007, *46*, 6301.

(36) Liu, Y.; Kravtsov, V. C.; Eddaoudi, M. *Angew. Chem., Int. Ed.* 2008, *47*, 8446.

(37) Nouar, F.; Eckert, J.; Eubank, J. F.; Forster, P.; Eddaoudi, M. *J. Am. Chem. Soc.* 2009, *131*, 2864.

(38) Stock, N.; Bein, T. *Angew. Chem., Int. Ed.* 2004, *43*, 749.

(39) Stoe & Cie GmbH: Darmstadt, 2004.

(40) Plabst, M.; Bein, T. *Inor. Chem.* 2009, *48*, 4331.

(41) Shannon, R. *Acta Crystallogr. Sect. A* 1976, *32*, 751.

(42) Baerlocher, C.; Hepp, A.; Institut für Kristallographie: Zürich, Switzerland, 1982.

(43) Jaulmes, S. Bull. Soc. Fr. Mineral. Cristallogr. 1972, 95, 42.

(44) Averbuch-Pouchot, M. T.; Durif, A. *J. Solid State Chem.* 1983, *46*, 193.

6 The Influence of the Guest Ion on the Synthesis and Sorption Properties of an Open Framework Lanthanide Tetrakisphosphonate

6.1 Introduction

One of the most desirable aspects in the synthesis of microporous materials is control over the pore system, including pore dimension and shape. In the field of zeolites and zeolite-like systems, constructing a framework around a template is a well-established strategy to approach this aim.1,2 Although real templating with guests imprinting their shape or geometry on the host structure is rare,[3,4] the crystallization of many zeolites only occurs in the presence of specific organic or inorganic cations,[5-7] which are then called structure directing agents (SDAs). In many other cases the guests are only pore fillers. For example, the structures of many metalorganic frameworks are usually defined by the coordination geometry of the framework metal in combination with the organic linker.[8] After synthesis, solvent molecules or excess ligands often occupy their pores. However, the interactions between the neutral frameworks and their guest molecules are often relatively weak. Therefore only few examples of structure direction in the field of metalorganic frameworks (MOFs) have been reported.[9-11] The first systematic investigation of the influence of SDAs on topological control in the synthesis of coordination polymers was carried out on compounds constructed from rare earth metals and flexible adipate ligands.[12-15] Unfortunately, the pyridyl-derived templates could not be removed from these compounds. The development of metal organic frameworks (MOFs) with charged frameworks increased the interest in network templating, as host-guest interactions can be stronger than in neutral frameworks.[9-11] In one of the first

systems studied in this context, several charge-balancing alkyl ammonium salts were introduced into a Mn / carboxylate system in order to produce a series of NaCl type frameworks.[16] Exploiting the same approach, an unprecedented new structure was recently found in the Z-MOF family; a class of materials with anionic zeolite-like framework derived from the coordination of single molecules by angular ditopic ligands.[17] Functionalized organic molecules are often used as SDAs. In these cases it is a challenge to avoid coordination of the SDA to the framework metal. This problem does not exist if the structure-directing agent is a metal ion with a low tendency to form coordination bonds. As an additional feature, the presence of metal ions in the pores of metalorganic framework materials significantly alters their sorption properties.[18,19]

In a recent high-throughput study on the hydrothermal crystallization behavior of the tetrakisphosphonic acid $(PO_3H_2)_2CH-C_6H_4-CH(PO_3H_2)_2$ **(H$_8$L)** (a ligand with two bisphosphonate groups connected by a rigid benzene linker) with lanthanide (III) ions, it was discovered that the addition of four equivalents of NaOH to a stoichiometric ratio of ligand and framework metal shifts the system from the crystallization of layered phosphonates towards three-dimensional open frameworks (chapter 4). A series of isomorphous compounds, **NaLn(H$_4$L)** (Ln = La, Nd, Gd, Dy) were synthesized. Structure solution of $NaLa[(PO_3H)_2CH-C_6H_4-CH(PO_3H)_2]·4H_2O$, **NaLa(H$_4$L)** revealed a three-dimensional coordination network formed by $(PO_3H)_2CH-C_6H_4-CH(PO_3H)_2{}^{4-}$ **(H$_4$L^{4-})** and La^{3+}. The La^{3+} ions are bridged into chains by the phosphonate groups of the **H$_4$L^{4-}** ligand. These chains are linked via the organic spacer into a three-dimensional anionic open framework. The framework features rhombic channels which are confined by the chains located at the corner of each rhombus and are filled with Na^+ ions and water molecules acting as guests (Figure 6.1 - 1). The aim of the present work is to investigate the role of the guest ion during the formation of the phosphonate framework. A high-throughput screening of the synthesis
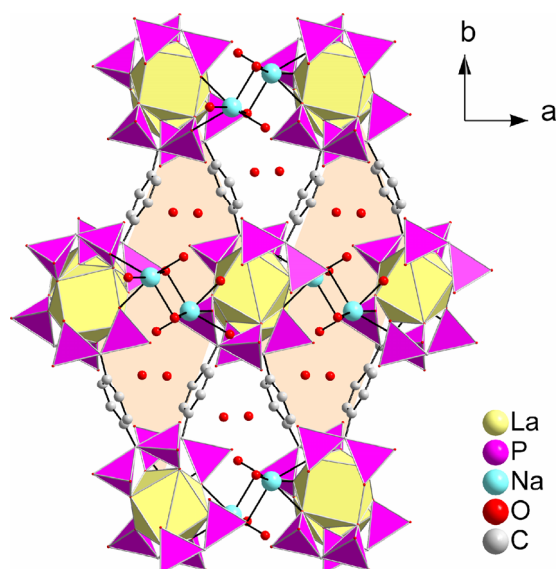
Figure 6.1 - 1: Projection of the NaLa(H₄L) structure showing the rhombus formed by the connection of phosphonate-bridged chains of La^{3+} ions (perpendicular to the page) and the H_4L^{4-} ligand. The channels are filled with Na^+ ions and water molecules.

conditions of **MLa(H₄L)** was performed, with various monovalent cations acting as possible guests. It can be shown that the guest ions exert a profound structure-directing effect on the synthesis of these lanthanide-phosphonate frameworks.Characterizing the new compounds **MLa(H₄L)** a strong dependence of the shape of the water sorption isotherms on the incorporated guest ions can be observed. Therefore in the following work a detailed study of the sorption properties of **LiLa(H₄L)**, **NaLa(H₄L)** and **KLa(H₄L)** is presented and discussed against the background of the flexible nature of their framework[20].

6.2 Experimental Section

General: Solvents and chemicals were purchased from Aldrich and were used as received. Bidistilled water was obtained from a Millipore system (Milli-Q Academic A10). 1 M aqueous solutions were prepared from $La(NO_3)_3 \cdot 6\ H_2O$, LiOH, NaCl and RbCl. 1 M volumetric standard solutions of NaOH and KOH were purchased. The molecular building block 1, 4-phenylenbis(methylidyne) tetrakis(phosphonic acid), **H₈L**, was prepared as described in chapter 3 and

135

provided as a 0.5 M aqueous solution. Conventionally synthesized NaLa[(PO$_3$H)$_2$CH-C$_6$H$_4$-CH(PO$_3$H)$_2$]·4H$_2$O, **NaLa(H$_4$L)**, was obtained as described in chapter 4.

For NMR studies solutions of 0.1 mmol of **H$_8$L** in 830 mmol H$_2$O were prepared, once with and once without 0.4 mmol of NaOH.

H$_8$L: ^{31}P-NMR (109.41 MHz, H$_2$O): δ = 17.94. ^{13}C-NMR (100.53 MHz, H$_2$O): 46.69, 2 x CH, t, ($^1J_{CP}$ = 127.86 Hz), CHP$_2$; 130.58, 4 x CH, C$_{ar}$; 131.52, 2 x C$_q$, C$_{ipso}$.

4NaOH/**H$_8$L**: ^{31}P-NMR (109.41 MHz, H$_2$O): δ = 15.85 (15.95, 15.76); ^{13}C-NMR (67.92 MHz, H$_2$O): 47.32, 2 x CH, t, ($^1J_{CP}$ = 116.09 Hz), CHP$_2$; 129.18, 4 x CH, C$_{ar}$; 132.03, 2 x C$_q$, C$_{ipso}$.

High-throughput screening reactions were performed in custom-made multiclave reactor blocks with 24 cavities containing individual Teflon liners of an individual total volume of 3 mL. Before each synthesis, the liners were cleaned in concentrated HCl and rinsed with water. They were then placed on a multi-stirrer device and equipped with small magnetic stirring bars. Reaction gels with a total volume of 1.5 mL were prepared according to the following general procedure: A 0.5 M solution of H8L was placed into the Teflon liner, deionized water was added, stirring was started and the 1 M solution of MX (MX = LiOH, KOH, NaCl, RbCl, NH$_4$OH) was added. After subsequent addition of a 1 M La(NO$_3$) solution, a precipitation occurred. The reaction mixture was stirred for 30 minutes until a homogenous gel was formed. After the removal of the stirring bars the pH was measured and the Teflon liners were transferred to the reactor block, in which each vessel was closed individually. Subsequently they were heated for 7 days. After the heating procedure the pH was measured again and crystals were separated from the reaction mixture by filtration under reduced pressure using a custom-made multi-filtration block and washed with water. Products were dried at room temperature and X-ray diffraction (XRD)

patterns were recorded. For NaCl screening, reactions were performed with the batch composition La(NO$_3$)$_3$: H$_8$L : x NaCl : 830 H$_2$O and x = 0, 0.5, 1, 2, 4, 8 and 12. A heating temperature of 150 °C was used. Screening of different guest ions was carried out with the batch composition La(NO3)3 : H8L : 4 MX : 830 H2O and MX = LiOH, KOH, NH$_4$OH and RbCl. The heating temperatures were 75 °C, 100 °C and 150 °C. Dilution series were performed at 150 °C for MX = LiOH, KOH, NH$_4$OH and RbCl with the batch composition La(NO$_3$)3 : H8L : 4 MX : z H$_2$O. The varied z values were z = 830, 1660, 2075, 8300, 16600, 83000. The optimal conditions for the preparation of LiLa(H$_4$L), NaLa(H$_4$L) with NaCl, KLa(H$_4$L), (NH$_4$)La(H$_4$L) and RbLa(H$_4$L) are given below:

NaLa(H$_4$L) was obtained with optimal crystallinity by the following procedure, when NaCl was the Na$^+$ source: To 0.2 mL of a 0.5 M aqueous solution of **H$_8$L**, 0.800 mL of of bidistilled water and 0.40 mL of a 1 M aqueous NaCl solution was added. Stirring was started and 0.1 mL of a 1 M solution of La(NO$_3$)$_3$ in bidistilled water was added. The gel with the batch composition La(NO$_3$)$_3$: H$_8$L : 4 NaCl : 830 H$_2$O was stirred for 30 minutes and then heated under hydrothermal conditions for one week at 150°C. The precipitated crystals were separated from the reaction mixture by filtration under reduced pressure, washed with deionized water and dried at room temperature. The pH of the reaction mixture was 1.0 both before and after the heating process. 59 mg (0.09 mmol, 90%) of NaLa[(PO$_3$H)$_2$CH-C$_6$H$_4$-CH(PO$_3$H)$_2$]·4H$_2$O were obtained. **Anal. calcd** for C$_8$H$_{18}$LaNaO$_{16}$P$_4$: C, 14.65; H, 2.77; La, 21.17; Na, 3.50; P, 18.89. Found: C, 14.70; H, 2.75; La, 20.80; Na, 3.10; P, 18.40.

LiLa(H$_4$L) was obtained by ion exchange of NaLa(H$_4$L) as described in chapter 5. **Anal. calcd** for C$_8$H$_{18}$LaLiO$_{16}$P$_4$: C, 15.01; H, 2.84; La, 21.71; Li, 1.08; O, 40.00; P, 19.36. Found: La, 20.10; Li, 1.17; P, 18.06.

KLa(H**$_4$L):** To 0.10 mL of a 0.5 M aqueous solution of **H$_8$L**, 1.15 mL of bidistilled water and 0.20 mL of a 1 M aqueous KOH solution was added. Stirring was started and 0.05 mL of a 1 M solution of La(NO$_3$)$_3$ in deionized water was added. The gel with the batch composition La(NO$_3$)$_3$: H$_8$L : 4 KOH : 1660 H$_2$O was stirred for 30 minutes and then heated under hydrothermal conditions for one week at 150 °C. The precipitated crystals were separated from the reaction mixture by filtration under reduced pressure, washed with deionized water and dried at room temperature. The pH of the reaction mixture was 4.0 before and 3.5 after the heating process. 28.9 mg (0.05 mmol, 91 %) of KLa[(PO$_3$H)$_2$CH-C$_6$H$_4$-CH(PO$_3$H)$_2$]·2H$_2$O were obtained. **Anal. calcd** for C$_8$H$_{14}$KLaO$_{14}$P$_4$: C, 15.11; H, 2.22; K, 6.15; La, 21.84; O, 35.21; P, 19.48. Found: C, 15.39; H, 1.98; K, 5.65; La, 23.80; P, 18.60.

(NH$_4$)La(H$_4$L): To 0.20 mL of a 0.5 M aqueous solution of **H$_8$L**, 0.80 mL of bidistilled water and 0.40 mL of a 1 M aqueous NH$_4$OH solution were added. Stirring was started and 0.1 mL of a 1 M solution of La(NO$_3$)$_3$ in deionized water was added. The gel with the batch composition La(NO$_3$)$_3$: H$_8$L : 4 NH$_3$: 833 H$_2$O was stirred for 30 minutes and then heated under hydrothermal conditions for one week at 150 °C. The precipitated crystals were separated from the reaction mixture by filtration under reduced pressure, washed with deionized water and dried at room temperature. The pH of the reaction mixture was 1.0 both before and after the heating process. 48.0 mg (0.078 mmol, 78 %) of NH$_4$La[(PO$_3$H)$_2$CH-C$_6$H$_4$-CH(PO$_3$H)$_2$]·2H$_2$O were obtained. **Anal. calcd** for C$_8$H$_{18}$LaNO$_{14}$P$_4$: C, 15.62; H, 2.95; La, 22.59; N, 2.28; O, 36.42; P, 20.14; found: C, 15.58; H, 2.93; La, 22.29; N, 2.14; P, 19.30.

(NH$_4$)La(H$_4$**L)** was additionally prepared by ion exchange, by stirring 100 mg of **NaLa(H$_4$L)** in 10 mL of a saturated aqueous solution of NH$_4$Cl for three days at room temperature. Thereafter the solid was separated from the solution by filtration under reduced pressure, briefly washed with bidistilled water and

dried at room temperature for two days. **Anal. calcd** for C$_8$H$_{18}$LaNO$_{14}$P$_4$: C, 15.62; H, 2.95; La, 22.59; N, 2.28; O, 36.42; P, 20.14. Found: C, 16.24; H, 2.70; La, 22.23; N, 2.11; P, 19.80.

RbLa(H$_4$L): To 0.20 mL of a 0.5 M aqueous solution of **H$_8$L**, 0.80 mL of bidistilled water and 0.40 mL of a 1 M aqueous RbCl solution were added. Stirring was started and 0.1 mL of a 1 M solution of La(NO$_3$)$_3$ in deionized water was added. The gel with the batch composition La(NO$_3$)$_3$: H$_8$L : 4 RbCl : 833 H$_2$O was stirred for 30 minutes and then heated under hydrothermal conditions for one week at 150 °C. The precipitated crystals were separated from the reaction mixture by filtration under reduced pressure, washed with deionized water and dried at room temperature. The pH of the reaction mixture was 1.0 both before and after the heating process. 54.60 mg (0.08 mmol, 80 %) of RbLa[(PO$_3$H)$_2$CH-C$_6$H$_4$-CH (PO$_3$H)$_2$]·2H$_2$O were obtained. **Anal. calcd** for C$_8$H$_{14}$LaO$_{14}$P$_4$Rb: C, 14,08; H, 2,07; La, 20.35; O, 32.82; P, 18.15; Rb, 12.52. Found: C, 14.66; H, 2.22; La, 20.17; P, 18.16; Rb, 10.92.

Characterization: ^{13}C- and ^{31}P-NMR spectra of the precursor solutions (of 0.1 mmol of H$_8$L in 830 mmol H$_2$O with and without 0.4 mmol of NaOH) were recorded at room temperature on a JEOL EX 400 and a JEOL GSX 270. The chemical shift is given relative to tetramethylsilane (TMS) or H$_3$PO$_4$, respectively. High-throughput X-ray diffraction analysis of all samples of the discovery library was carried out using a Stoe high-throughput powder diffractometer equipped with an image plate detector system.[21] Higher resolution X-ray powder diffraction patterns were recorded in theta-theta geometry with a Bruker D8 Discover instrument using monochromatic CuK$_\alpha$ radiation and a Vantec detector. The XRD patterns of the flexible frameworks change with the water content of the samples. Therefore samples of **KLa(H$_4$L)** were humidified before measurement to obtain the pattern of the hydrated expanded form. Samples of ion-exchanged **NH$_4$La(H$_4$L)** were slowly dried at

room temperature for two days before measurement. Morphology and stoichiometry were studied with a Jeol JSM 6500 F scanning electron microscope equipped with an EDX detector. The respective samples were applied to an adhesive carbon film on the sample holder and coated with carbon with a BAL-TEC MED 020 Coating System. The chemical compositions of all samples **MLa(H₄L)** were determined by inductively coupled plasma optical emission spectroscopy (ICP-OES, VARIAN VISTA) and an ELEMENTAR vario EL. Sorption isotherms were determined in a pressure range from $(p/p_0) = 0.001$ to 1 using a static volumetric technique on a Quantachrome Autosorb 1 with N_2 and Kr as sorptives at 77 K. Water sorption was carried out at 291 K, and with a minimum equilibration time of 3 minutes per data point. A typical experiment was stopped after about four days when pressure had remained constant at $p/p_0 = 0.05$ for several hours. Prior to the adsorption experiments, the samples were out-gassed under vacuum at 150 °C for 5 h. All measurements were repeated in order to confirm the reproducibility of the isotherms. Thermogravimetric analyses (TGA) were performed on a Netzsch STA 449 C TG/DSC, heating the sample with a rate of 10 K/min in a stream of synthetic air of ~25 mL/min.

6.3 Results and Discussion

$NaLa(H_4L)$ forms readily at a batch composition of $La(NO_3)_3 : H_8L : 4\ NaOH : x$ H_2O over a broad temperature range and at various dilution degrees of the reaction gel. The determining factor for the formation is the stoichiometric ratio of one equivalent of lanthanide for each ligand and the additional presence of four equivalents of NaOH (Figure 6.3 - 1, route I). The role of NaOH in this reaction is not entirely evident. It was initially added to influence the degree of deprotonation of **H₈L**. However, as one equivalent of Na^+ is incorporated in the structure the question arises whether OH^- or Na^+ are decisive for the successful formation of the three-dimensional network. This question was addressed by

substituting NaOH with NaCl in a high-throughput approach. Synthesis was performed at batch compositions of La(NO$_3$)$_3$: H$_8$L : x NaCl : 830 H$_2$O with x = 0, 0.5, 1, 2, 4, 8 and 12 for 3 days at 150 °C. Products were evaluated comparing their powder patterns, crystal morphologies and elemental compositions. At very low Na$^+$ contents (x = 0 to 0.5) **La(H$_5$L)·a,**[22] a layered lanthanum phosphonate with no Na$^+$ incorporated in the structure was formed Figure 6.3 - 2a, b). Between x = 1 and 2, a mixture of unknown phases was obtained (Figure 6.3 - 2c). EDX analysis indicated a low content of Na$^+$ (4%) and SEM micrographs showed crystals with a sheet-like morphology (Figure 6.3 - 2d). It can be assumed that small amounts of sodium were incorporated between the layers in a disordered manner. If x ≥ 4, **NaLa(H$_4$L)** was formed with good crystallinity (Figure 6.3 − 2e and f). An excess of Na$^+$ in the synthesis gel was suitable for crystal formation as crystal size increased with increasing Na$^+$ content. This result demonstrates that Na$^+$ is essential for the crystallization of the open framework **NaLa(H$_4$L)**. The open question remains why four equivalents of Na$^+$ are required in the synthesis gel, although only one equivalent is incorporated in the structure. An explanation might be the formation of a Na$_4$(H$_4$L)$_{solv}$ precursor complex in solution, which provides the ligand in the adequate conformation and degree of protonation for the subsequent network formation with La^{3+}. NMR spectroscopy provides evidence for such interactions between sodium ions and the tetrakis phosphonate ligand. The ^{31}P-NMR signal of (PO$_3$H$_2$)$_2$CH-C$_6$H$_4$-CH(PO$_3$H$_2$)$_2$ ¸ **(H$_8$L)**, shifts from 17.94 ppm to 16.35 ppm after the addition of 4 equivalents of NaOH. Additionally the NMR signal is split into two (16.46 ppm, 15.25 ppm). The unchanged set of ^{13}C signals still indicates the presence of a mirror plane going through the benzene ring. Thus, the two different signals can be assigned to two different phosphonates of the same bisphosphonate group, which can be explained either by unequal complexation of Na$^+$ or by a differing degree of deprotonation.
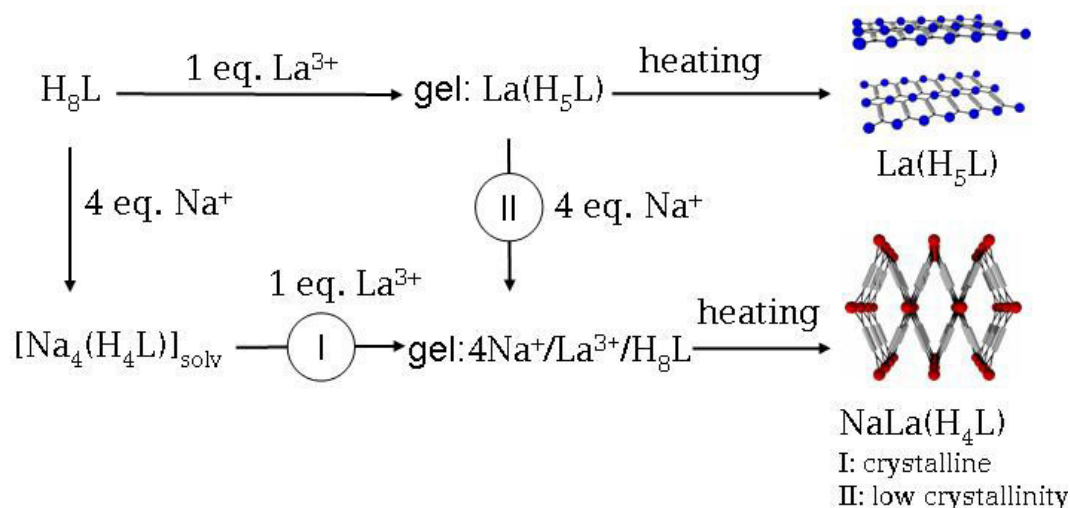
Figure 6.3 - 1: Reaction scheme of the crystallization system Na$^+$/La^{3+}/H$_8$L.

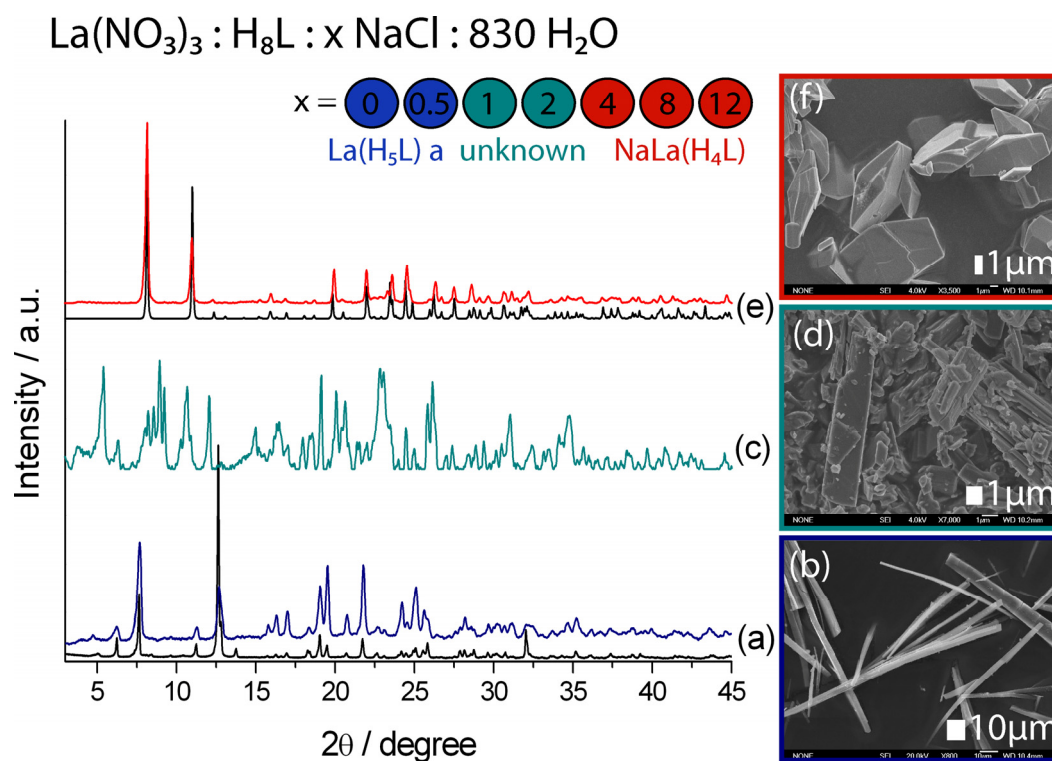**Figure 6.3 - 2:** Results of the NaCl screening: a) XRD pattern of a sample without NaCl (x=0) (blue) compared to the pattern of NaLa(H$_5$L)·a (black)[22]; b) crystals of sample a; c) XRD pattern of a sample with a NaCl : H$_8$L ratio of 2; f) crystals of sample c; e) sample with a NaCl : H$_8$L = ratio of 4 (red) compared to the simulated pattern of **NaLa(H$_4$L)** (black)[22]; f) crystals of **NaLa(H$_4$L)** obtained at a NaCl : H$_8$L ratio of 12.

The influence of the order of addition of the metal ions to the reaction mixture is yet another indication that a complex between H$_8$L and Na$^+$ ions in solution is implicated in the structure formation of **NaLa(H$_4$L)**. The syntheses described above were all performed via route I (Figure 6.3 - 1): The synthesis gel was prepared by adding the framework metal La^{3+} to a solution containing the ligand, **H$_8$L**, and Na$^+$. Alternatively, the order of metal addition was inverted (route II); this results in the initial formation of a gel from **H$_8$L** and La^{3+}. Subsequently, after a stirring time of 30 minutes, Na$^+$ was added. In the batches prepared using the latter methodology, **NaLa(H$_4$L)** was still formed but the crystallinity detected by XRD was comparatively poor (Figure 6.3 - 3). In the morphology of some crystals the characteristic rhombic motif could still be identified, but most of them lost the typical crystal shape of NaLa(H$_4$L) (Figure 6.3 - 4). Having identified Na$^+$ as template for the structure formation, the question arises if it can be substituted by other monovalent cations. In order to address this issue, Na$^+$ was replaced in another series of experiments by Li$^+$, K$^+$, NH$_4^+$ or Rb$^+$, which, based on ion-exchange experiments[20], are all known to fit in the channels. Synthesis with LiOH did not yield the target structure (Figure 6.3 - 5), but isostructural compounds **MLa(H$_4$L)** were formed with K$^+$, NH$_4^+$ and Rb$^+$. However, the parameter range that allows successful crystallization of the respective phase is considerably smaller than with Na$^+$. In all three cases higher temperatures were required (Figure 6.3 - 5a). While **NaLa(H$_4$L)** forms already at 75 °C, **KLa(H$_4$L)** requires at least 100 °C. **(NH$_4$)La(H$_4$L)** and **RbLa(H$_4$L)** do not crystallize below 150 °C. Additionally, **NaLa(H$_4$L)** and **KLa(H$_4$L)** crystallize at 150 °C from concentrated gels as well as from highly diluted mixtures (Figure 6.3 - 5b), while **NH$_4$La(H$_4$L)** and **RbLa(H$_4$L)** were obtained phase-pure only with the initial water content of x = 830 in the synthesis. From these results an order of suitability can be derived showing that Na$^+$ > K$^+$ >> NH$_4^+$, Rb$^+$ for the
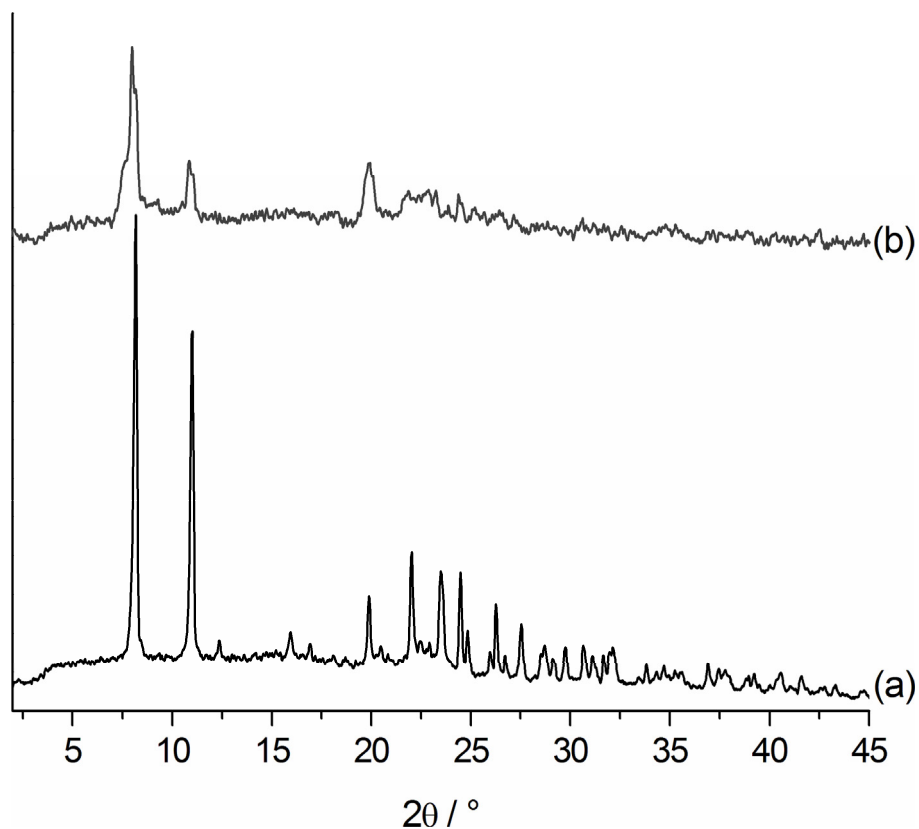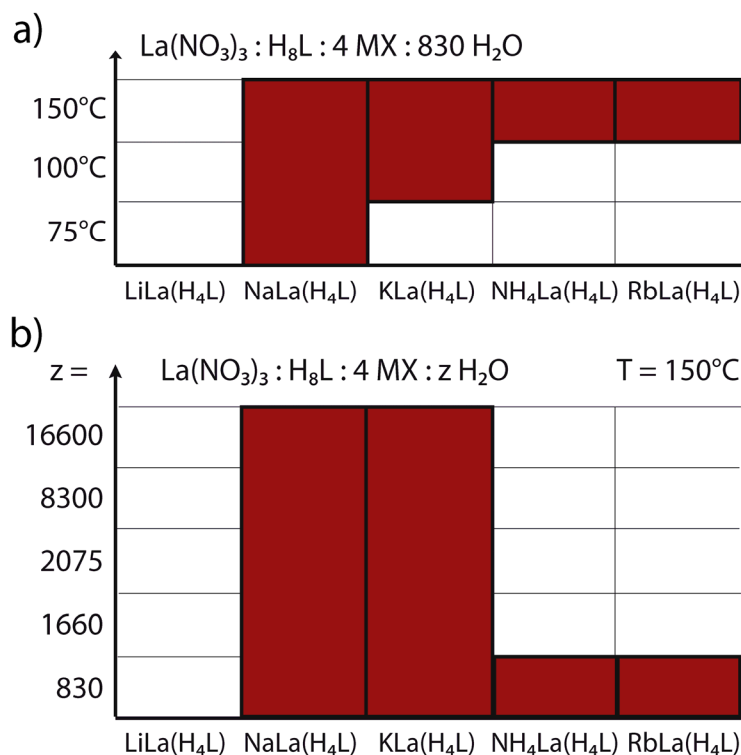
Figure 6.3 ‑ 3: XRD of **NaLa(H$_4$L)** a) synthesized according to route I, adding Na$^+$ before La^{3+}. b) synthesized according to route II, adding Na$^+$ to the gel of H$_8$L and La^{3+}. Intensities are comparable due to equal measurement times.
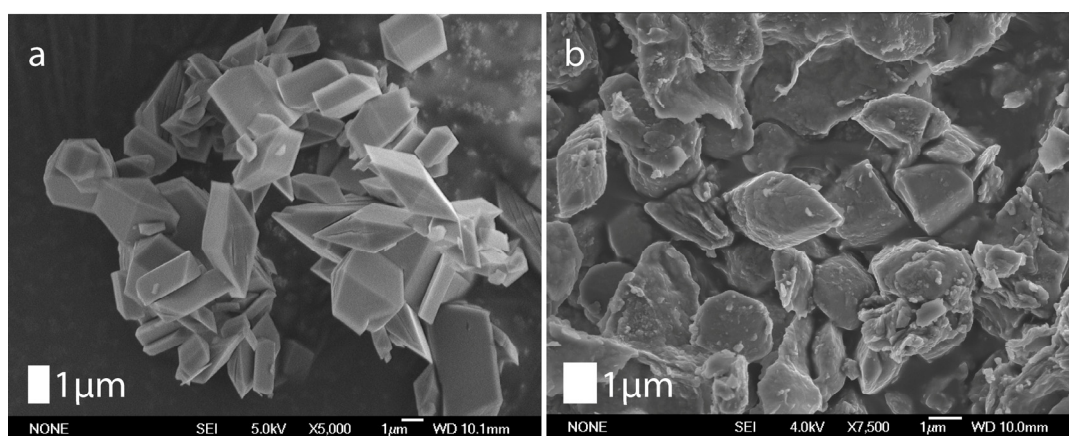
Figure 6.3 ‑ 4: Crystal morphology of NaLa(H$_4$L): a) prepared using route I; b) prepared using route II.

a)

La(NO_3)$_3$: H_8L : 4 MX : 830 H_2O

b)

La(NO_3)$_3$: H_8L : 4 MX : z H_2O T = 150°C

Figure 6.3 - 5: Parameter screening in the synthesis of MLa(H_4L): a) temperature; b) degree of dilution.

structure formation of **MLa(H_4L)**. Summarizing all these trends it can be stated that Na^+ is a strong structure-directing agent in the synthesis of **NaLa(H_4L)**.

Characterization of the synthesized compounds **MLa(H_4L)** was performed with XRD, scanning electron microscopy and elemental analysis. All XRD patterns were similar to the simulated pattern of **NaLa(H_4L)**, obtained by XRD structure analysis (Figure 6.3 - 6). The powder patterns of **KLa(H_4L)** and **RbLa(H_4L)** are in good agreement with the patterns obtained by ion exchange described elsewhere[20]. To confirm the pattern of **(NH$_4$)La(H_4L),** the compound was additionally prepared by ion exchange and the similarity of both patterns verified. The crystals of **KLa(H_4L)** and **(NH$_4$)La(H_4L)** are strongly intergrown and vary in length and size compared to the well-defined crystals of **NaLa(H_4L)** (Figure 8.3.1 - 1a,b). On higher magnification micrographs the typical rhombic
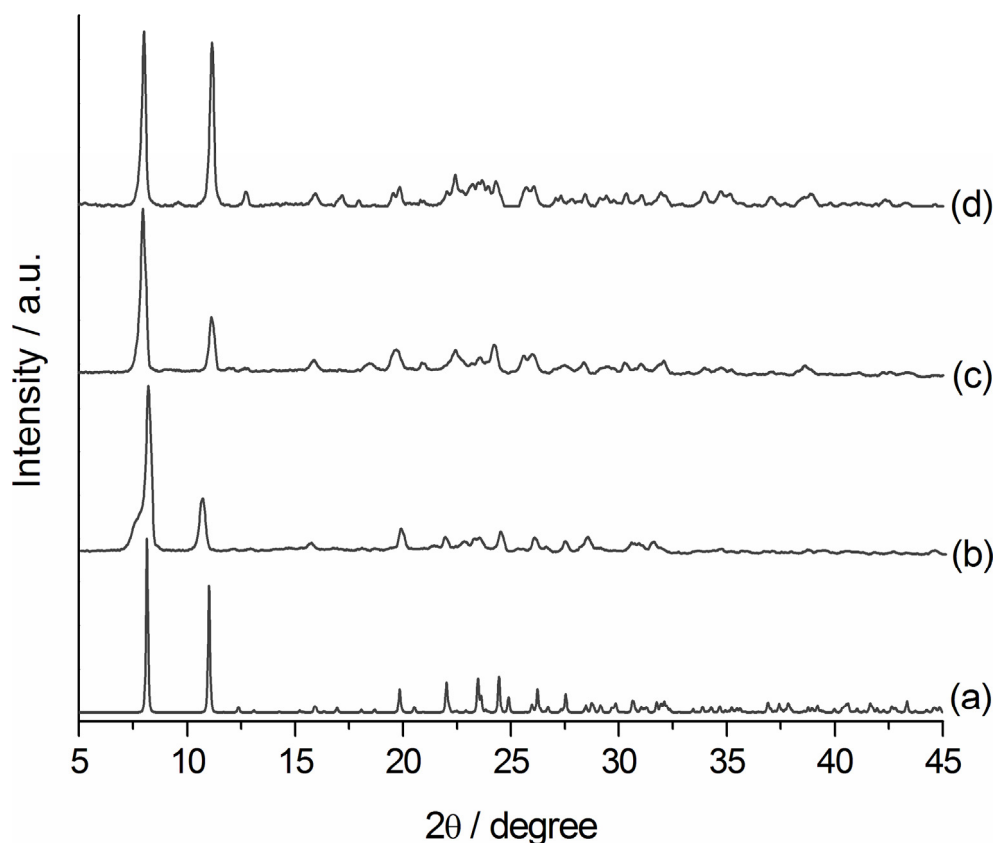
Figure 6.3‑6: Simulated XRD of NaLa(H$_4$L) (a) in comparison to the experimental XRD of b) a humidified sample of KLa(H$_4$L) c) **RbLa(H$_4$L)** and d) **(NH$_4$)La(H$_4$L)**.

motif can still be recognized. **RbLa(H$_4$L)** crystals are larger and similar to **NaLa(H$_4$L)** crystals (Figure 8.3.1‑1c). To investigate the accessibility of the one-dimensional rhombic channels of **NaLa(H$_4$L)**, gas sorption was measured for N$_2$, Kr and H$_2$O. The samples for gas sorption measurements were prepared by heating NaLa(H$_4$L) at 150 °C under vacuum for 5 h to remove all guest water molecules. From the XRD studies described in chapter 5 it is known that the rhombic channels of NaLa(H$_4$L) contract upon dehydration (Figure 6.3‑7a), which leads to a decrease in the cell volume by 15%. In this process the sodium ions, which are strongly connected to only one side of the channel walls in the expanded hydrated form, become attached to both sides of the channels thus generating a La-O-M-O-La chain perpendicular to the lanthanum phosphonate chains of the initial network. Before a considerable amount of gas can be

146

absorbed, the channels have to be opened again. As the sorption isotherms demonstrate, this can only be achieved with water molecules (Figure 6.3 - 7b). The small and polar water molecules can enter the channels, while non-polar gases such as N$_2$ or Kr are excluded. At first glance, the water sorption isotherm of **NaLa(H$_4$L)** is similar to a type I isotherm with larger micropores. However, a closer look reveals small differences. From p/p0 = 0 to p/p0 = 0.024, only moderate water adsorption takes place. Then a steep increase of the curve between p/p0 = 0.02 and p/p0 = 0.05 can be observed. The adsorbed volume of water during this step is 42.23 cm^3/g. This distinctive step of volume uptake can be correlated to the opening of the channels of the flexible framework. After this step, the adsorption branch flattens again and the adsorbed amount of water increases slowly up to 117.5 cm^3/g at p/p0 = 0.88. The desorption branch follows the adsorption with an apparent hysteresis that becomes more pronounced at lower partial pressures. This hysteresis can be attributed to very slow desorption. Desorption cannot be completed due to the strong bonds of the water molecules to the framework, and therefore the measurement was stopped after loading remained constant at p/p0 = 0.05 for several hours.

The above interpretation of the isotherm can be confirmed by comparing the water sorption isotherm of **NaLa(H$_4$L)** with the water sorption isotherms of **LiLa(H$_4$L)** and **KLa(H$_4$L).** For these experiments **LiLa(H$_4$L)** was prepared by ion exchange. Similar to the isotherm of **NaLa(H$_4$L),** the isotherms of **LiLa(H$_4$L)** and **KLa(H$_4$L)** both show a steep increase in the adsorption curve that corresponds to a volume uptake of 40.0 cm^3/g and 43.3 cm^3/g respectively (Figure 6.3 - 7c, d), which can be attributed to the channel expansion in the structures. The channel expansion occurs at different partial pressures depending on the incorporated guest ion. In the case of **LiLa(H$_4$L),** the corresponding adsorption step already starts at a low partial pressure of p/p$_0$ = 0.01. Due to its high hydration energy, all adsorbed water rapidly coordinates to Li$^+$ and the channels

expand allowing further sorption of water into the pore system. In contrast, in the case of **KLa(H₄L)** the starting point of this step is greatly shifted towards a higher partial pressure of $p/p_0 = 0.38$. The hydration enthalpy of K^+ is lower in comparison to Li^+ and Na^+. Therefore, water is initially adsorbed on the surface and in the voids of the contracted form until a certain water concentration is reached in the solid. Only then does the La-O-K-O-La chain of the contracted form open, K^+ becomes hydrated and the equilibrium is shifted to the side of the expanded form. These observations are in good agreement with earlier XRD experiments.[20] It was shown that in air and at room temperature, **LiLa(H₄L)** and **NaLa(H₄L)** are present in the hydrated expanded form, while the expanded form of **KLa(H₄L)** could only be observed when increasing the water concentration by humidifying the sample. In **KLa(H₄L)** the hysteresis during desorption is much more strongly pronounced than in the isotherms of **NaLa(H₄L)** and **LiLa(H₄L)**. The desorption curve shows a steep desorption step of 40.2 cm^3/g at a partial pressure of $p/p_0 = 0.16$, which can be correlated to pore contraction. Accordingly, the removal of water and the shift back into the contracted form is kinetically inhibited. Generally, the total pore volume derived from water sorption increases when going from **LiLa(H₄L)** to **KLa(H₄L)**. This is in good agreement with the increasing unit cells of the structures of the hydrated expanded forms (Table 6.3 - 1). The water sorption isotherms of **RbLa(H₄L)** and **(NH₄)La(H₄L)** cannot be described using this model. Both adsorb much less water and show no significant step of vapor uptake in the isotherms (Figure 8.3.2 - 1). In the case of **RbLa(H₄L)**, pore opening was not observed in XRD either. The large ionic radius and the low hydration enthalpy of Rb^+ lead to a strong stabilization of the contracted form. In **(NH₄)La(H₄L)**, interactions between the guest ions and the channel walls rely on hydrogen-bonding. The bonding situation is therefore not comparable to the compounds
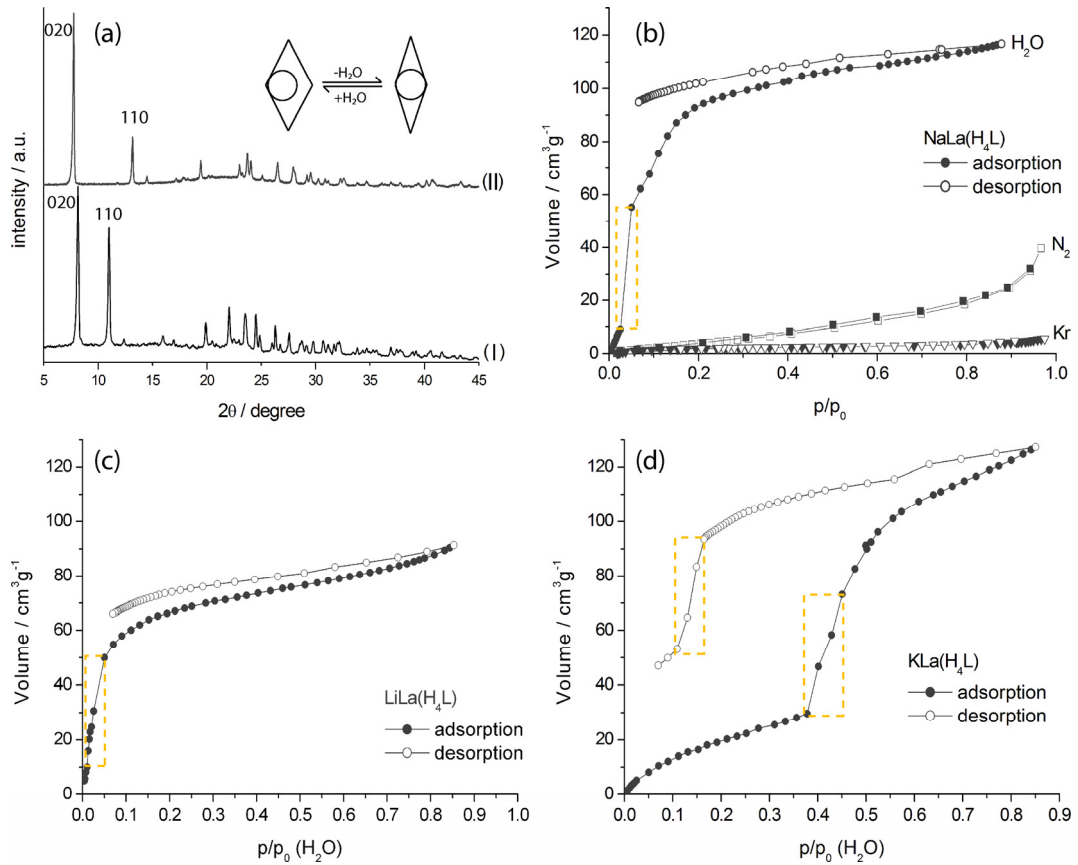
Figure 6.3 - 7: a) Shrinking of the rhombic channels of **NaLa(H₄L)** during reversible dehydration demonstrated by XRD;[20] (I) pattern of **NaLa(H₄L)**·$4H_2O$; (II) pattern of dehydrated **NaLa(H₄L)**; b-d) Water sorption isotherms of b) **NaLa(H₄L)** c) **LiLa(H₄L)** and d) **KLa(H₄L)**. The stepwise increase in adsorbed volume due to the opening of the channels in the flexible framework is highlighted in yellow.

Table 6.3 - 1: Total pore volume (V_{ads}) for a water partial pressure of $p/p_0 = 0.85$ and volume of the unit cells[20] of MLa(H₄L) with M=Li, Na, K.

MLa(H₄L)	V_{ads} / 10^{-2} cm^3g^{-1}	$V_{unit\ cell}$ / $Å^3$
LiLa(H₄L)	7.35	1901.6
NaLa(H₄L)	9.34	1910.2
KLa(H₄L)	10.26	1976.9

with metal ions acting as guests. Thermogravimetric analysis supports this conclusion (Figure 8.3.3 - 1). While in the alkali metal containing compounds water removal from the structure takes place at 100 °C in one endothermic step, in the TGA diagram of **(NH$_4$)La(H$_4$L)** two endothermic steps can be observed at 85 °C and at 120 °C indicating that water molecules are involved in different hydrogen-bonding modes. The ammonium ions are not removed during this treatment.

6.4 Conclusion

The structure directing role of the Na+ guest ions in the synthesis of the recently discovered anionic open framework tetrakisphosphonate NaLa[(PO$_3$H)$_2$CH-C$_6$H$_4$-CH(PO$_3$H)$_2$]·4H$_2$O **(NaLa(H$_4$L))** was studied. A high-throughput screening of the synthesis parameters revealed that its presence is important for the successful network formation, at a molar ratio higher than that incorporated into the framework. This finding and the observed effect of the order of metal ion addition during gel preparation on crystallinity leads to the assumption that a Na$_4$(H$_4$L)$_{solv}$ precursor exists in solution which favors the crystallization of **NaLa(H$_4$L)**. The synthesis of isomorphous compounds MLa(H$_4$L) can be performed with K$^+$, NH$_4^+$ and Rb$^+$ in the following order of suitability: Na$^+$ > K$^+$ >> NH$_4^+$, Rb$^+$. Li$^+$ does not lead to the formation of the respective structure. From all these results it can be concluded that Na$^+$ is a strong structure-directing agent in the synthesis of **NaLa(H$_4$L)**. Sorption measurements show that only the polar water molecules can open and intrude the channels of the flexible framework of **NaLa(H$_4$L)**, while non-polar gases such as N$_2$ or Kr are excluded. In the water sorption isotherms of **LiLa(H$_4$L)**, **NaLa(H$_4$L)** and **KLa(H$_4$L)**, an adsorption step can be observed; this can be correlated to the expansion of the channels in the flexible framework. The required partial pressure for the pore expansion depends on the incorporated

guest ion and increases with the decreasing hydration enthalpy from Li$^+$ to K$^+$. The structure-directing effect of the guest ion in combination with its influence on sorption properties observed in this study suggests new opportunities for the design of MOF materials constructed around metal ions as guests.

6.5 References

(1)   Cundy, C. S.; Cox, P. A. *Chem. Rev.* 2003, *103*, 663.

(2)   Davis, M. E.; Lobo, R. F. *Chem. Mater.* 1992, *4*, 756.

(3)   Lawton, S. L.; Rohrbaugh, W. J. *Science* 1990, *247*, 1319.

(4)   Wessels, T.; Baerlocher, C.; McCusker, L. B.; Creyghton, E. J. *J. Am. Chem. Soc.* 1999, *121*, 6242.

(5)   Gies, H.; Marker, B. *Zeolites* 1992, *12*, 42.

(6)   Kubota, Y.; Helmkamp, M. M.; Zones, S. I.; Davis, M. E. *Microporous Mater.* 1996, *6*, 213-229.

(7)   Wagner, P.; Nakagawa, Y.; Lee, G. S.; Davis, M. E.; Elomari, S.; Medrud, R. C.; Zones, S. I. *J. Am. Chem. Soc.* 2000, *122*, 263.

(8)   Eddaoudi, M.; Moler, D. B.; Li, H.; Chen, B.; Reineke, T. M.; O'Keeffe, M.; Yaghi, O. M. *Acc. Chem. Res.* 2001, *34*, 319.

(9)   Tynan, E.; Jensen, P.; Kruger Paul, E.; Lees Anthea, C. *Chem. Commun.* 2004, 776.

(10)   Fletcher A., J.; Cussen E., J.; Bradshaw, D.; Rosseinsky M., J.; Thomas, K. M. *J. Am. Chem. Soc.* 2004, *126*, 9750.

(11)   Choi, E.-Y.; Park, K.; Yang, C.-M.; Kim, H.; Son, J.-H.; Lee, S. W.; Lee, Y. H.; Min, D.; Kwon, Y.-U. *Chem. Eur. J.* 2004, *10*, 5535.

(12)   Sun, Z.-G.; Ren, Y.-P.; Long, L.-S.; Huang, R.-B.; Zheng, L.-S. *Inorg. Chem. Commun.* 2002, *5*, 629.

(13)   de Lill, D. T.; Cahill, C. L. *Cryst. Growth Des.* 2007, *7*, 2390.

(14)   de Lill, D. T.; Gunning, N. S.; Cahill, C. L. *Inorg. Chem.* 2005, *44*, 258.

(15)   de Lill, D. T.; Bozzuto, D. J.; Cahill, C. L. *Dalton Trans.* 2005, 2111.

(16)   Wang, Z.; Zhang, B.; Otsuka, T.; Inoue, K.; Kobayashi, H.; Kurmoo, M. *Dalton Trans.* 2004, 2209.

(17)   Liu, Y.; Kravtsov, V. C.; Eddaoudi, M. *Angew. Chem., Int. Ed.* 2008, *47*, 8446.

(18)   Mulfort, K. L.; Hupp, J. T. *Inorg. Chem.* 2008, *47*, 7936.

(19)   Dinca, M.; Long, Jeffrey R. *Angew. Chem.* 2008, *120*, 6870.

(20)   Plabst, M.; McCusker, L. B.; Bein, T. *J. Am. Chem. Soc.* 2009, DOI: 10.1021/ja904636y.

(21)   Stock, N.; Bein, T. *Angew. Chem., Int. Ed.* 2004, *43*, 7492.

(22)   Plabst, M.; Bein, T. *Inorg. Chem.* 2009, *48*, 4331.

7 Conclusions

Phosphonic acids and lanthanides are both promising building blocks for the synthesis of new metal organic frameworks (MOFs). However, their chemical and structural flexibility challenges the tailoring of well defined three-dimensional open framework structures. This thesis addresses this limitation introducing a new building block in metal phosphonate chemistry.

Initially a synthesis route to 1,4 phenylenebis(methylidyne)tetrakis(phosphonic acid) $(H_2O_3P)_2CH\text{-}C_6H_4\text{-}CH(PO_3H_2)_2$, **(H$_8$L)**, a new type of building block was developed. Instead of single phosphonate functionalities it contains bisphosphonate groups and thus provides large chelating ligands that are expected to bond more specifically to large and hard metal centers. Moreover its functional groups are connected without freedom of rotation to the rigid organic spacer in order to restrict the possibilities of a free assembly of the molecule.

The new ligand **H$_8$L** was then proven in hydrothermal synthesis to be a suitable building block for metal organic frameworks. Using a high throughput approach, the building block was combined with lanthanide(III) ions as corresponding metal centers. Using this approach, 14 new lanthanide phosphonates were discovered, categorized into three structure types and their crystallization fields described. Structure type **I** is formed by **H$_8$L** with one equivalent of metal. It comprises various layered structures on the basis of a two-dimensional coordination network where the lanthanide is coordinated by bisphosphonate groups, phosphonate groups and water molecules. If an excess of lanthanide ions is present during synthesis, compounds with structure type **II** are formed, where the metal centers of the two-dimensional coordination network are associated into dimers. The most interesting structure type emerges when four equivalents of NaOH are added to the reaction mixture of

H$_8$L, with one equivalent of metal. With this synthesis stoichiometry, crystals with the three-dimensional open framework of structure type **III** were obtained over a broad range of temperatures and concentrations. In this structure type, a well-defined coordination geometry was achieved with the lanthanide ions coordinated by bisphosphonate units in an exclusively bidentate fashion. The structure provides one-dimensional rhombic channels with sodium ions and water molecules acting as guests.

NaLa(H$_4$L) features a flexible open-framework anionic host with an extraordinary charge selectivity for its guest cations. The water molecules in the channels can be removed by heating, and this causes a shrinking of the channels and a decrease in the cell volume of 15 %. Upon dehydration, the Na$^+$ ions compensate for the loss of coordinated water by forming new bonds with phosphonate oxygens, and in the process generate an -La-O-Na-O-La- chain perpendicular to the lanthanum phosphonate chain of the original coordination network. The formation of this second chain stabilizes the framework and can be considered to be the driving force for the structural transformation. This dehydration process is fully reversible.

In aqueous media, the Na$^+$ ions hosted in the channels of the structure can be exchanged with other monovalent ions, while divalent ions in the same size range are rejected. Besides **NaLa(H$_4$L),** the ion-exchanged compounds **LiLa(H$_4$L)** and **KLa(H$_4$L)**, too, can exist in both the expanded and the contracted form, whereas **RbLa(H$_4$L)** is only found in the contracted form. The ionic radius and the enthalpy of hydration of the guest cation were seen to influence the equilibrium between the two forms. The framework adapts to the water content or the guest cation, and a volume change of 22% was observed in going from the dehydrated contracted Na$^+$ form to the expanded hydrated K$^+$ form. The key role played by the ionic guest in the chain-forming mechanism and the adaptation of the framework to the size of the cation both show the relevance of

the exchangeable cations to framework stabilization and charge balance. The monovalent guest cations are located at specific sites in the structure, where they can satisfy their coordination requirements. Divalent ions could occupy only half of these sites, and this might explain the unusual selectivity of this material for monovalent cations.

Furthermore, the structure-directing role of the Na^+ guest ions during the synthesis of **NaLa(H$_4$L)** was studied. A high-throughput screening of the synthesis parameters revealed that its presence is important for the successful network formation, at a molar ratio higher than that incorporated into the framework. This finding and the observed effect of the order of metal ion addition during gel preparation on crystallinity leads to the assumption that a $Na_4(H_4L)_{solv}$ precursor exists in solution which favors the crystallization of **NaLa(H$_4$L)**. The synthesis of isomorphous compounds MLa(H$_4$L) can be performed with K^+, NH_4^+ and Rb^+ in the following order of suitability: $Na^+ > K^+ \gg NH_4^+, Rb^+$. Li^+ does not lead to the formation of the respective structure. From all these results it can be concluded that Na^+ is a strong structure-directing agent in the synthesis of **NaLa(H$_4$L)**.

Sorption measurements showed that only the polar water molecules can open and intrude the channels of the flexible framework of **NaLa(H$_4$L)**, while non-polar gases such as N_2 or Kr are excluded. In the water sorption isotherms of **LiLa(H$_4$L)**, **NaLa(H$_4$L)** and **KLa(H$_4$L)**, an adsorption step can be observed; this can be correlated to the expansion of the channels in the flexible framework. The required partial pressure for the pore expansion depends on the incorporated guest ion and increases with the decreasing hydration enthalpy from Li^+ to K^+.

In conclusion, this work demonstrates that the bisphosphonate group connected to an aromatic spacer provides excellent access to MOFs of hard metals with high coordination numbers that are not easily synthesized with other ligands.

Regarding their properties, such polar materials with anionic frameworks are complementary to common MOF materials and build a bridge between MOFs and zeolites.
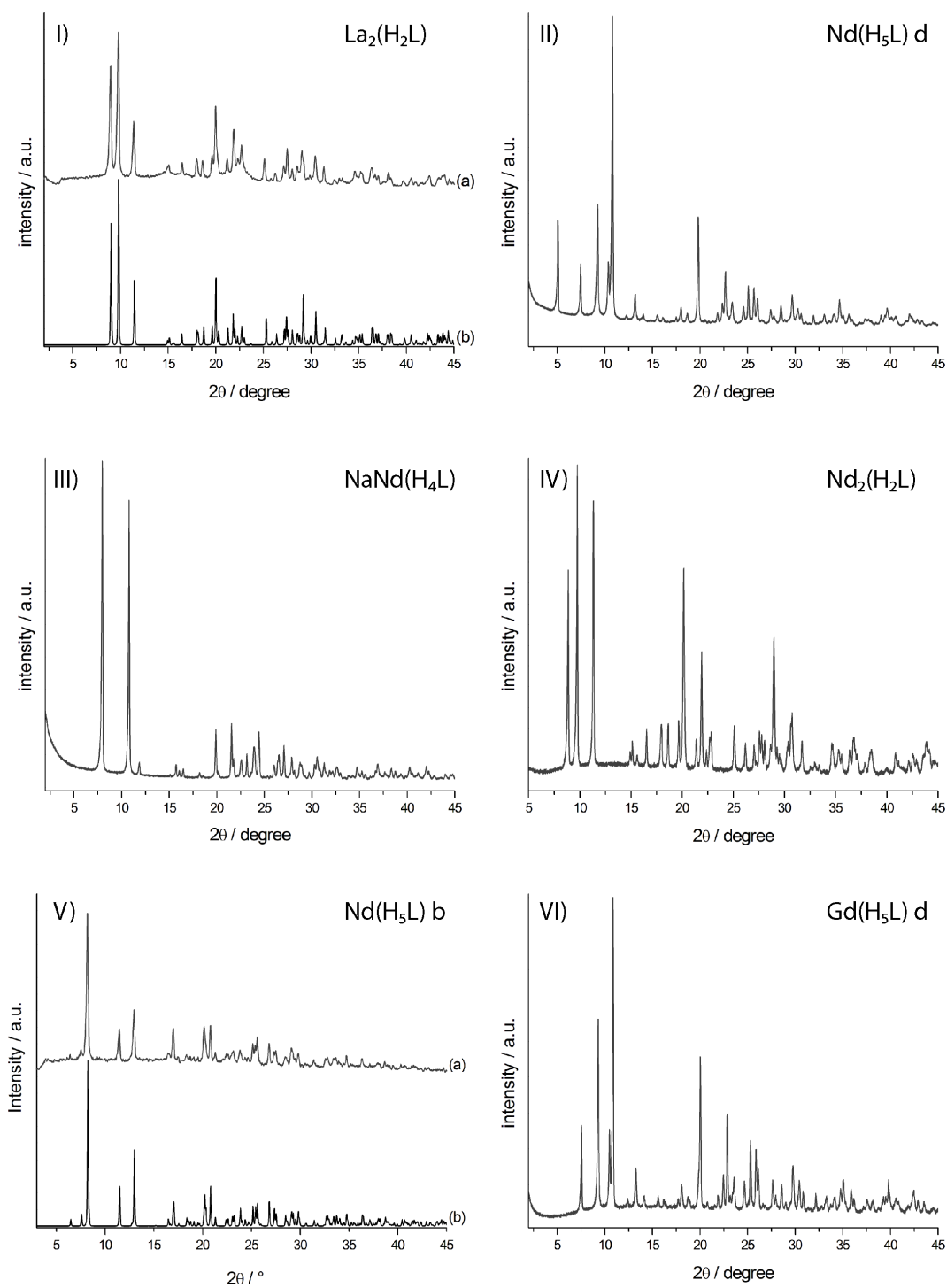
# 8 Supporting Information

8.1 Supporting Information to Chapter 4

### 8.1.1 XRDs of New Phases Discovered in the High-Throughput Screening
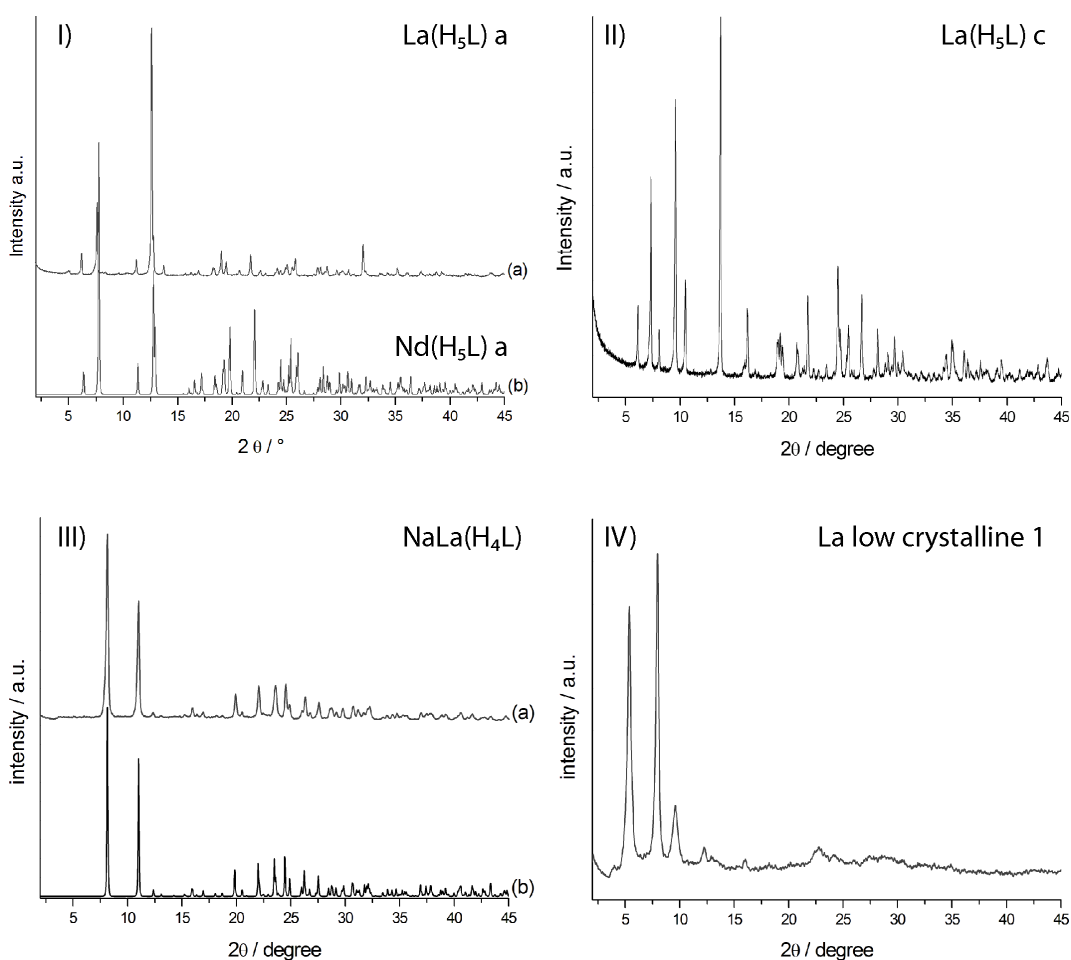
Figure 8.1.1-1: I) a) Experimental XRD pattern of **La(H₅L) a**; b) simulated pattern of **Nd(H₅L)** a; II) XRD pattern of **La(H₅L) c**; III) Experimental (a) and simulated (b) XRD pattern of NaLa(H4L); IV) XRD pattern of **La-low crystalline 1**.

Figure 8.1.1-2: I) Experimental (a) and simulated (b) XRD pattern of **La₂(H₂L)**; II) XRD pattern of **Nd(H₅L) d**; III) XRD pattern of **NaNd(H₄L)**; IV) XRD pattern of **Nd₂(H₂L)**; V) Experimental (a) and simulated (b) XRD pattern of **Nd(H₅L) b**; VI) XRD pattern of **Gd(H₅L) d**.
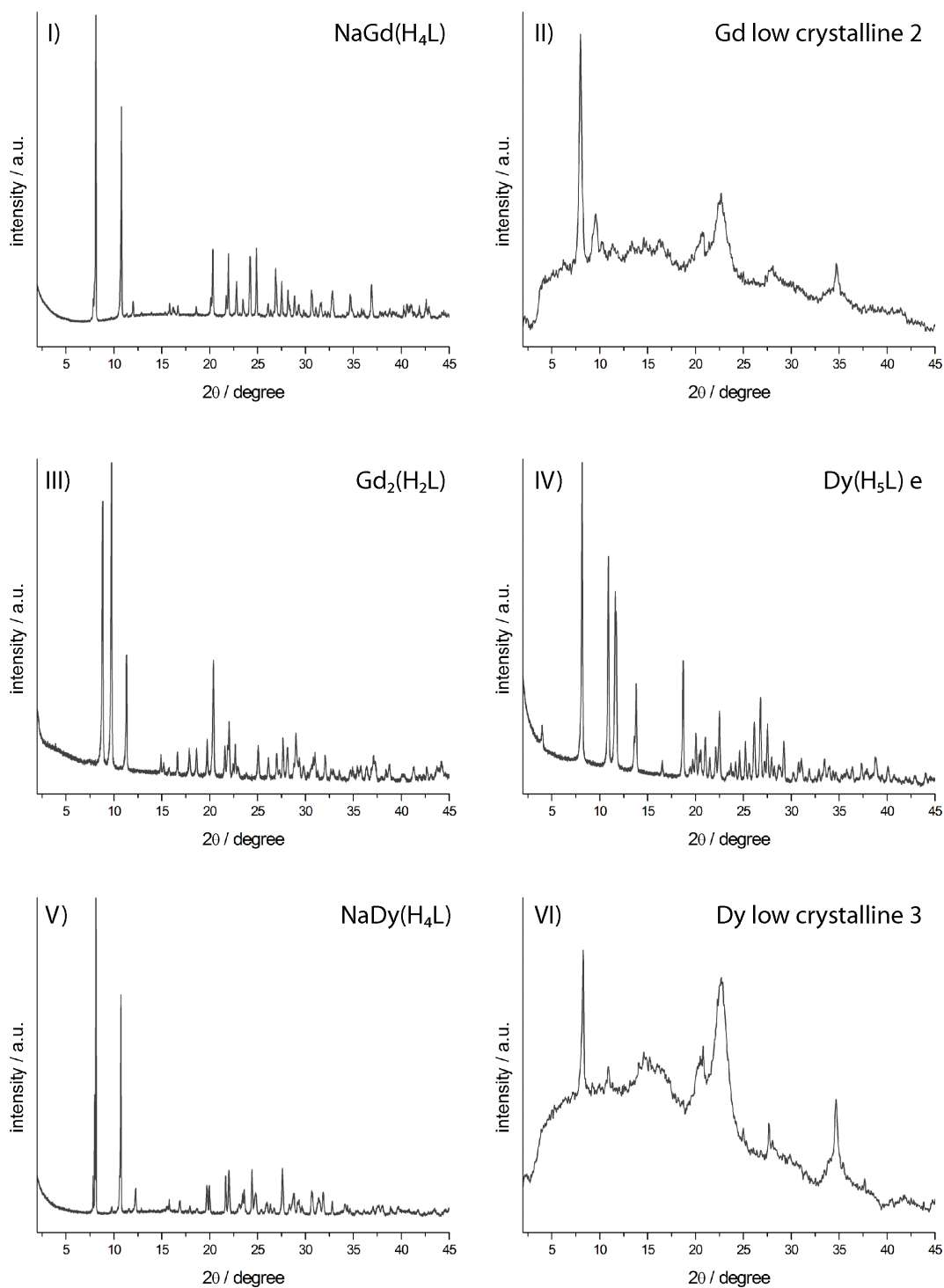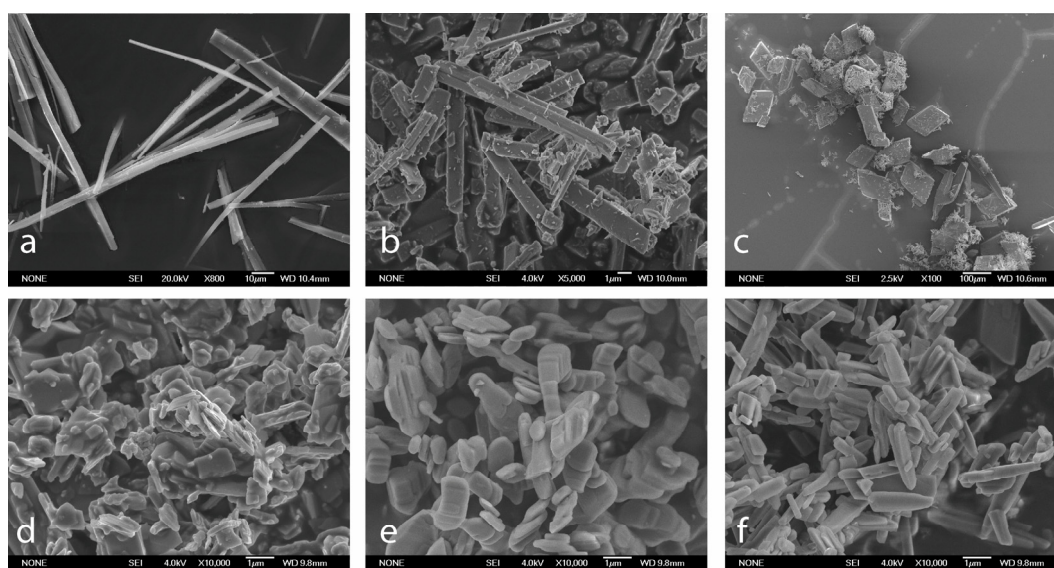
Figure 8.1.1-3: I) XRD pattern of **NaGd(H₄L)**; II) XRD pattern of **Gd-low crystalline 2**; III) XRD pattern of **Gd₂(H₂L)**; IV) XRD pattern of **Dy(H₅L) e**; V) XRD pattern of **NaDy(H₄L)**; VI) XRD pattern of **Dy-low crystalline 3**.
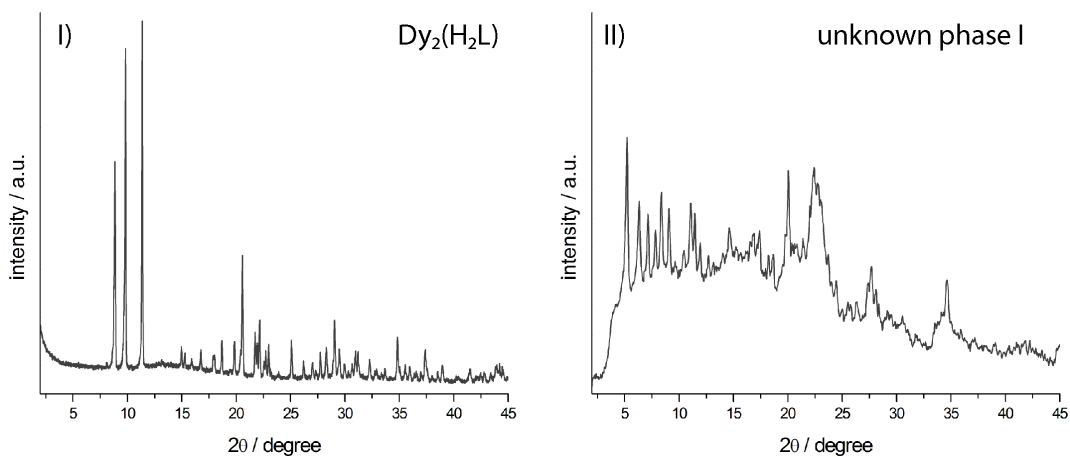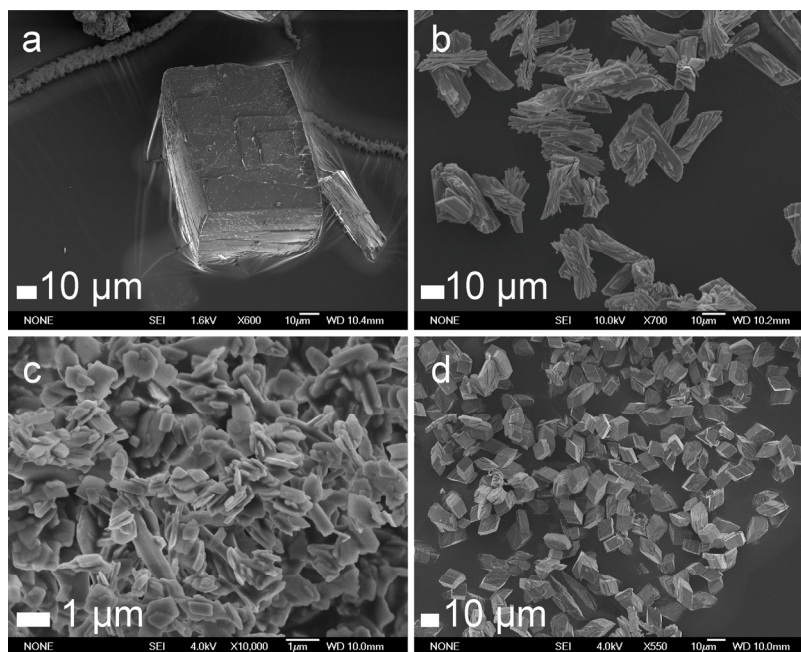
Figure 8.1.1-4: I) XRD pattern of **Dy$_2$(H$_2$L)**; II) XRD pattern of unknown phase 1.

8.1.2 Selected Scanning Electron Micrographs of the New Phases

Figure 8.1.2-1: SEM micrographs of compounds crystallized at a batch composition of Ln^{3+}: H$_8$L = 1:1 a) **La(H$_5$L) a** ; b) **La(H$_5$L) c**; c) **Nd(H$_5$L) b**; d) **Nd(H$_5$L) d**; e) **Gd(H$_5$L) d**; f) **Dy(H$_5$L) e**.

Figure 8.1.2-2: SEM micrographs of compounds with structure type II a) **La$_2$(H$_2$L)**; b) **Nd$_2$(H$_2$L)**; c) **Gd$_2$(H$_2$L)**; d) **Dy$_2$(H$_2$L)**.

8.1.3 Additional Raman Spectra
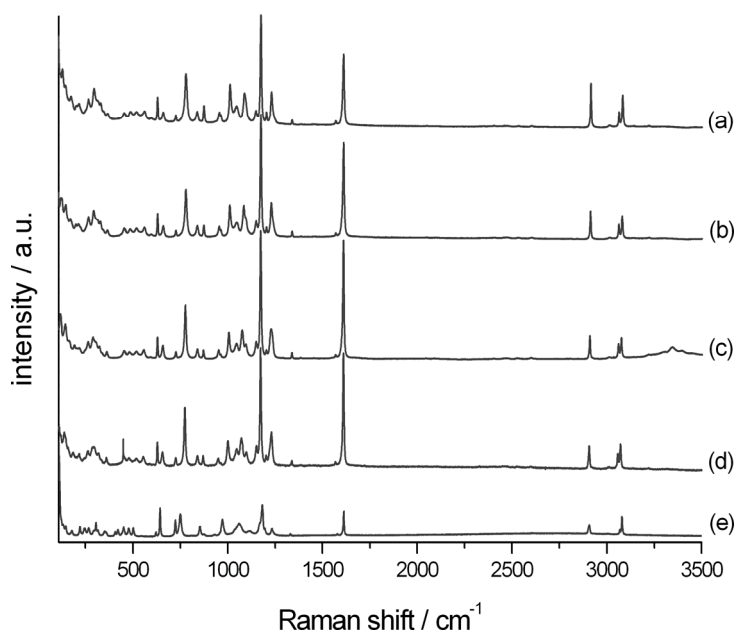
Figure 8.1.3-1: Raman spectra of **Dy$_2$(H$_2$L)** (a), **Gd$_2$(H$_2$L)** (b), **Nd$_2$(H$_2$L)** (c), **La$_2$(H$_2$L)** (d) und **H$_8$L** (e).
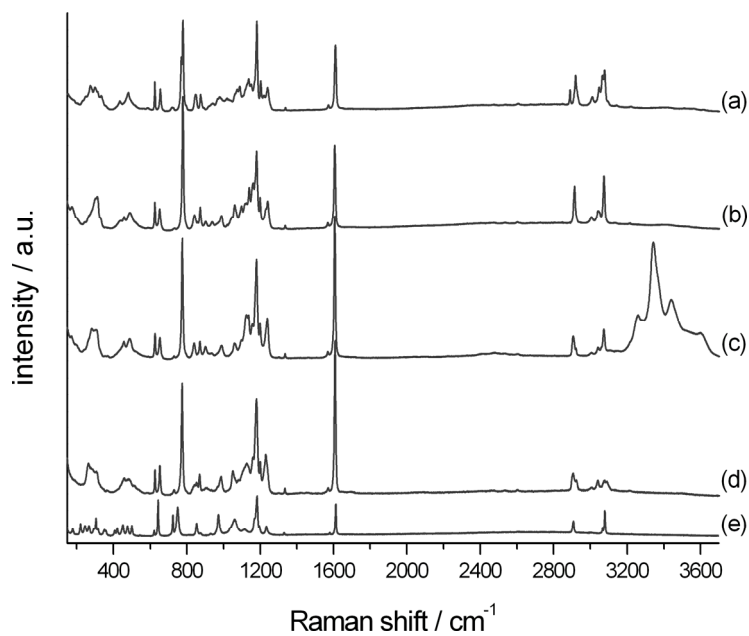
Figure 8.1.3-2: Raman spectra of **NaDy(H$_4$L)** (a), **NaGd(H$_4$L)** (b), **NaNd(H$_4$L)** (c), **NaLa(H$_4$L)** (d) und **H$_8$L** (e).

8.1.4 Thermogravimetric Analysis and Differential Scanning Calorimetry Measurements of the New Compounds
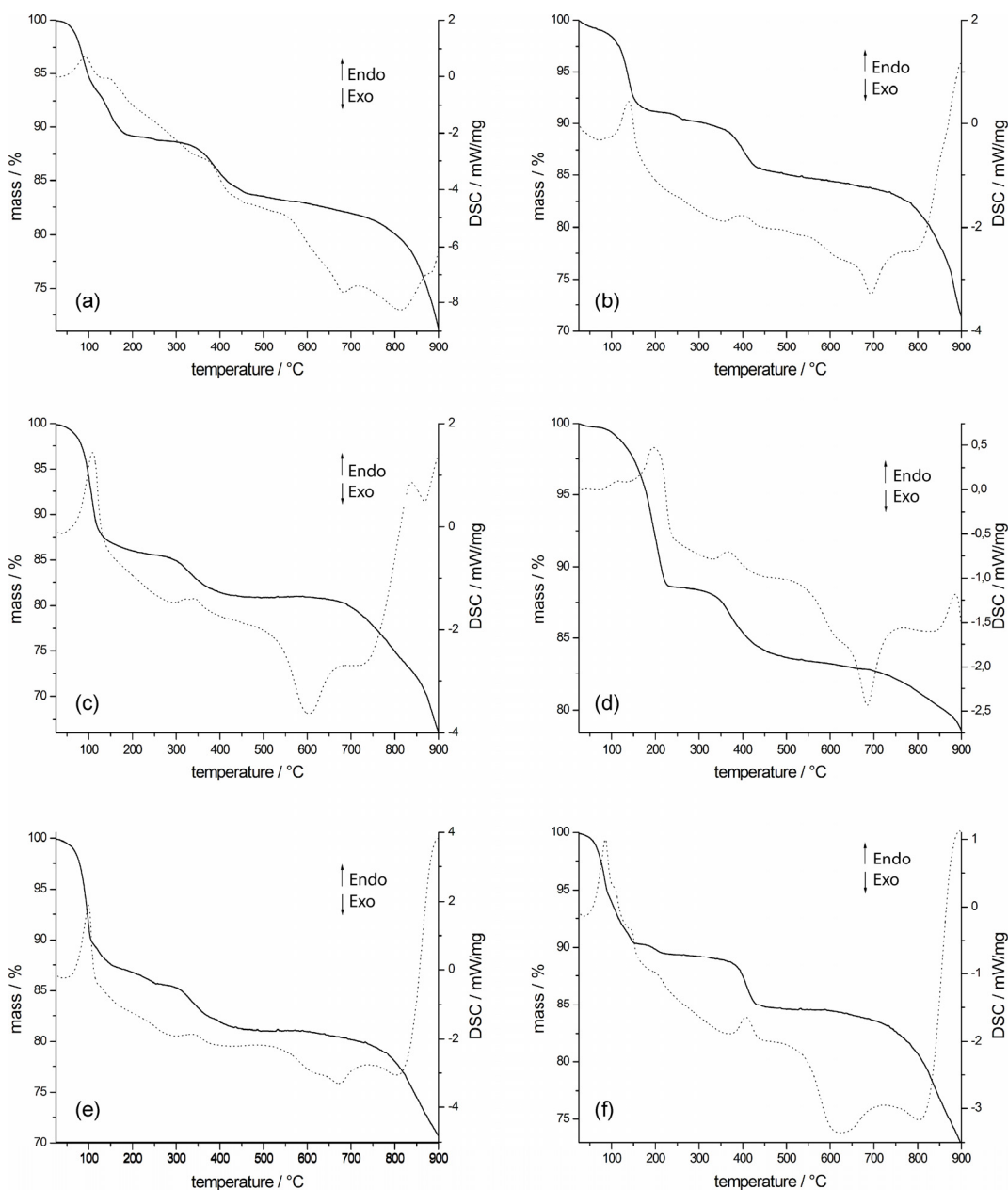
Figure 8.1.4-1: TGA and DSC of **La(H$_5$L) a** (a), **La(H$_5$L) c** (b), **Nd(H$_5$L) d** (c), **Nd(H$_5$L) b** (d), **Gd(H$_5$L) d** (e) und **Dy(H$_5$L) e** (f).

Compounds with structure type I: Thermogravimetric analysis shows three prominent steps of weight loss that all five compounds have in common: Step 1 proceeds between 60°C and 180°C. It is endothermal, and varies between 9 and

14%. In the case of **La(H₅L)** a (11%) and Nd(H₅L) b (12%) these values fit well to the loss of the four water molecules of the crystal structure. Between 300 and 450 degrees, step 2 indicates a second endothermal phase transformation. At 600 °C, oxidation and combustion of the carbon framework occurs in the strongly exothermal step III.

Compounds with structure type II: Thermogravimetric analysis shows for all four compounds a total weight loss of 20 %. The first weight loss of 16-18 % proceeds in two endothermic steps in the range from 60 to 150 °C and 150 to 250 °C, and correspond to the loss of the eight water molecules.
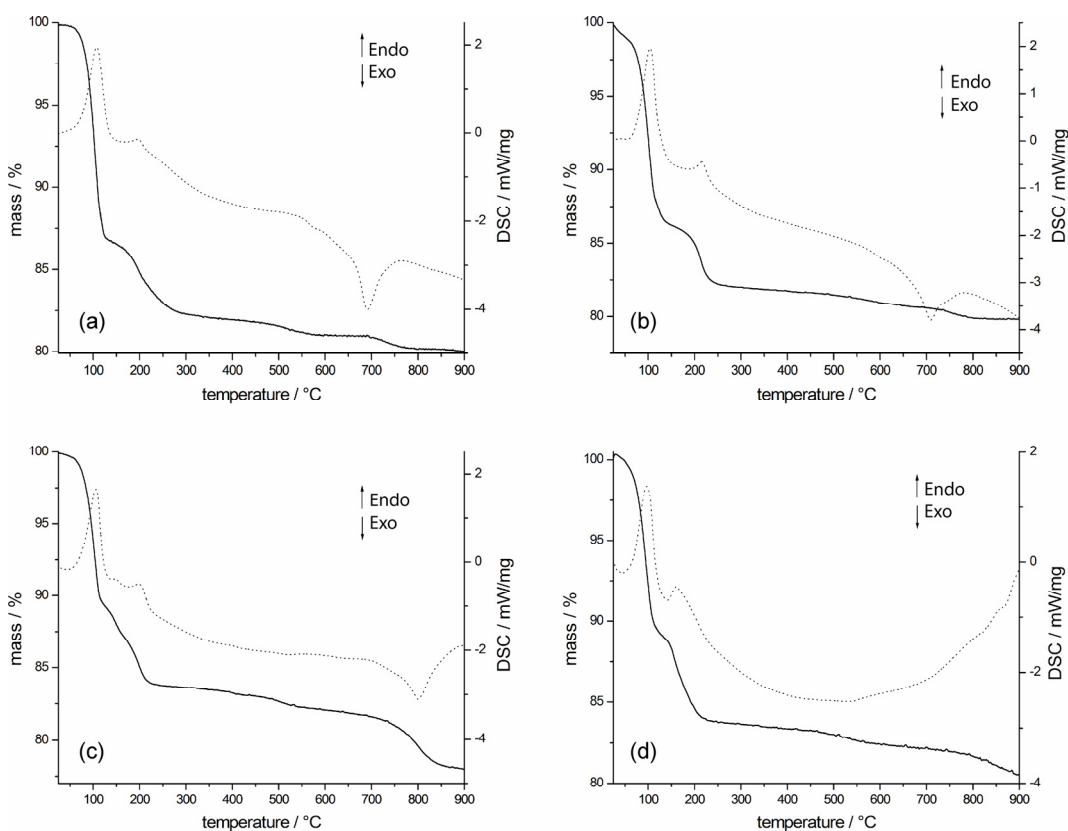
Figure 8.1.4-2: Thermogravimetric analysis and DSC of **La₂(H₂L)** (a), **Nd₂(H₂L)** (b), **Gd₂(H₂L)** (c) and **Dy₂(H₂L)** (d).

Compounds with structure type III: Thermogravimetric analysis shows three steps of weight loss for **NaLa(H$_4$L)**, **NaNd(H$_4$L)**, **NaGd(H$_4$L)** and **NaDy(H$_4$L)**. Step 1 with a weight loss of 11 % corresponds to the loss of the four water molecules per asymmetric unit. Remarkably the temperature necessary for the water removal increases from La^{3+} (60 °C − 160 °C) to Dy^{3+} (110 °C − 210 °C). Similar to phases with structure type I an endothermal phase transformation takes place between 300°C and 450 °C (step 2). Between 500 and 600°C oxidation and combustion of the carbon framework occurs in a strongly exothermal step 3.
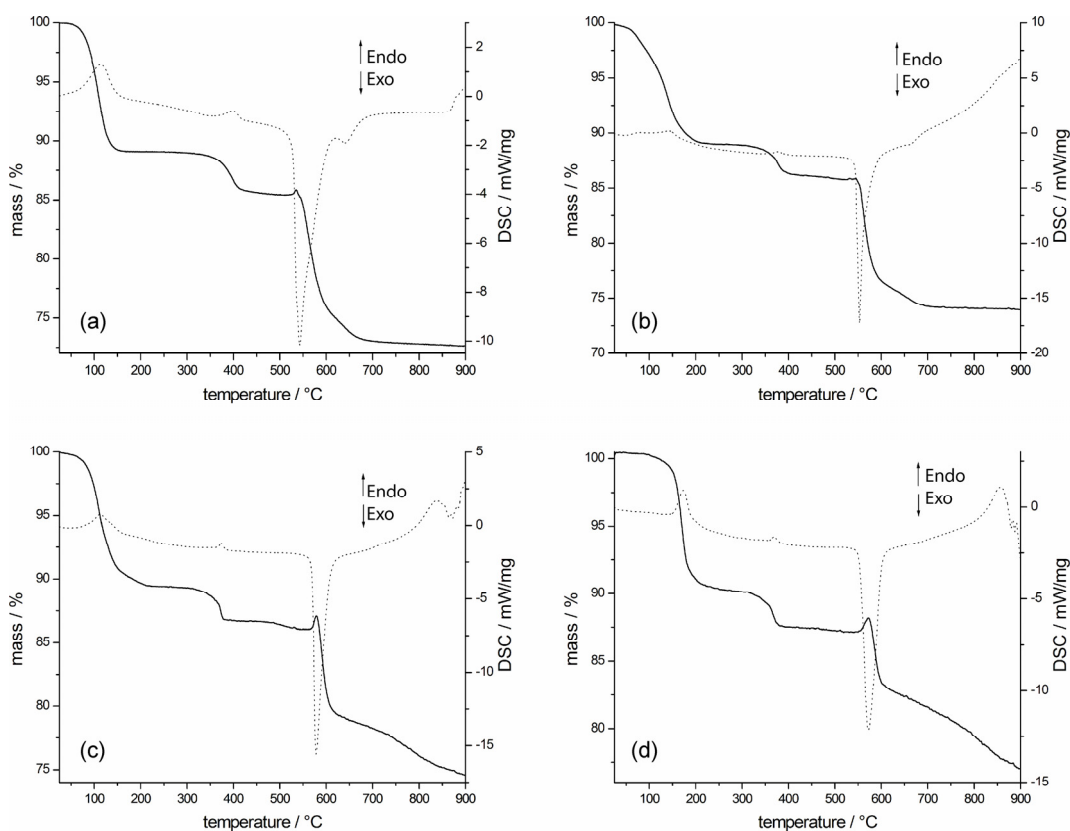
Figure 8.1.4-3: Thermogravimetric analysis and DSC of **NaLa(H$_4$L)** (a), **NaNd(H$_4$L)** (b), **NaGd(H$_4$L)** (c) and **NaDy(H$_4$L)** (d).

8.1.5 Additional Crystallographic Information

Table 8.1.5 - 1: Crystallographic details of the structure solutions of **Nd(H$_5$L) a**, **La(H$_5$L) b**, **La$_2$(H$_2$L)** and **NaLa(H$_4$L)**:

parameter	La(H$_5$L) b	Nd(H$_5$L) a	La$_2$(H$_2$L)	NaLa(H$_4$L)
empirical formula	C$_8$H$_{19}$LaO$_{16}$P$_4$	C$_8$H$_{19}$NdO$_{16}$P$_4$	C$_8$H$_{24}$La$_2$O$_{20}$P$_4$	C$_8$H$_{18}$LaNaO$_{16}$P$_4$
fw [gmol^{-1}]	634.03	639.36	841.97	656.01
cryst size [mm^3]	0.07x0.03x0.03	0.04x0.01x0.01	0.05x 0.06x 0.12	0.04x0.04x0.04
cryst syst	triclinic	triclinic	triclinic	monoclinic
space group	P-1	P-1	P-1	P2$_1$/n
a [Å]	5.49830(10)	5.67270(20)	6.2659(2)	8975
b [Å]	12.5695(3)	12.19310(40)	9.8383(2)	21691
c [Å]	14.6540(3)	14.47360(50)	10.4758(2)	10186
α [°]	106.223(2)	73.0258(19)	99.7269(15)	90
β [°]	100.6700(10)	85.4674(21)	103.6343(14)	105.56
γ [°]	99.5930(10)	76.7428(20)	107.8791(14)	90
V [10^6Å^3]	929.67(3)	931.900(56)	576.59(3)	1910.2
Z	2	2	1	4
ρ [gcm-3]	2.265	2.268	2.425	2.267
μ [mm-1]	2.724	3.21	4.023	2.675
abs. correct.	-	-	-	-
F(000)	624	624	406	1272
2θ range [°]	3.1 - 27.5	3.1, 27.5	3.4 - 27.5	3.134, 27.485
range in hkl	-7 ≤ h ≤7, -16 ≤ k ≤ 16, -19 ≤ l ≤ 19	-7 ≤ h ≤ 7, -15 ≤ k ≤ 15, -18 ≤ l ≤ 18	-8 ≤ h ≤ 8, -12 ≤ k ≤ 12, -13 ≤ l ≤ 13	-11 ≤ h ≤ 11, -28 ≤ k ≤ 27, -13 ≤ l ≤ 13
total data collected	14772	22191	12625	24954
unique/obs data [l>2σ(l)]	4263 / 3809	4256 / 3668	2638 / 2570	4370 / 3877
R(int)	0.0270	0.0306	0.018	0.0173
R1, wR2 [l>2σ(l)]	0.0239, 0.0504	0.0278, 0.0519	0.0139, 0.0334	0.0202, 0.0440
R1, wR2 [all data]	0.0301, 0.0526	0.0378, 0.0545	0.0145, 0.0337	0.0260, 0.0463
GOF	1.077	1.075	1.089	1.080
no. of parameters	336	327	191	340
Δemin/Δemax [eÅ-3]	0.785, -0.593	-0.98, 1.09	-0.45, 1.07	-0.699, 0.098

Selected bond distances in $Nd[(PO_3H)_2CH\text{-}C_6H_4\text{-}CH(PO_3H)(PO_3H_2)]\cdot 4H_2O$, $Nd(H_5L)$ a:

Table 8.1.5 - 2: P-O bonding distances in $Nd(H_5L)$ a:

P–O	Bond length [Å]	fragment
P1–O2	1.499(2)	P-O
P1–O3	1.510(2)	P-O
P1–O1	1.577(3)	P-OH
P2–O4	1.486(2)	P-O
P2–O6	1.533(2)	P-OH
P2–O5	1.559(2)	P-OH
P3–O9	1.494(2)	P-O
P3–O8	1.517(2)	P-O
P3–O7	1.575(3)	P-OH
P4–O11	1.492(2)	P-O
P4–O10	1.511(2)	P-O
P4–O12	1.579(2)	P-OH

Table 8.1.5 - 3: Nd-O distances in $Nd(H_5L)$ a

Nd–O	Bond length [Å]	ligand
Nd1–O2	2.372(2)	PO_3
Nd1–O3	2.464(2)	$PO_3\text{-}C\text{-}PO_3$
Nd1–O4	2.412(2)	$PO_3\text{-}C\text{-}PO_3$
Nd1–O9	2.407(2)	$PO_3\text{-}C\text{-}PO_3$
Nd1–O10	2.410(2)	$PO_3\text{-}C\text{-}PO_3$
Nd1–O11	2.395(2)	PO_3
Nd1–O13	2.640(3)	H_2O
Nd1–O14	2.567(4)	H_2O

Table 8.1.5 - 4: Hydrogen bonds in Nd(H_5L) a:

d(D–H···A) [Å]	d(D–H) [Å]	d(H···A) [Å]	d(D···A) [Å]	angle [°]	type
O1–H1···O15	0.69(4)	1.97(4)	2.657(4)	175(5)	interlayer I
O5–H5···O13	1.07(6)	1.55(6)	2.604(3)	168(5)	intralayer
O6 –H6···O8	0.92(6)	1.54(6)	2.449(3)	176(5)	interlayer II
O7– H7···O16	0.36(8)	2.23(7)	2.578(5)	164(15)	interlayer II
O12–H12···O10	0.73(4)	2.21(4)	2.842(4)	146(4)	interlayer I
O12–H12···O14	0.73(4)	2.39(4)	2.972(5)	138(4)	interlayer I
O13–H13A···O4	0.79(4)	2.46(4)	2.751(4)	103(3)	intralayer
O13–H13B···O8	0.75(4)	1.90(4)	2.630(4)	164(4)	intralayer
O14–H*···O14			2.965(2)		interlayer I
O14–H*···O15			2.909(2)		interlayer I
O15–H15A···O1	0.48(5)	2.57(5)	2.915(4)	133(8)	interlayer I
O15–H*···O3			2.793(4)		interlayer I
O16–H16A···O7	0.87(3)	2.39(3)	2.838(5)	113(3)	interlayer II
O16–H*···O6			2.87(20)		interlayer II

Intralayer bonds are situated in one layer. Interlayer bonds I join two layers face to face with a interlayer distance of 5.73 Å. Interlayer bonds II connect the layer pairs with an interlayer distance of 8.15 Å. (Hydrogen bonds marked with *were not calculated with SHELXL due to a missing hydrogen atom. They were added based on bond distances measured in diamond.)

Selected bond distances in La[(PO$_3$H)$_2$CH-C$_6$H$_4$-CH(PO$_3$H)(PO$_3$H$_2$)]·4H$_2$O, **La(H$_5$L) b**:

Table 8.1.5 - 5: P-O bond distances in **La(H$_5$L) b**

P–O	bond length [Å]	fragment
P1–O1	1.507(2)	P-O
P1–O2	1.5235(19)	P-O-H$^{\text{half occupied}}$
P1–O3	1.560(2)	P-O-H
P2–O6	1.5016(19)	P-O
P2–O5	1.5125(19)	P-O
P2–O4	1.572(2)	P-O-H
P3–O8	1.492(2)	P-O
P3–O7	1.509(2)	P-O
P3–O9	1.575(2)	P-O-H
P4–O10	1.501(2)	P-O
P4–O12	1.518(2)	P-O-H$^{\text{half occupied}}$
P4–O11	1.562(2)	P-O-H

Table 8.1.5 - 6: La-O distances in **La(H$_5$L) b**

La–O	bond length [Å]	ligand
La1–O6	2.4165(18)	PO$_3$
La1–O7	2.4502(19)	PO$_3$-C-PO$_3$
La1–O8	2.454(2)	PO$_3$
La1–O5	2.5024(18)	PO$_3$-C-PO$_3$
La1–O10	2.5103(19)	PO$_3$-C-PO$_3$
La1–O1	2.5237(19)	PO$_3$-C-PO$_3$
La1–O14	2.647(2)	H$_2$O
La1–O13	2.661(3)	H$_2$O

Table 8.1.5 - 7: hydrogen bonds in **La(H$_5$L) b**

d(D–H···A) [Å]	d(D–H) [Å]	d(H···A) [Å]	d(D···A) [Å]	angle [°]	type
O2–H2···O2	1.2084(19)	1.2084(19)	2.417(4)	180.000(2)	interlayer II
O3–H3···O16	0.79(4)	1.79(4)	2.577(3)	179(4)	interlayer II
O4–H4···O15	0.75(3)	1.88(3)	2.618(3)	170(4)	interlayer I
O9–H9···O7	0.819(5)	2.07(3)	2.837(3)	156(6)	interlayer I
O9–H9···O13	0.819(5)	2.36(6)	2.872(4)	121(5)	interlayer I
O11–H11···O14	0.86(4)	1.84(4)	2.699(3)	174(4)	intralayer
O12–H12···O12	1.2119(19)	1.2119(19)	2.424(4)	180.0(1)	interlayer II
O13–H13A···O9	0.63(6)	2.53(7)	3.009(4)	135(7)	Interlayer I
O13–H13B···O9	0.79(9)	2.25(8)	2.872(4)	136(8)	interlayer I
O14–H14A···O2	0.80(4)	2.06(4)	2.781(3)	149(4)	interlayer II
O14–H14B···O1	0.85(5)	1.95(5)	2.808(3)	178(4)	intralayer
O15–H15A···O4	0.79(5)	2.31(5)	2.998(3)	146(4)	interlayer I
O15–H15B···O5	0.76(5)	1.98(5)	2.724(3)	164(5)	interlayer I
O16–H16A···O10	0.72(5)	2.18(5)	2.869(3)	161(5)	interlayer II

Intralayer Bonds are situated in one layer. Interlayer bonds I join two layers face to face with a interlayer distance of 5.91 Å. Interlayer bonds II connect the layer pairs with an interlayer distance of 7.73 Å.

Bond distances in $La_2[(HO_3P)(O_3P)\text{-}CH\text{-}C_6H_4\text{-}CH\text{-}(PO_3)(PO_3H)]\cdot 8H_2O$, **$La_2(H_2L)$**:

Table 8.1.5 - 8: P-O bond distances in $La_2(H_2L)$

P−O	bond length [Å]	fragment
P1−O1	1.5225(14)	P-O
P1−O3	1.5271(14)	P-O
P1−O4	1.5381(13)	P-O
P2−O6	1.5125(14)	P-O
P2−O2	1.5156(15)	P-O
P2−O5	1.5601(14)	P-OH

Table 8.1.5 - 9: La-O distances in **$La_2(H_2L)$**

La−O	bond length [Å]	ligand
La−O4	2.4435(13)	PO_3
La−O1	2.4514(14)	PO_3-C-PO_3
La−O2	2.4709(14)	PO_3-C-PO_3
La−O6	2.4851(14)	PO_3-C-PO_3
La−O7	2.5086(15)	H_2O
La−O3	2.5316(13)	PO_3
La−O8	2.6055(17)	H_2O
La−O4	2.6578(13)	PO_3-C-PO_3

Table 8.1.5 - 10: hydrogen bonds in **$La_2(H_2L)$**

d(D−H···A) [Å]	d(D−H) [Å]	d(H···A) [Å]	d(D···A) [Å]	angle [°]	type
O5 H5 O9	0.820(5)	1.694(8)	2.505(2)	170(3)	interlayer
O9 H91 O6	0.820(5)	2.016(8)	2.827(2)	170(3)	interlayer
O9 H92 O10	0.821(5)	1.921(8)	2.734(3)	170(3)	interlayer
O7 H71 O2	0.821(5)	1.968(6)	2.788(2)	177(3)	intralayer
O7 H72 O5	0.820(5)	2.021(16)	2.773(2)	152(3)	interlayer
O10 H102 O3	0.822(5)	1.895(9)	2.700(2)	166(3)	interlayer
O10 H101 O1	0.822(5)	2.156(8)	2.962(2)	167(2)	interlayer
O8 H81 O10	0.820(5)	2.081(10)	2.882(3)	165(3)	interlayer

Intralayer Bonds are situated in one layer. Interlayer bonds connect two layers.

Bond distances in LaNa[(PO$_3$H)$_2$CH-C$_6$H$_4$-CH(PO$_3$H)$_2$]·4H$_2$O, **NaLa(H$_4$L)**:

Table 8.1.5 - 11: P-O bond distances in **NaLa(H$_4$L)**:

P–O	bond length [Å]	fragment
P1–O2	1.5053(17)	P-O
P1–O3	1.5074(16)	P-O
P1–O1	1.5822(18)	P-OH
P2–O5	1.4967(17)	P-O
P2–O6	1.5075(16)	P-O
P2–O4	1.5916(18)	P-OH
P3–O9	1.4959(17)	P-O
P3–O7	1.5090(16)	P-O
P3–O8	1.5758(19)	P-OH
P4–O12	1.5007(17)	P-O
P4–O11	1.5025(16)	P-O
P4 –O10	1.5938(17)	P-OH

Table 8.1.5 - 12: La-O distances in **NaLa(H$_4$L)**:

La–O	bond length [Å]	ligand
La1–O9	2.4392(16)	PO$_3$-C-PO$_3$
La1–O6	2.4883(16)	PO$_3$-C-PO$_3$
La1–O2	2.4970(16)	PO$_3$-C-PO$_3$
La1–O12	2.5251(16)	PO$_3$-C-PO$_3$
La1–O5	2.5326(16)	PO$_3$-C-PO$_3$
La1–O11	2.5422(15)	PO$_3$-C-PO$_3$
La1–O7	2.5887(16)	PO$_3$-C-PO$_3$
La1–O3	2.5986(16)	PO$_3$-C-PO$_3$

Table 8.1.5 - 13: Na-O distances in **NaLa(H$_4$L)**:

Na–O	bond length [Å]	ligand
Na–O16	2.215(2)	H$_2$O
Na–O11	2.2957(18)	PO$_3$
Na–O5	2.3524(18)	PO$_3$
Na–O13	2.402(2)	H$_2$O
Na–O3	2.5311(19)	PO$_3$
Na–O10	2.665(2)	PO$_3$

8.2 Supporting Information to Chapter 5

8.2.1 Rietveld Refinement of NaLa(H$_4$L)$_{dehyd}$

Table 8.2.1 – 1: Crystallographic data for **NaLa(H$_4$L)$_{dehyd}$**

Data collection		
	Diffractometer	Stoe STADI P
	Radiation	CuKα_1 (1.54059 Å)
	2θ range (°2θ)	6.50 - 67.50
	Step size (°2θ)	0.01
Unit cell		
	Space group	P2$_1$/n
	a (Å)	7.1510(1)
	b (Å)	22.7160(2)
	c (Å)	10.1132(2)
	β (°)	100.7(5)
Rietveld refinement		
	Number of observations	5797
	Number of contributing reflections	602
	Number of geometric restraints	96
	Number of structural parameters	85
	Number of profile parameters	10
	R$_F$	0.055
	R$_{wp}$	0.086
	R$_{exp}$	0.075
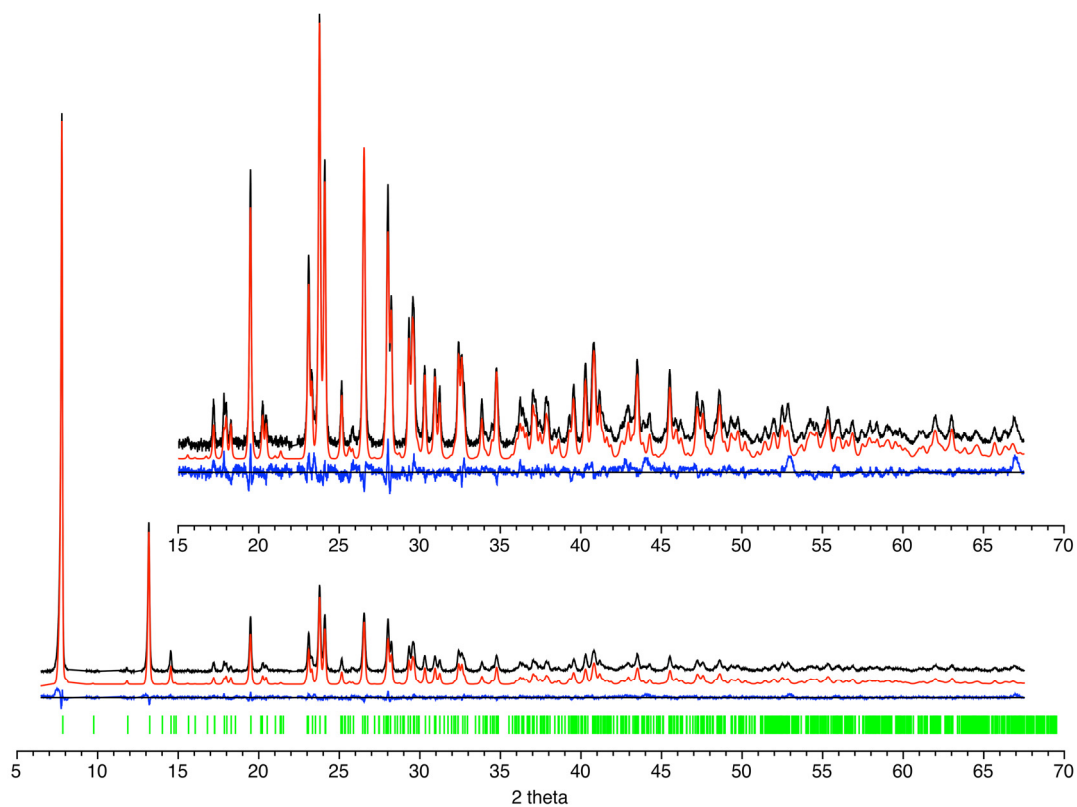
Figure 8.2.1 - 1: Observed (black), calculated (red) and difference (blue) profiles for the Rietveld refinement of **NaLa(H₄L)dehyd**.The higher angle data have been scaled up by a factor of 5 to show more detail. $\lambda = 1.54059$ Å.

8.2.2 Bond Distances in NaLa(H₄L)$_{dehyd}$

Table 8.2.2 - 1: P-O bond distances in **NaLa(H₄L)$_{dehyd}$**.

P–O	bond distance [Å]	bond
P1–O1	1.58(2)	P-OH
P1–O2	1.52(2)	P-O
P1–O3	1.51(2)	P-O
P2–O4	1.57(1)	P-OH
P2–O5	1.51(2)	P-O
P2–O6	1.51(2)	P-O
P3–O7	1.50(2)	P-O
P3–O8	1.59(2)	P-OH
P3–O9	1.51(2)	P-O
P4–O10	1.57(2)	P-OH
P4–O11	1.51(2)	P-O
P4–O12	1.51(2)	P-O

Table 8.2.2 - 2: La-O bond distances in **NaLa(H₄L)$_{dehyd}$**.

La–O	bond distance [Å]
La1–O2	2.58(2)
La1–O3	2.50(2)
La1–O5	2.65(2)
La1–O6	2.47(2)
La1–O7	2.52(2)
La1–O9	2.48(2)
La1–O11	2.56(2)
La1–O12	2.70(2)

Table 8.2.2 - 3: Na-O bond distances in **NaLa(H₄L)$_{dehyd}$**

| Na–O	bond distance [Å]
Na1–O3	2.53(2)
Na1–O5	2.42(2)
Na1–O6	2.73(2)
Na1–O11	2.30(2)
Na1–O12	2.38(2)

8.2.3 Additional Illustrations Comparing NaLa(H₄L) and NaLa(H₄L)$_{dehyd}$
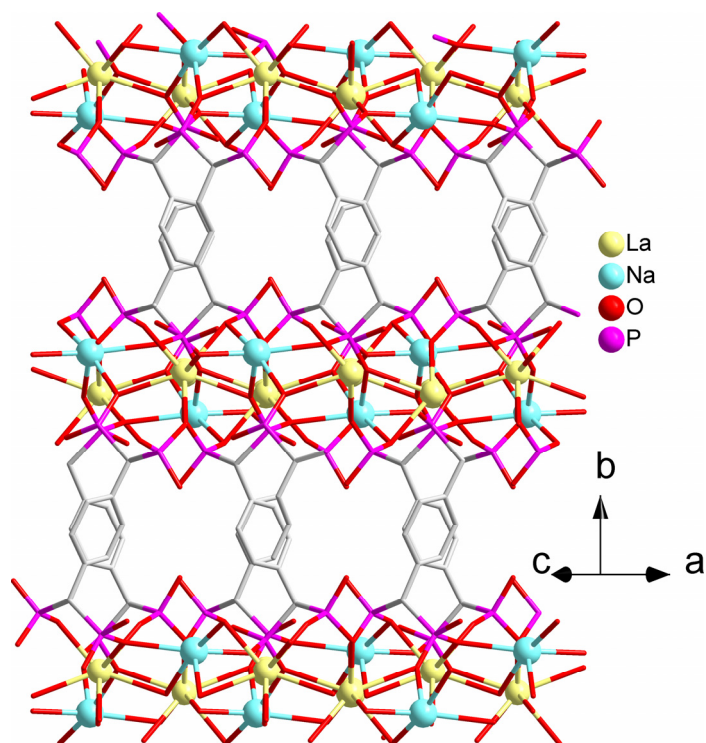
Figure 8.2.3 - 1: Projection along [101] showing the apertures in the channel walls of **NaLaH₄L$_{dehyd}$** that interconnect the contracted main channels.
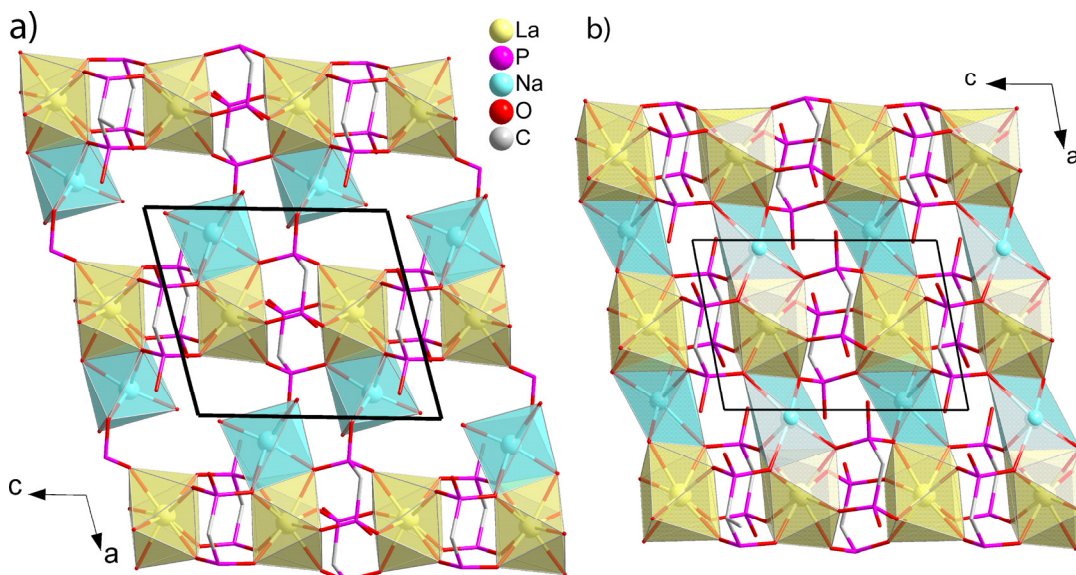

Figure 8.2.3 - 2: Projection along [010] of the structure of a) **NaLa(H₄L)** and b) **NaLa(H₄L)$_{dehyd}$** showing the -La-O-Na-O-La- chain-closing upon dehydration. (Water molecules, benzene groups, and hydrogen atoms are omitted for clarity.)
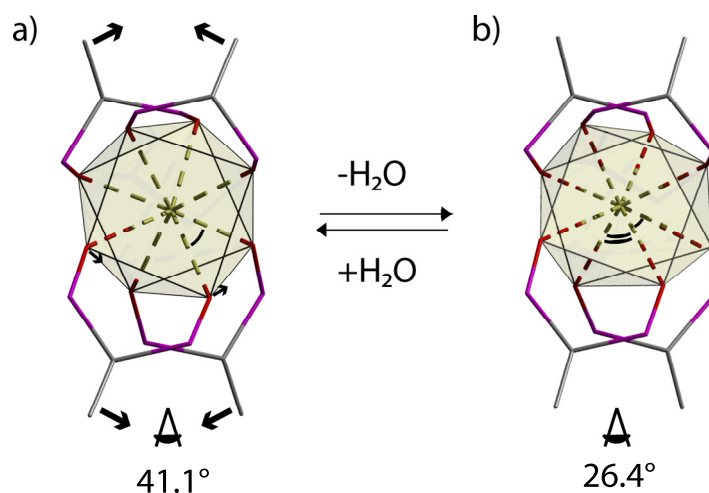
Figure 8.2.3 - 3: The distortion of the coordination geometry of (a) **NaLa(H$_4$L)** during the dehydration to (b) **NaLaH$_4$L$_{dehyd}$** leads to a decreasing of the acute angle of the rhombus shown in Figure 5.1 - 1.

8.2.4 Additional XRD Patterns of NaLa(H$_4$L) Samples after Ion Exchange Experiments.
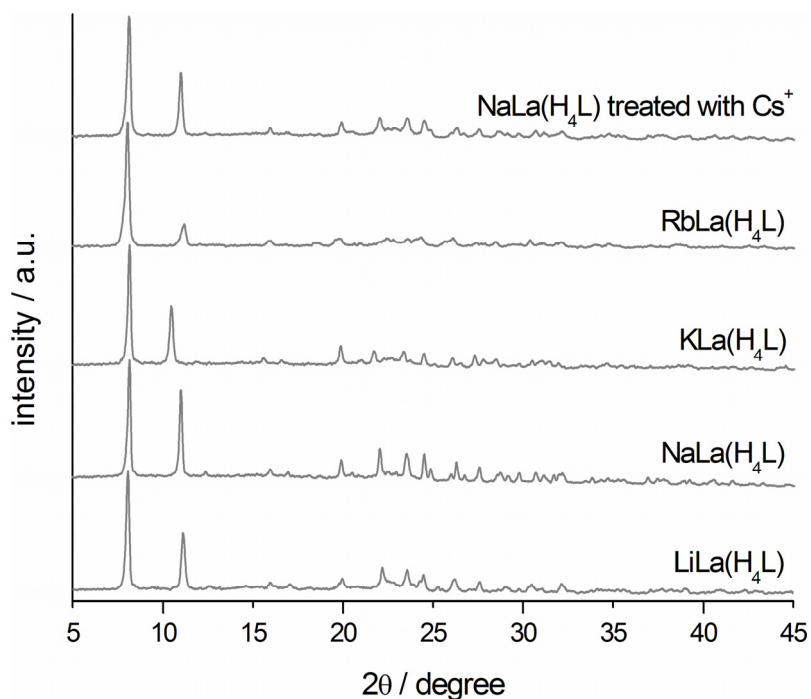
Figure 8.2.4 - 1: XRD patterns of **LiLa(H$_4$L)**, **NaLa(H$_4$L)**, **KLa(H$_4$L)**, **RbLa(H$_4$L)** and **NaLa(H$_4$L)** treated with Cs$^+$.

8.2.5 EDX Analysis of Ion Exchanged Samples

Table 8.2.5 - 1: Chemical Composition of ion exchanged samples as determined by EDX-analysis.

sample	Na[*]/P	M/P	La[*]/P	P
$NaLa(H_4L)$	1,3	-	1,1	4,0
$Na_{(1-x)}Li_xLa(H_4L)$	0,1	-[**]	1,0	4,0
$Na_{(1-x)}K_xLa(H_4L)$	0,1	0,9	1,0	4,0
$Na_{(1-x)}Rb_xLa(H_4L)$	0,2	0,8	0,8	4,0
$Na_{(1-x)}Cs_xLa(H_4L)$	0,9	0,2	1,1	4,0
$Na_{(1-2x)}Mg_xLa(H_4L)$	1,1	0,0	0,9	4,0
$Na_{(1-2x)}Ca_xLa(H_4L)$	1,3	0,3	1,0	4,0
$Na_{(1-2x)}Sr_xLa(H_4L)$	1,4	0,1	0,8	4,0
$Na_{(1-2x)}Ba_xLa(H_4L)$	1,0	0,2	1,0	4,0
$Na_{(1-2x)}Ni_xLa(H_4L)$	1,5	0,0	0,9	4,0
$Na_{(1-2x)}Cu_xLa(H_4L)$	0,9	0,2	0,9	4,0
$Na_{(1-2x)}Mn_xLa(H_4L)$	1,2	0,1	1,0	4,0

* Values for sodium and lanthanum are not exact, due to an overlap of the respective bands. Usually sodium is overweight. In the case of the alkali ions, exact values were determined with ICP-OES analysis. ** Lithium cannot be detected in EDX spectroscopy.

8.2.6 Thermogravimetric Analysis (TGA) and Differential Scanning Calorimetry (DSC) Measurements of the Alkaline Exchanged Samples of NaLa(H$_4$L)
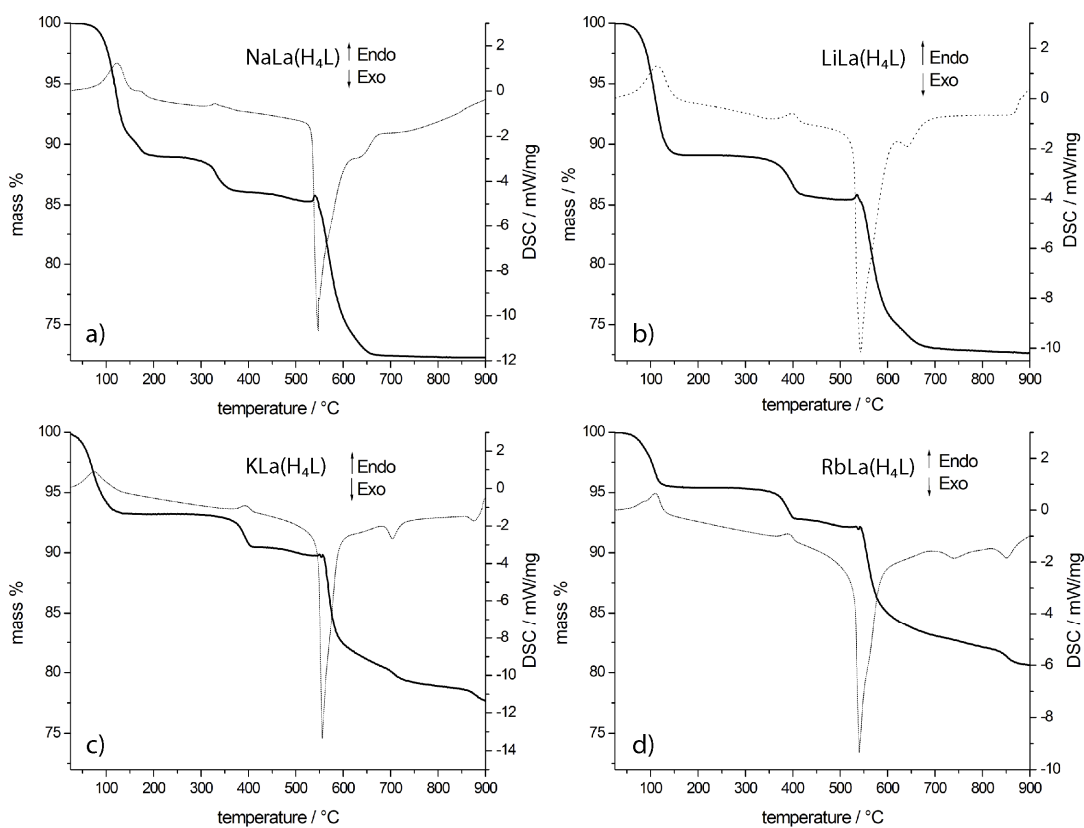
Figure 8.2.6 - 1: Thermogravimetric Analysis and Differential Scanning Calorimetry diagrams of a) **LiLa(H$_4$L)**, b) **NaLa(H$_4$L)**, c) **KLa(H$_4$L)** and d) **RbLa(H$_4$L)**.

8.3 Supporting Information to Chapter 6

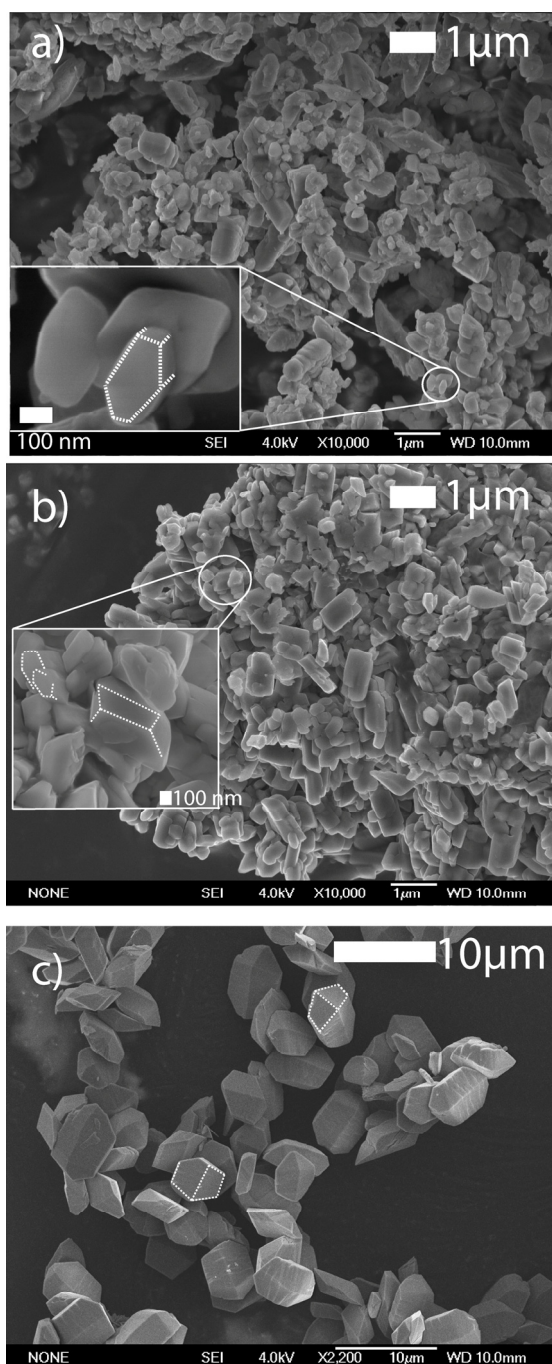### 8.3.1 Additional Scanning Electron Microscopy Images

Figure 8.3.1 - 1: SEM micrographs of a) **KLa(H$_4$L)**, b) **NH$_4$La(H$_4$L)** and c) **RbLa(H$_4$L)**.

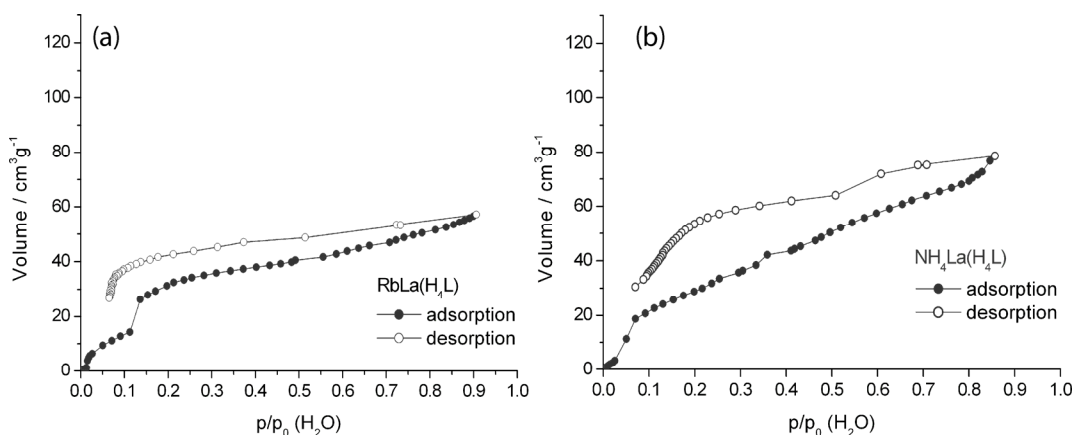### 8.3.2 Additional Water Sorption Isotherms

Figure 8.3.2 ‑ 1: Water sorption isotherms of a) **RbLa(H$_4$L)** and b) **(NH$_4$)La(H$_4$L)**.

8.3.3 Additional Thermogravimetric Analyses and Differential Scanning Calorimetry Measurements

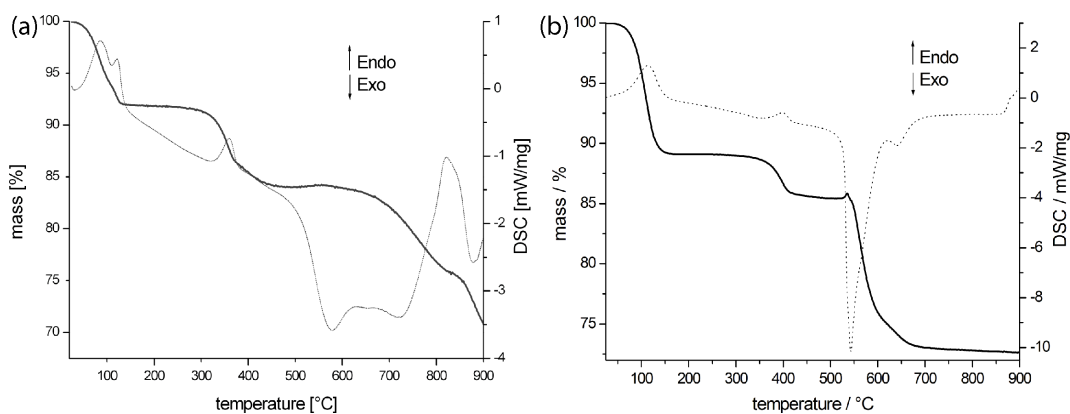**Figure 8.3.3 ‑ 1**: Thermogravimetric Analysis and Differantial Calorimetry Measurement of a) **(NH$_4$)La(H$_4$L)** and b) **NaLa(H$_4$L).** In **NH$_4$La(H$_4$L)** water removal occurs in two energetically distinct endothermic steps.

9 Curriculum Vitae

PERSÖNLICHE INFORMATIONEN:

Name:	Monika Plabst
Geburtsdatum:	28.08.1978
Geburtsort:	München
Nationalität:	deutsch
Familienstand:	ledig

UNIVERSITÄRER UND SCHULISCHER WERDEGANG:

seit 07/2005:	Promotion im Arbeitskreis von Herrn Prof. Thomas Bein (Physikalische Chemie) an der Ludwig-Maximilians-Universität München
	Arbeitsgebiet: *Hochdurchsatzmethoden in der Hydrothermalsynthese von Zeolithen und metallorganischen Gerüstverbindungen(MOFs)*
	Weitere Tätigkeiten: Betreuung von Forschungspraktika und einer Diplomarbeit, Leitung von Seminaren und Kurspraktika, Betreuung von Hochdurchsatzanlagen und Röntgengeräten.
	Koordinatorin im Projekt „Funktionale Asymmetrische Netzwerke" (LMU excellent) von 10/2007- 01/2009: Begleitung der Anschaffung und der Inbetriebnahme von zwei Forschungsgeräten, wissenschaftliche Betreuung eines Teilprojekts (covalent organic frameworks COFs), Budgetverwaltung, Berichterstattung.
11/2004 - 04/2005:	Wissenschaftliche Mitarbeiterin in der Gruppe von Herrn Dr. Pau Ballester (Supramolekulare Chemie) am Instituto Catalan de Investigacion Quimica (ICIQ), Tarragona, Spanien
	Arbeitsgebiet: *Ruthenium-Oligoporphyrine und ihr Komplexbildungs-verhalten mit DABCO*
10/2001 - 06/2004:	Studium der Chemie an der Ludwig – Maximilians - Universität München: Diplom: sehr gut (1.2)
	Diplomarbeit in der Gruppe von Herrn Prof. Thomas Bein (Physikalische Chemie) an der LMU München unter der Leitung von Herrn Dr. Norbert Stock
	Thema: *Ammoniumbisphosphonate – Synthese, Hochdurchsatz-screening und strukturelle Trends*
09/2000 - 08/2001:	Studium der Chemie an der Universität von Barcelona (UB), Spanien
10/1998 - 08/2000:	Studium der Chemie an der Technischen Universität Carola Willhelmina zu Braunschweig. Vordiplom: sehr gut (1.5)
09/1997 - 06/1998:	Aupair Aufenthalt in Mulhouse, Frankreich
06/1997:	Abitur am Theresiengymnasium, München

NEBENTÄTIGKEITEN UND AUSLANDSPRAKTIKA:

10/2006 - 03/2008:   Freie Mitarbeit bei der Firma Nanoscape im Bereich Analytik

02/2002 - 06/2002:   HiWi-Stelle im Arbeitskreis von Herrn Prof. Klaus Meerholz (Physikalische Chemie) an der Ludwig-Maximilians-Universität München

    Arbeitsgebiet: *Organic Light Emitting Diodes (OLEDs)*

02/2001 - 07/2001:   Praktikum im Rahmen des Erasmusprogramms an der Universität von Barcelona in der Gruppe von Herrn Dr. Guillermo Muller unter der Leitung von Herrn Dr. Daniel Sainz. (Organometallchemie)

    Thema: *Study and Characterization of Phosphapalladacycles and its Application in the Heck-Reaction*

09/2000 - 12/2000:   Praktikum im Rahmen des Erasmusprogramms an der Universität von Barcelona in der Gruppe von Herrn Dr. Miguel Pericas unter der Leitung von Herrn Dr. Albert Moyano. (Asymmetrische Katalyse)

    Thema: *Synthesis of (4r)-N-Crotonyl-4-ferrocenyl-1,3-oxazolidinone and Study of ist Diels-Alder Reaction with Cyclopentadiene*

BESONDERE KENNTNISSE:

Sprachen: Deutsch: Muttersprache; Englisch und Spanisch: fließend in Wort und Schrift; Französisch: gut; Katalanisch: Grundkenntnisse

EDV: MS Office, Adobe CS, POV-Ray, Endnote, Scifinder, Origin, Diamond, WinGX, WinXPOW, DIFFRAC

Methoden: Hochdurchsatzmethoden; Röntgenbeugung an Pulvern und Einkristallen; NMR, IR, Raman- und Fluoreszenzspektroskopie; Rasterelektronenmikroskopie und EDX; Aufdampfanlage, TGA/DSC; Sorption; ICP-OES, GC-MS und HPLC; Schlenk Technik, Glove Box, Flow Box. Spincoating und Dektak Profilometrie

WEITERES:

seit 2006:   Aktives Mitglied im Jungchemikerforum München; Mitorganisation des Alpenforums 2007 und 2008; 2. Sprecherin im Jahr 2008.

10/2006:   Teilnahme am Wochenkurs Projektmanagement unter der Leitung von Herrn Dr. Lucas von Hippel, Allessa Chemie

09/1999:   Initiierung des Erasmusvertrags zwischen der Universidad de Barcelona und der TU Braunschweig

Hobbys: Bergsteigen, Skifahren, Reisen, Kino, Kochen mit Freunden und Literatur

München, den 14.10.2009

Monika Plabst

10 PUBLIKATIONEN:

M. Plabst, T. Bein
*"1,4 Phenylenebis(methylidyne)tetrakis(phosphonic acid) –A New Building Block in
Metal Organic Framework Synthesis "*
Inorganic Chemistry, 48 (2009) 4331.

M. Plabst, N. Stock, T. Bein
*"Hydrogen-bonded Networks of Ammoniumbisphosphonates - Synthesis, High-Throughput
Screening and Structural Trends"*
Crystal Growth & Design, 9 (2009) 5049–5060.

M. Plabst, L. B. McCusker, T. Bein
*„Exceptional Ion-Exchange Selectivity in a Flexible Open Framework Lanthanum(III)
tetrakisphosphonate"*
Journal of the American Chemical Society, 131 (2009) 18112–18118.

M. Plabst, Ralf Koehn, T. Bein
*„The Influence of the Guest Ion on the Synthesis and Sorption Properties of an Open
Framework Lanthanide Tetrakisphosphonate"*
CrystEngComm, (2010) DOI: 10.1039/b917338m

PRÄSENTATIONEN:

10. Frühjahrssymposium des JungChemikerForum, 2008, Rostock
Poster: *"1,4 Phenylenebis(methylidyne)tetrakis(phosphonic acid) –A New Building Block in
Metal Organic Framework Synthesis"*
<u>M. Plabst</u>, T. Bein

abc technologies 2008, Basel, Schweiz
Poster: *"High-Throughput Methods in Hydrothermal Synthesis of Metal Organic Frameworks
and Zeolites"*
<u>M. Plabst</u>, T. Bein

Informationstag und Diskussionsveranstaltung Potentiale der Hochdurchsatzforschung in der
Materialtechnologie, 2007, DECHEMA, Frankfurt am Main.
Kurzvortrag: *„High-Throughput Methods in the Bein Group"*
<u>M.Plabst</u>, T.Bein

CeNS Winterschool 2007, Maunterndorf, Austria
Poster: *"High-Throughput Methods in Hydrothermal Synthesis"*
<u>M. Plabst</u>, <u>H. v. Heyden</u>, T. Bein